

学位論文

Hadron Injection in the Early Universe  
and Big Bang Nucleosynthesis

宇宙初期におけるハドロン放出と元素合成

平成11年12月博士(理学)申請

東京大学大学院理学系研究科  
物理学専攻

那 和 篤

①

Ph.D THESIS

**Hadron Injection in the Early Universe and  
Big Bang Nucleosynthesis**

Kazunori Kohri

*Dissertation submitted to  
Department of Physics, School of Science, The University of Tokyo  
December, 1999*

# Contents

<b>1 Introduction</b>	<b>1</b>
1.1 Overview	1
1.2 Organization of this thesis	3
<b>2 Standard Big Bang Nucleosynthesis</b>	<b>4</b>
2.1 Review of Observation	4
2.2 Review of theory in SBBN	6
2.2.1 Thermal history	6
2.2.2 Nuclear Statistical Equilibrium	7
2.2.3 Neutron to proton ratio	10
2.2.4 Freeze-out of $n/p$	11
2.2.5 Production of light elements	12
2.3 Monte Carlo simulation	16
2.4 Statistical Analysis and Results	21
<b>3 Late-time entropy production with Hadron injection and Big Bang Nucleosynthesis</b>	<b>24</b>
3.1 Late-time entropy production : overview	24
3.2 Formulation of Neutrino Thermalization	26
3.2.1 Reheating Temperature	26
3.2.2 Basic Equations	27
3.3 Neutrino Thermalization and BBN	30
3.3.1 Time evolution of Neutrino spectrum	30
3.3.2 Neutrino thermalization and neutron to proton ratio	35
3.3.3 Neutrino thermalization and light element abundances	39
3.4 Hadron injection by massive particle decay	43
3.4.1 Hadron Jets and $e^+e^-$ collider experiments	43
3.4.2 Formulation in Hadron Injection Scenario	45
3.4.3 Hadron injection and BBN	48
3.4.4 Summary of hadron injection	53
3.5 Constraints from Large Scale Structure and CMB anisotropy	53
3.6 Lower bound of reheating temperature : Summary	61

<b>4 Hadron injection from Primordial Black holes and BBN</b>	<b>62</b>
4.1 Evaporation of Primordial Black Hole and BBN : overview	62
4.2 Evaporation and Jets	65
4.3 Hadron injection and BBN	68
4.3.1 Hadron scattering off the background particles	68
4.3.2 Formulation	70
4.3.3 Observational constraints	71
4.4 Results	72
4.5 Constraints of the PBH evaporation : summary	75
<b>5 Radiative decay of a long-lived massive particle and BBN</b>	<b>77</b>
5.1 BBN + X	77
5.1.1 Photon Spectrum	77
5.1.2 Abundance of Light Elements with X	78
5.1.3 Comparison with Observation	81
5.1.4 Additional Constraints	81
5.2 Models	88
5.3 The obtained constraints of the long-lived massive particles : summary	95
<b>6 Conclusion and Discussion</b>	<b>97</b>
6.1 Summary of conclusions	97
<b>A Neutrino decoupling from the thermal bath</b>	<b>101</b>
A.1 Neutrino decoupling temperature	101
<b>B Boltzmann equation for neutrino distribution functions</b>	<b>104</b>
B.1 Reduction of collision integral	104
<b>C Method of Maximal Likelihood Analysis</b>	<b>108</b>
C.1 $\chi^2$ Fitting in SBBN and SBBN+X	108

# Chapter 1

## Introduction

### 1.1 Overview

Today we have a standard theory of the universe which is called "Big bang model" and we believe it to be reliable because it stands on the three important observational evidences: i) the discovery of Hubble expansion law as a proof of the expanding universe [1], ii) the discovery of the cosmic microwave background radiation which is a vestige that once the universe started from the primordial fireball [2], and iii) the success of the primordial nucleosynthesis of the light elements (H, D,  $^4\text{He}$  and  $^7\text{Li}$ ), i.e. big bang nucleosynthesis (BBN) [3]. BBN is one of the strong tools to probe the early universe. Especially since it is very sensitive to the condition of the universe from  $10^{-2}$  sec to  $10^3$  sec, the history of the universe can be indirectly checked by the observational light element abundances which are measured precisely.

From the standpoint of the particle physics, we have an excellent theory, "Weinberg-Salam model" which is commonly called "Standard model (SM)" [4]. The theory unifies the electromagnetic interaction and weak interaction, and precisely predicts any phenomena up to about  $\mathcal{O}(\text{TeV})$  without a few exceptions [5]. Of course we should not forget there were big efforts to regularize ultraviolet divergences by using the dimensional regularization scheme [6] which appear in the most calculations in electroweak physics and the applications for the infrared divergence and mass singularities [7]. However, in other words, we can not understand the phenomena beyond the TeV scale, and probably we do not rely on any predictions in such a high energy scale very well because the application of the theory is extremely limited. One approach to search the new physics beyond the SM might be to try to unify the above electroweak theory and the strong interaction, or even the gravitational interaction, and to find some hints in such attempts.

The supersymmetric (SUSY) extension of the standard model is one of the attractive candidates of the new physics beyond it. In the minimal SUSY standard model (MSSM), three gauge coupling constants are unified at  $E \simeq 10^{16}\text{GeV}$  [8, 9] and the stability of the SM against the radiative corrections for Higgs mass is guaranteed excellently by the cancellation of the quadratic divergences between the fermion and the boson loops [10, 11]. The energy

scale needed for the verification of the above supersymmetric grand unification theory (SUSY GUT) is namely about  $10^{16}\text{GeV}$ . However, we can not expect that the collider experiments will reach such a high energy scale in the near future.

On the other hand, for last two decades it has been expected that to clarify the high energy physics including GUT would solve the problems in the early universe. For example, the first simple models of the baryogenesis which were proposed in the late 1970's [12] and the first ideas of the inflationary cosmology which were developed at the beginning of 1980's [13] were surely motivated by the application of GUT. Since that time, the developments in the cosmology are expected to elucidate the particle physics or the high energy physics, and the new disciplinary category "Particle cosmology" has been formed.

The purpose of this thesis is to search the high energy physics and find some hints of the new physics by applying BBN to the early universe. In local SUSY (i.e. supergravity) or superstring theory which is expected to be the candidate of the new physics beyond the SM, there are a lot of unstable massive particles, e.g. Polonyi, Moduli, and Dilaton, which have long lifetimes since they interact with the other particles only through the gravitational interaction. As we noted above, BBN is very sensitive to the contents in the early universe. Thus if the massive particles dominated the energy density in the universe, or if not so, they exist as a net fraction of the energy density in the BBN epoch, their subsequent decay influences the cosmic history and predictions of light element abundances, and then we can constrain their masses, lifetimes and the abundances by the observations.

Concretely, when the massive particle has a relatively short lifetime and decays just before the BBN epoch, the produced entropy would replace what used to be, and then we should be worried about the thermalization of the particle contents because the insufficient thermalization of the background particles will drastically change the standard scenario. For the relatively longer lifetime, i.e. when the massive particle decays after the BBN epoch, there exist the further severe troubles that the emitted high energy photons would destroy the light elements which have already been synthesized. They are very interesting and delicate problems for the cosmology and should be studied in detail.

From the point of view of an interdiscipline between the cosmology and the particle physics, the primordial black hole (PBH) would also be the interesting subjects. We believe that the PBHs originated from the density fluctuations which are produced by the primordial inflation. If PBHs evaporate around the BBN epoch, they radiate a variety of particles and it is expected to induce some dangerous effects and change the standard scenario. When we investigate the details of the physical mechanism and their evolution, and we compare them with the observations, we can obtain the useful informations on the primordial spectrum of density fluctuations and the nature of the high energy physics concerning the model of the inflation which produces them. It should be noted that it is quite a unique method to search the primordial density fluctuations on small scales and at present we do not have any other way to do.

## 1.2 Organization of this thesis

Here we outline the organization of this thesis. In Chapter 2, we review the standard big bang nucleosynthesis (SBBN). In this chapter we discuss the theory of SBBN and the recent observational data of the light element abundances (D,  $^4\text{He}$ ,  $^7\text{Li}$ , etc.). We also introduce the method of the statistical analysis for the data obtained by the theory and the observations. In Appendix A we discuss the neutrino decoupling in the standard big bang cosmology.

In Chapter 3, we investigate the late-time entropy production process due to the decay of the long lived massive particle. In this chapter we show how low the reheating temperature after the late-time entropy production can be observationally allowed comparing with the predictions of BBN, the large scale structure, and the anisotropy of the cosmic microwave background radiation. To describe the thermalization process of the neutrino background, we should formulate the Boltzmann equation for the neutrino distribution functions. In Appendix B, we introduce the formulation to derive a set of Boltzmann equations.

In Chapter 4, we investigate the effects on BBN by the evaporation of the primordial black holes. There we point out how important we should treat the hadron emission as a quark-gluon jet in the modern view of quantum chromodynamics (QCD) and we replace the old constraints of the primordial abundance of PBH which have been referred for about twenty years.

In Chapter 5, the radiative decay of the massive particle after the BBN epoch and its various effects on the light elements are investigated. In this chapter we obtain the upper bound of the reheating temperature after the primordial inflation which determines the initial abundance of the massive particle. In Appendix C, we show the method of  $\chi^2$  fitting commonly used in Chapter 2, 3 and 5.

Chapter 6 is devoted to the discussion and conclusion.

## Chapter 2

### Standard Big Bang Nucleosynthesis

We begin by reviewing standard big-bang nucleosynthesis (SBBN). We are interested in the light elements, since their primordial abundances can be estimated from observations. In particular, we check the consistency between the theoretical predictions and the observations for the following quantities:

$$y_2 = \text{D}/\text{H} = n_{\text{D}}/n_{\text{H}}, \quad (2.1)$$

$$Y = \rho_{^4\text{He}}/\rho_{\text{B}}, \quad (2.2)$$

$$y_6 = {}^6\text{Li}/\text{H} = n_{^6\text{Li}}/n_{\text{H}}, \quad (2.3)$$

$$r = n_{^3\text{He}}/n_{\text{D}}, \quad (2.4)$$

$$y_7 = {}^7\text{Li}/\text{H} = n_{^7\text{Li}}/n_{\text{H}}, \quad (2.5)$$

where  $n_i$  is the number density of an element  $i$ ,  $\rho_{^4\text{He}}$  is the energy density of  $^4\text{He}$ , and  $\rho_{\text{B}}$  is the total baryon energy density.

In this chapter, we first review the observations of the light elements, and the extrapolations back to the primordial abundances. Next, we describe our theoretical calculations of these abundances, by using standard big-bang theory. Finally, we compare the theoretical and observed light-element abundances to determine how well the SBBN theory works.

#### 2.1 Review of Observation

In this section we briefly show the current status of the observational light element abundances. Concerning the deuterium abundance, the primordial D/H is measured in the high redshift QSO absorption systems. For the most reliable D abundance, we adopt the following value which is obtained by the clouds at  $z = 3.572$  towards Q1937-1009 and at  $z = 2.504$  towards Q1009+2956 [15],

$$y_2^{\text{obs}} = (3.39 \pm 0.25) \times 10^{-5}. \quad (2.6)$$

On the other hand, recently the high deuterium abundance is reported in relatively low redshift absorption systems at  $z = 0.701$  towards Q1718+4807 [16],  $\text{D}/\text{H} = (2.0 \pm 0.5) \times 10^{-4}$ .

Another group also observes the clouds independently [17]. However, because they do not have full spectra of the Lyman series, the analyses would be unreliable. More recently Kirkman *et al.* [18] observed the quasar absorption systems at  $z = 2.8$  towards Q0130-4021 and they obtain the upper bound,  $D/H \lesssim 6.7 \times 10^{-5}$ . Moreover Molaro *et al.* reported  $D/H \simeq 1.5 \times 10^{-5}$  which was observed in the absorber at  $z = 3.514$  towards APM 08279+5255 although it has the large systematic errors in the hydrogen column density [21]. Considering the current situation, we do not adopt the high deuterium value in this thesis.

For  ${}^3\text{He}$ , we use the pre-solar measurements. In this thesis, we do not rely upon any models of galactic and stellar chemical evolution, because of the large uncertainty involved in extrapolating back to the primordial abundance. But it is reasonable to assume that  ${}^3\text{He}/D$  is an increasing function of the cosmic time, because D is the most fragile isotope, and it is certainly destroyed whenever  ${}^3\text{He}$  is destroyed. Using the solar-system data reanalyzed by Geiss [19], the  ${}^3\text{He}/D$  ratio is estimated to be [20]

$$r_{\odot}^{obs} \equiv \left( y_3^{obs} / y_2^{obs} \right)_{\odot} = 0.591 \pm 0.536, \quad (2.7)$$

where  $\odot$  denotes the pre-solar abundance. We take this to be an upper bound on the primordial  ${}^3\text{He}$  to D ratio:

$$r^{obs} < r_{\odot}^{obs}. \quad (2.8)$$

Because the theoretical prediction of  ${}^3\text{He}/D$  in SBBN agrees so well with this upper bound, we do not include this constraint in the SBBN analysis. But when we investigate the photodissociation scenario in Chapter 5, the situation is quite different.  ${}^4\text{He}$  photodissociation produces both D and  ${}^3\text{He}$  and can raise the  ${}^3\text{He}$  to D ratio [20]. Hence, only in the analysis of BBN with photodissociation in Chapter 5, we include this upper bound, as described in the appendix (see Eq. (C.5)).

The primordial  ${}^4\text{He}$  mass fraction  $Y_p$  is observed in the low metallicity extragalactic HII regions. Since  ${}^4\text{He}$  is produced with Oxygen in the star, the primordial value is obtained to regress to the zero metallicity  $O/H \rightarrow 0$  for the observational data. Using the 62 blue compact galaxies (BCG) observations, it was reported that the primordial  $Y$  is relatively "low",  $Y_p \simeq 0.234$  [22]. However, recently it is claimed that HeI stellar absorption is an important effect though it was not included in the previous analysis properly [23]. They found the relatively "high" primordial value,  $Y_p = 0.245 \pm 0.004$ . More recently Fields and Olive [24] also reanalyze the data including the HeI absorption effect and they obtain

$$Y^{obs} = 0.238 \pm (0.002)_{stat} \pm (0.005)_{syst}, \quad (2.9)$$

where the first error is the statistical uncertainty and the second error is the systematic one. We adopt the above value as the observational  $Y_p$ .

The primordial  ${}^7\text{Li}/H$  is observed in the Pop II old halo stars. In general a halo star whose surface effective temperature is low (the mass is small), has the deep convective zone.

For such a low temperature star, the primordial  ${}^7\text{Li}$  is considerably depleted in the warm interior of the star. On the other hand for the high temperature stars ( $T_{eff} \gtrsim 5500\text{K}$ ), it is known that the primordial abundance is not changed and they have a "plateau" of the  ${}^7\text{Li}$  as a function of the effective temperature. In addition, though it is also known that  ${}^7\text{Li}/H$  decreases with decreasing  $\text{Fe}/H$ ,  ${}^7\text{Li}$  still levels off at lower metallicity,  $[\text{Fe}/H] \lesssim -1.5$ , in the plateau stars. We adopt the recent measurements which are observed by Bonifacio and Molaro [25]. They observed 41 old halo stars which have the plateau and they argued that the data provides no evidence for  ${}^7\text{Li}/H$  depletion in the stellar atmospheres (caused by, *e.g.*, stellar winds, rotational mixing, or diffusion). However, for our analysis, we shall adopt the more cautious estimate of Hogan [26] that  ${}^7\text{Li}$  may have been supplemented (by production in cosmic-ray interactions) or depleted (in stars) by a factor of two: [27]. Then we obtain

$$\log_{10}(y_7^{obs}) = -9.76 \pm (0.012)_{stat} \pm (0.05)_{syst} \pm (0.3)_{add}. \quad (2.10)$$

Because  ${}^6\text{Li}$  is so much rarer than  ${}^7\text{Li}$ , it is much more difficult to observe. Currently, there is insufficient data to find the "Spite plateau" of  ${}^6\text{Li}$ . However, we can set an upper bound on  ${}^6\text{Li}/{}^7\text{Li}$ , since it is generally agreed that the evolution of  ${}^6\text{Li}$  is dominated by production by spallation (reactions of cosmic rays with the interstellar medium). The upper bounds on  ${}^6\text{Li}/{}^7\text{Li}$  observed in low-metallicity ( $[\text{Fe}/H] \leq -2.0$ ) halo stars range from [28]  $y_6/y_7 \lesssim 0.045$  to  $y_6/y_7 \lesssim 0.13$ . (Note that the primordial  ${}^6\text{Li}$  and  ${}^7\text{Li}$  have both been destroyed in material which has been processed by stars.)

Rotational mixing models [29] yield a survival factor for  ${}^7\text{Li}$  of order 0.05 and a survival factor for  ${}^6\text{Li}$  of order 0.005. Therefore, the upper bound for primordial  ${}^6\text{Li}/{}^7\text{Li}$  ranges approximately from

$$y_6^{obs}/y_7^{obs} \lesssim 0.5 \text{ to } 1.3. \quad (2.11)$$

Since we have only a rough range of upper bounds on  ${}^6\text{Li}$ , and no lower bound, we will not use  ${}^6\text{Li}$  in our statistical analysis to test the concordance between observation and theory. Of course SBBN satisfies the constraint. Instead, for the photo-dissociation scenario in Chapter 5, we will just check the consistency of our theoretical results with the above constraint.

## 2.2 Review of theory in SBBN

### 2.2.1 Thermal history

In this subsection we briefly review the thermal history around the BBN epoch. In standard big bang cosmology we believe that photon, electrons, three neutrinos, and nucleons are in thermal equilibrium at a high temperature  $T \gtrsim 10\text{MeV}$ . First we especially pay attention to neutrinos. At  $T \gtrsim$  a few MeV, they are kept in thermal equilibrium through the weak in-

interaction,  $\nu\bar{\nu} \leftrightarrow e^+e^-$ ,  $\nu e \leftrightarrow \nu e$ , etc. The magnitude of the weak interaction is approximately given by  $\Gamma_{int} = n\sigma|v| \simeq G_F^2 T^5$ , where  $G_F$  is Fermi coupling constant. On the other hand, the Hubble expansion rate is given by,  $H \simeq T^2/m_{pl}$  in radiation dominated epoch. Therefore these equations tell us that,  $\Gamma_{int}/H \simeq G_F^2 m_{pl} T^3$ . As temperature decrease, this ratio will become smaller than unity. Then the neutrinos no longer interact with the thermal bath. For each neutrino species, the decoupling temperatures  $T_D$  are estimated as,  $T_D \simeq 2.2$  MeV for  $\nu_e$  and  $T_D \simeq 3.3$  MeV for  $\nu_\mu$  and  $\nu_\tau$ , see Appendix A for detailed computations.

The decoupling temperature of the electron neutrino is lower than that of  $\nu_\mu$  and  $\nu_\tau$ . This is because there are a lot of background electrons at that time. Although  $\nu_\mu$  and  $\nu_\tau$  interact only through the neutral current interaction with the background electrons, the electron neutrino can interact through both the neutral current interaction and charged current interaction with the electrons. For the above reason, the magnitude of interaction for the electron neutrino is larger than  $\nu_\mu$  and  $\nu_\tau$ , and the interaction of  $\nu_e$  continues later than that of  $\nu_\mu$  and  $\nu_\tau$ . Since the decoupling, the neutrino temperature  $T_\nu$  exactly scales as  $R(t)^{-1}$  where  $R(t)$  is the scale factor.

When the temperature approximately drops below the electron mass  $m_e$  ( $\simeq 0.511$  MeV), the electron and the positron begin to annihilate, and their entropy is converted to the photons. However neutrinos are not heated because they have already decoupled from the thermal bath. For  $T \gtrsim m_e$ , the statistical degree of freedom of the relativistic particles except neutrinos in the thermal bath is  $g_* = 11/2$ . On the contrary, for  $T \lesssim m_e$  only the photon contributes to it, i.e.  $g_* = 2$ . As the universe adiabatically expands, the value  $g_* T^3 R^3$  should be conserved. Namely after the  $e^+e^-$  annihilation, the temperature of photon  $T_\gamma$  is heated by a factor of third-root of the ratio of  $g_*$ . Since the neutrino temperature  $T_\nu$  is not changed, the ratio of  $T_\gamma$  to  $T_\nu$  is given by,

$$\frac{T_\gamma}{T_\nu} = \left(\frac{11}{4}\right)^{1/3} \simeq 1.40. \quad (2.12)$$

Today the temperature of the cosmic microwave background photon is accurately observed that  $T_{\gamma,0} \simeq 2.74$  K [30]. Then Eq. (2.12) indirectly predicts that there also exists the neutrino background whose temperature is  $T_{\nu,0} \simeq 1.96$  K at present. The evolution of the temperature of photon and that of neutrinos is shown in Fig. 2.1. The big bang nucleosynthesis starts under such circumstances.

## 2.2.2 Nuclear Statistical Equilibrium

Standard big bang scenario tells us that once the universe was in thermal equilibrium, and then the universe have experienced a history that the particles had gradually decoupled from the thermal equilibrium. In that picture we begin to discuss the standard big bang nucleosynthesis (SBBN). Here we consider the nuclear statistical equilibrium (NSE) and

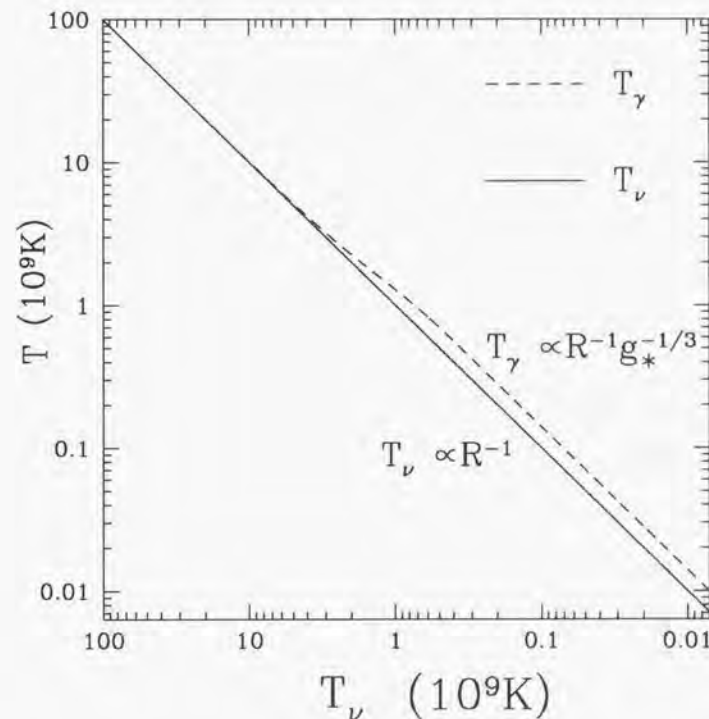


Figure 2.1: Evolution of  $T_\gamma$  and  $T_\nu$  around  $e^\pm$  annihilation epoch. The solid line denotes the neutrino temperature which exactly scales as  $\propto R^{-1}$  and the dashed line denotes the photon temperature. ( $10^9$  K  $\simeq 0.086$  MeV)

its consequences. In *kinetic equilibrium* the number density of a non-relativistic particle ( $m_A \gg T$ ) is given by

$$n_A = \frac{g_A}{2\pi} \int_{m_A}^{\infty} \frac{(E^2 - m_A^2)^{1/2}}{\exp[(E - \mu_A)/T] \pm 1} E^2 dE, \quad (2.13)$$

$$\simeq g_A \left( \frac{m_A T}{2\pi} \right)^{3/2} \exp\left( \frac{\mu_A - m_A}{T} \right), \quad (2.14)$$

where  $A$  denotes the nucleon mass number,  $g_A$  is the statistical degree of freedom, and  $\mu_A$  is the chemical potential. When the reaction is enough rapid compared to the Hubble expansion rate  $H$ , the *chemical equilibrium* is realized.

$$\mu_A = Z\mu_p + (A - Z)\mu_n, \quad (2.15)$$

where  $Z$  is the atomic number. When the reaction is in NSE, the forward reaction is equal to the reverse one. From Eqs. (2.14), (2.15) and (2.17) the number density is obtained as,

$$n_A = g_A A^{3/2} 2^{-A} \left( \frac{2\pi}{m_N T} \right)^{3(A-1)/2} n_p^Z n_n^{A-Z} \exp(B_A/T), \quad (2.16)$$

where  $B_A$  is the binding energy which is defined by

$$B_A = Zm_p + (A - Z)m_n - m_A. \quad (2.17)$$

Since the differences among  $m_n$ ,  $m_p$  and  $m_A/A$  are not important in the pre-exponential factor, we identify them as a nuclear mass unit  $m_N \equiv {}^{12}\text{C}/12 \simeq 931.5 \text{ MeV}$ .

Here it is useful to define the mass fraction  $X_i$  by

$$X_i \equiv \frac{n_A A}{n_N}, \quad (2.18)$$

where  $n_N$  is the total nucleon number density, and  $\sum_i X_i = 1$  by definition. Using the mass fraction  $X_A$ , Eq.(2.16) gives

$$X_A = g_A C(A) A^{3/2} \left( \frac{T}{m_N} \right)^{3(A-1)/2} \eta^{A-1} X_p^Z X_n^{A-Z} \exp\left( \frac{B_A}{T} \right), \quad (2.19)$$

where  $C(A) = 2^{(3A-1)/2} \pi^{(1-A)/2} \zeta(3)^{A-1}$ ,  $\zeta(3) \simeq 1.202$ , and the baryon to photon ratio  $\eta$  is defined by

$$\eta \equiv n_B/n_\gamma \simeq 2.73 \times 10^{-8} (\Omega_B h^2) \left( \frac{T_{90}}{2.74 \text{ K}} \right)^{-3}, \quad (2.20)$$

where the baryon density parameter is defined by  $\Omega_B \equiv \rho_B/\rho_c$ ,  $\rho_c$  is the critical density, and  $h$  is defined by  $H_0 = 100h \text{ km/s/Mpc}$ . In Eq. (2.19) we find there exists  $\eta$  in pre-exponential factor and it leads to the characteristic effect in the production of D. The binding energy of

D is so low ( $B_2 \simeq 2.2 \text{ MeV}$ ) that an adequate abundance of deuterium is not produced until  $T \lesssim 0.1 \text{ MeV}$ , and it delays the onset of the further nuclear reactions. This effect is called "*deuterium bottleneck*". Namely it is caused by large  $n_\gamma$  or the large entropy in the universe compared to  $n_B$ .

### 2.2.3 Neutron to proton ratio

At a high temperature ( $T \gg 1 \text{ MeV}$ ), the following weak interactions are rapid enough to keep the neutron and proton in statistical equilibrium.

$$n \leftrightarrow p + e^- + \bar{\nu}_e \quad (2.21)$$

$$n + \nu_e \leftrightarrow p + e^- \quad (2.22)$$

$$n + e^+ \leftrightarrow p + \bar{\nu}_e \quad (2.23)$$

These reaction rates are given by

$$\Gamma_{n \rightarrow p + e^- + \bar{\nu}_e} = C \int_1^q \frac{\epsilon \sqrt{\epsilon^2 - 1} (\epsilon - q)^2}{(1 + \exp(-\epsilon z))(1 + \exp((\epsilon - q)z_\nu))} d\epsilon, \quad (2.24)$$

$$\Gamma_{n + \nu_e \rightarrow p + e^-} = C \int_q^\infty \frac{\epsilon \sqrt{\epsilon^2 - 1} (\epsilon - q)^2}{(1 + \exp(-\epsilon z))(1 + \exp((\epsilon - q)z_\nu))} d\epsilon, \quad (2.25)$$

$$\Gamma_{n + e^+ \rightarrow p + \bar{\nu}_e} = C \int_1^\infty \frac{\epsilon \sqrt{\epsilon^2 - 1} (\epsilon + q)^2}{(1 + \exp(\epsilon z))(1 + \exp(-(\epsilon + q)z_\nu))} d\epsilon, \quad (2.26)$$

$$\Gamma_{p + e^- + \bar{\nu}_e \rightarrow n} = C \int_1^q \frac{\epsilon \sqrt{\epsilon^2 - 1} (\epsilon - q)^2}{(1 + \exp(\epsilon z))(1 + \exp(-(\epsilon - q)z_\nu))} d\epsilon, \quad (2.27)$$

$$\Gamma_{p + e^- \rightarrow n + \nu_e} = C \int_q^\infty \frac{\epsilon \sqrt{\epsilon^2 - 1} (\epsilon - q)^2}{(1 + \exp(\epsilon z))(1 + \exp(-(\epsilon - q)z_\nu))} d\epsilon, \quad (2.28)$$

$$\Gamma_{p + \bar{\nu}_e \rightarrow e^+ + n} = C \int_1^\infty \frac{\epsilon \sqrt{\epsilon^2 - 1} (\epsilon + q)^2}{(1 + \exp(-\epsilon z))(1 + \exp((\epsilon + q)z_\nu))} d\epsilon, \quad (2.29)$$

where  $C = \frac{G_F^2}{2\pi^3} (1 + 3c_A^2) m_e^5$ ,  $q = Q/m_e$ ,  $Q = m_n - m_p = 1.293 \text{ MeV}$ ,  $\epsilon = E_e/m_e$ ,  $z = m_e/T_e$ , and  $z_\nu = m_e/T_\nu$ .  $c_A$  is axial vector coupling constant ( $\sim 1.26$ ) and  $G_F$  is Fermi coupling constant. Of course Eq. (2.24) gives the neutron free decay rate  $1/\tau_n$  at  $T \rightarrow 0$ . Here we consider the neutron forward reaction rate  $\Gamma_{n \rightarrow p}$  and the reverse reaction rate  $\Gamma_{p \rightarrow n}$  which are defined by

$$\Gamma_{n \rightarrow p} \equiv \Gamma_{n \rightarrow p + e^- + \bar{\nu}_e} + \Gamma_{n + \nu_e \rightarrow p + e^-} + \Gamma_{n + e^+ \rightarrow p + \bar{\nu}_e}, \quad (2.30)$$

$$\Gamma_{p \rightarrow n} \equiv \Gamma_{p + e^- + \bar{\nu}_e \rightarrow n} + \Gamma_{p + e^- \rightarrow n + \nu_e} + \Gamma_{p + \bar{\nu}_e \rightarrow e^+ + n}. \quad (2.31)$$

At a higher temperature ( $z, z_\nu \ll 1$ ) we approximately obtain

$$\frac{\Gamma_{n \rightarrow p}}{\Gamma_{p \rightarrow n}} \simeq \exp\left( -\frac{Q}{T} \right). \quad (2.32)$$

This means the principle of detailed balance. The differential equation of neutron mass fraction is given by

$$\frac{dX_n}{dt} = -\Gamma_{n \rightarrow p} X_n + \Gamma_{p \rightarrow n} (1 - X_n). \quad (2.33)$$

In thermal equilibrium,  $dX_n/dt = 0$  and then the above equation tells us that  $X_n$  is given by

$$X_n = \frac{\Gamma_{p \rightarrow n}}{\Gamma_{p \rightarrow n} + \Gamma_{n \rightarrow p}} \quad (2.34)$$

$$= \frac{1}{1 + \left(\frac{\Gamma_{n \rightarrow p}}{\Gamma_{p \rightarrow n}}\right)^{-1}}. \quad (2.35)$$

On the other hand, by definition the neutron mass fraction  $X_n$  is given by

$$X_n = \frac{n_n}{n_n + n_p}, \quad (2.36)$$

$$= \frac{1}{1 + \left(\frac{n_n}{n_p}\right)^{-1}}. \quad (2.37)$$

From Eqs. (2.32), (2.35) and (2.37), in thermal equilibrium the neutron to proton ratio  $n/p$  is estimated as

$$\left(\frac{n}{p}\right)_{\text{EQ}} = \exp\left(-\frac{Q}{T}\right). \quad (2.38)$$

The above relation is also obtained from Eq. (2.14) for neutron and proton. Eq. (2.38) tells us that the initial value of  $n/p$  is close to unity, and as the temperature of the universe decreases, the neutron to proton ratio decreases exponentially in thermal equilibrium.

## 2.2.4 Freeze-out of $n/p$

Here we compare the time scale of the weak interaction rate of nucleons with the Hubble expansion rate. As we mentioned in the previous subsection, the neutron life time  $\tau_n$  at  $T \sim 0$  controls the magnitude of the weak interaction rates at a finite temperature as

$$\frac{1}{\tau_n} = \Gamma_{n \rightarrow p + e^- + \bar{\nu}_e}(T=0) = \frac{G_F^2}{2\pi^3} (1 + 3c_A^2) m_e^5 \lambda_0, \quad (2.39)$$

where

$$\lambda_0 \equiv \int_1^q \epsilon(\epsilon - q)^2 (\epsilon^2 - 1)^{1/2} d\epsilon \simeq 1.636. \quad (2.40)$$

Then we can represent all six reaction rates (Eqs. (2.24) - (2.29)) using  $\tau_n$  which is measured by the experiments. For example at a high temperature we have

$$\Gamma_{n + e^+ \rightarrow p + \bar{\nu}_e} = (\tau_n \lambda_0)^{-1} \int_q^\infty d\epsilon \frac{\epsilon(\epsilon - q)^2 (\epsilon - 1)^{1/2}}{[1 + \exp(\epsilon z)] [1 + \exp((q - z) z_{nu})]} \quad (2.41)$$

$$\rightarrow \frac{7}{60} \pi (1 + 3c_A) G_F^2 T^5 \quad (T \gg Q, m_e). \quad (2.42)$$

This interaction rate should be compared to the Hubble expansion rate  $H(T)$ . If the ratio to the  $H(T)$  is larger than unity, the interaction is sufficiently rapid. On the other hand, if it is less than unity, we regard the reaction as freeze-out. The Hubble expansion rate is expressed by

$$H(T) \simeq 1.66 g_* T^2 / m_{pl}, \quad (2.43)$$

where  $g_*$  is the statistical degree of freedom and  $m_{pl} = 1/\sqrt{G}$  is Planck mass. From Eqs. (2.42) and (2.43) approximately we find

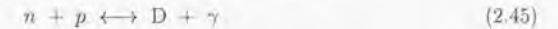
$$\frac{\Gamma_{n \rightarrow p}(T)}{H(T)} \simeq \left(\frac{T}{0.8 \text{ MeV}}\right)^3. \quad (2.44)$$

Eq. (2.44) tells us that if the temperatures is higher than the freeze-out temperature  $T_f \simeq 0.8$  MeV, the inter-converting reaction between neutron and proton is faster than the Hubble expansion rate and the  $n/p$  changes following Eq. (2.38). However, if the temperature is below  $T_f$ , the inter-converting reaction decouples and  $n/p$  is almost freeze-out. In other words, at that time the primordial neutron abundance was determined approximately. Then only the free decay decreases the neutron abundance a little.

In Fig. 2.2 we plot the time evolution of the neutron to proton ratio. The NSE value of  $n/p$  is represented by the dashed line. At about  $T \simeq 0.07$  MeV neutrons are almost included in nuclears and the free neutrons disappear from the background.

## 2.2.5 Production of light elements

As we mentioned in the previous subsections, as it were, the big bang cosmology is the history that the particles have departed from the NSE tracks. As the temperature decreases, the most reaction rates of the light elements gradually decouple. However, interestingly the production rate of deuterium is almost in NSE during the BBN epoch.



From Eq. (2.19) the NSE value of D is estimated by

$$X_2 = 16.3 \left(\frac{T}{m_N}\right)^{\frac{3}{2}} \eta \exp\left(\frac{B_2}{T}\right) X_n X_p, \quad (2.46)$$

where  $B_2 \simeq 2.22$  MeV. At  $T \simeq 1$  MeV the deuterium mass fraction  $X_2$  is about ten orders of magnitude smaller than the proton and neutron abundances. However, as the temperature decreases below about  $T \simeq 100$  keV, the NSE value of D can reach just the two orders of magnitude smaller than that of nucleons. Then deuteriums are used as materials to build

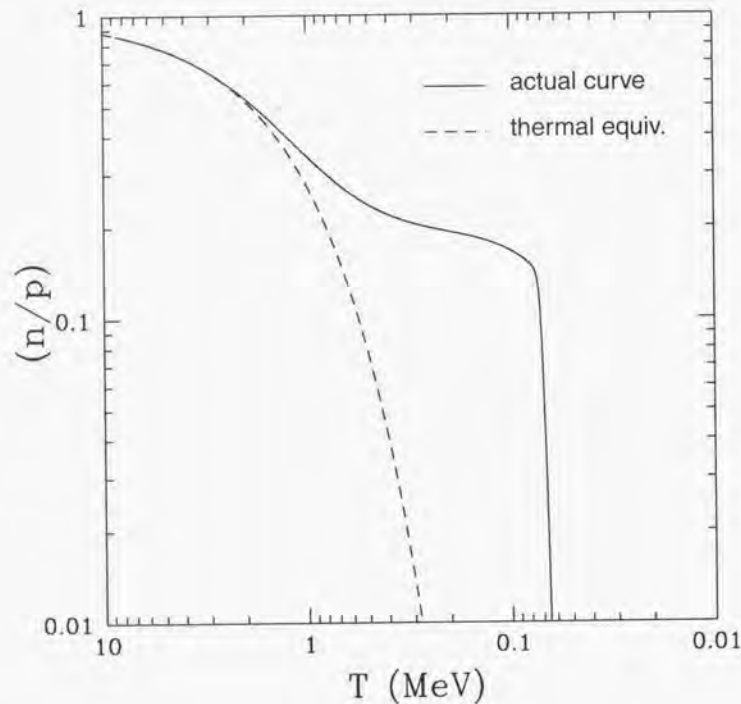
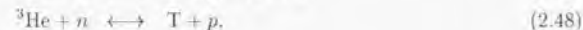
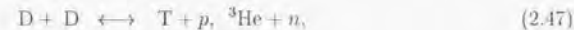


Figure 2.2: Time evolution of the neutron to proton ratio. The dashed curve denotes the nuclear statistical equilibrium (NSE). The solid curve denotes the actual curve in SBBN.

the following mass-3 and mass-4 light elements.



and



These interaction rates are rapid enough to proceed the nuclear reactions compared to the Hubble expansion rate. Thus most neutrons are changed into  ${}^4\text{He}$  through D. Therefore using an intuitive estimation,  ${}^4\text{He}$  mass fraction can be approximately given by

$$X_4 = \frac{4m_N n_3}{m_N n_N} = \frac{4n_n/2}{n_p + n_n} = \frac{2(n/p)_{nuc}}{1 + (n/p)_{nuc}}, \quad (2.51)$$

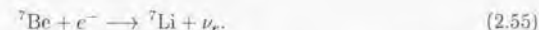
$$\sim 0.250, \quad (2.52)$$

where  $(n/p)_{nuc} \sim 1/7$  represents the neutron to proton ratio at the time when  ${}^4\text{He}$  synthesis takes place ( $T \sim 0.1$  MeV).

Through these processes, D and  ${}^3\text{He}$  which could not burn into  ${}^4\text{He}$  remain as the burned embers. Since there is no stable nucleus whose mass number is 5 or 8, the nucleus whose mass number is larger than 8 is not produced very much in the BBN epoch. However, only  ${}^7\text{Li}$  and  ${}^7\text{Be}$  are produced a little through the following reactions,



${}^7\text{Be}$  is changed to  ${}^7\text{Li}$  through the electron capture reaction,



Here we view the history as a series of the departures from NSE. At  $T \gtrsim 0.6$  MeV,  ${}^4\text{He}$  is in NSE with  ${}^3\text{He}$  and T, and  ${}^3\text{He}$  is in NSE with T. Both  ${}^3\text{He}$  and T are in NSE with D, and D is in NSE with neutron and proton. From Eq. (2.19) their NSE values are given by (2.46) and

$$X_t = 57.4 \left(\frac{T}{m_N}\right)^3 \eta^2 \exp\left(\frac{B_t}{T}\right) X_n^2 X_p, \quad (2.56)$$

$$X_3 = 57.4 \left(\frac{T}{m_N}\right)^3 \eta^2 \exp\left(\frac{B_3}{T}\right) X_n X_p^2, \quad (2.57)$$

$$X_i = 113 \left( \frac{T}{m_N} \right)^{3/2} \eta^3 \exp \left( \frac{B_i}{T} \right) X_n^2 X_p^2, \quad (2.58)$$

where  $t$ , 3, and 4 denote tritium,  ${}^3\text{He}$  and  ${}^4\text{He}$ . The binding energy  $B_i$  is shown in Table 2.1. In Fig. 2.3 we plot the evolution curve of the light elements (n, p, D, T,  ${}^3\text{He}$ ,  ${}^4\text{He}$ ,  ${}^6\text{Li}$ ,  ${}^7\text{Li}$

${}^A_Z$	$B_A$	$g_A$
${}^2\text{H}$ (D)	2.22 MeV	3
${}^3\text{H}$ (T)	8.48 MeV	2
${}^3\text{He}$	7.72 MeV	2
${}^4\text{He}$	28.3 MeV	1
${}^{12}\text{C}$	92.2 MeV	1

Table 2.1: The binding energies of light elements

and  ${}^7\text{Be}$ ) as a function of the temperature. The solid lines denote the time evolution of their mass fractions. The four dashed lines are the nuclear statistical equilibrium values for D, T,  ${}^3\text{He}$  and  ${}^4\text{He}$ , when we assume that the neutron abundance is constant. From Fig. 2.3 we find that since the NSE curve of  ${}^4\text{He}$  is very steep, it would have dominated other elements much earlier ( $T \gtrsim 0.3\text{MeV}$ ), if there were enough materials ( ${}^3\text{He}$  and T).

At  $T \sim 0.6\text{MeV}$  the actual curve of  ${}^4\text{He}$  begins to depart from the NSE curve because of the following reasons. The NSE curves of mass-4 and mass-3 cross at  $T \sim 0.6\text{MeV}$ .  ${}^3\text{He}$  and T are still kept in NSE each other through  $\text{T}(p, n){}^3\text{He}$  or through D reactions  $\text{D}(n, \gamma)\text{T}$  and  $\text{D}(p, \gamma){}^3\text{He}$ . On the contrary, the reactions  ${}^3\text{He}(n, \gamma){}^4\text{He}$  and  $\text{T}(p, \gamma){}^4\text{He}$  which produce  ${}^4\text{He}$  are no longer as rapid as the Hubble expansion rate. Therefore the actual  ${}^4\text{He}$  curve follows the mass-3 NSE curves until about 0.2 MeV. This effect is “*mass-3 bottle neck*” which prevents  ${}^4\text{He}$  from dominating other elements.

At  $T \sim 0.2\text{MeV}$  the reactions  $\text{D}(n, \gamma)\text{T}$  and  $\text{D}(p, \gamma){}^3\text{He}$  which keep both tritium and  ${}^3\text{He}$  in NSE through D, are no longer rapid relative to the Hubble expansion rate. The actual tritium and  ${}^3\text{He}$  curves depart from NSE tracks and begin to follow to the deuterium NSE curve. Namely since that time, T,  ${}^3\text{He}$ , and  ${}^4\text{He}$  should wait for the deuterium to be completed. Even below this temperature, however, T and  ${}^3\text{He}$  are still in thermal equilibrium each other only through  $\text{T}(p, n){}^3\text{He}$ . Because the binding energy of T is larger than  ${}^3\text{He}$ , the abundance of  ${}^3\text{He}$  is suppressed compared to tritium abundance until about 0.08 MeV.

At  $T \sim 0.08\text{MeV}$ , the reaction rate of  $\text{T}(p, n){}^3\text{He}$  becomes slower than the Hubble expansion rate. And soon after then, at last D departs from its NSE track (at about 0.07 MeV).

In this way, most neutrons are included into  ${}^4\text{He}$ , and in succession D, T and  ${}^3\text{He}$  collide to the existing  ${}^4\text{He}$  and produce the larger mass number nuclei,  ${}^6\text{Li}$ ,  ${}^7\text{Li}$ , and  ${}^7\text{Be}$ . These elements are in quasi-static equilibrium (QSE) as well as D, T and  ${}^3\text{He}$ . Although NSE means the status that the forward reaction rate is equal to the reverse rate, QSE means the

status that the magnitude of the total forward reactions is almost equal to the magnitude of the total reverse reactions. Generally the reaction of a nuclide  $i$  is following to a set of differential equations which are given by,

$$\frac{dY_i}{dt} = \sum_{k,l} Y_k Y_l \Gamma_{k,l}^i - \sum_j Y_i Y_j \Gamma_{i,j}^d, \quad (2.59)$$

where  $Y_i \equiv X_i/A_i$ ,  $A_i$  is the mass number of nuclide  $i$ ,  $\Gamma_{k,l}^i$  is the creation rate of a nuclide  $i$  from the nuclide  $k$  and  $l$ , and  $\Gamma_{i,j}^d$  is the destruction rate of the nuclide  $i$  into  $j$ . In QSE, the left hand side of the equation is zero and we obtain

$$Y_i(T) = \frac{\sum_{k,l} Y_k(T) Y_l(T) \Gamma_{k,l}^i(T)}{\sum_j Y_j(T) \Gamma_{i,j}^d(T)}. \quad (2.60)$$

The condition of QSE is maintained while the reaction rate  $\Gamma_{i,j}^d(T)$  is rapid enough compared to expansion rate. As the temperature fall down, the rate becomes weaker and the abundance of the nuclide  $i$  freezes out. We find each freeze-out temperature in Table 2.2.

${}^A_Z$	Freeze-out Temperature
${}^2\text{H}$ (D)	30 keV
${}^3\text{H}$ (T)	9.0 keV
${}^3\text{He}$	30 keV
${}^4\text{He}$	60 keV
${}^7\text{Li}$	20 keV
${}^7\text{Be}$	20 keV

Table 2.2: Freeze-out temperature of light elements

## 2.3 Monte Carlo simulation

Theoretically, the primordial abundances of the light elements in SBBN depend only upon a single parameter: the baryon to photon ratio  $\eta$ . In our analysis, we modified Kawano’s nucleosynthesis code [31] to calculate the primordial light-element abundances and uncertainties.

In our calculation, we included the uncertainty in the neutron lifetime [32], in the rates of the 11 most important nucleosynthesis reactions [33].<sup>1</sup> We treated the neutron lifetime, the nucleosynthesis reaction rates as independent random variables with Gaussian probability density functions (p.d.f.’s). We performed a Monte-Carlo<sup>2</sup> over the neutron lifetime, nucle-

<sup>1</sup>In Chapter 5 we will consider the photo-dissociation of the light elements. In the chapter we also adopt the same treatments for the rates of the photofission reactions (see Table 5.1).

<sup>2</sup>It has recently been demonstrated that the uncertainties only in SBBN can be quantified by the much quicker method of linear propagation of errors. [34]

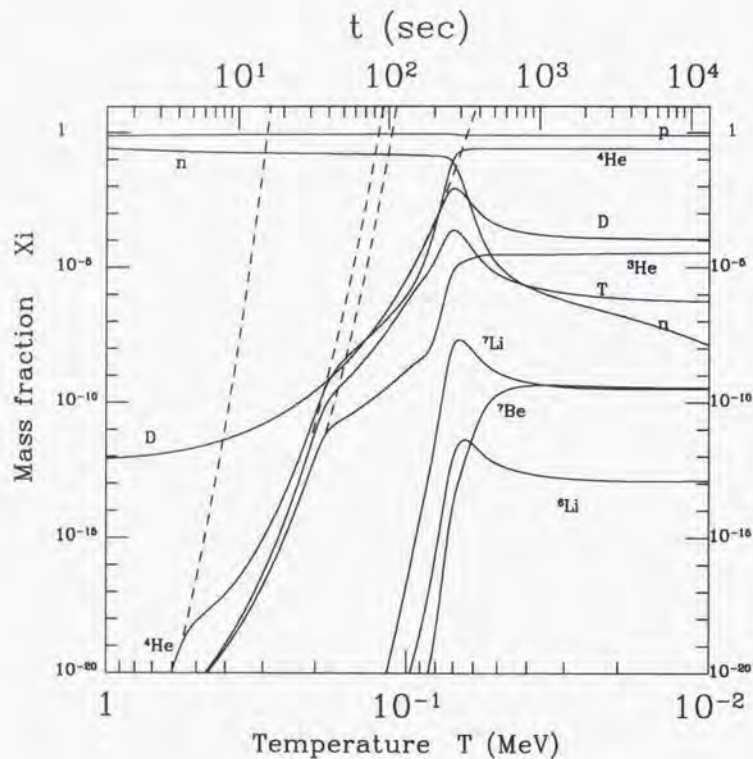


Figure 2.3: Time evolution of the light element abundances at  $\eta = 3.162 \times 10^{-10}$ . The dashed line denotes the nuclear statistical equilibrium value of each light element.

osynthesis reaction rates, and we found that the light-element abundances were distributed approximately according to independent, Gaussian p.d.f.'s (see Fig. 2.4). Therefore, the p.d.f.  $p_{tot}^{th}$  for the theoretical abundances is given by the product of the Gaussian p.d.f.'s

$$p^{Gauss}(x; \bar{x}, \sigma) = \frac{1}{\sqrt{2\pi}\sigma} \exp\left[-\frac{1}{2}\left(\frac{x-\bar{x}}{\sigma}\right)^2\right] \quad (2.61)$$

for the individual abundances:

$$p_{tot}^{th}(y_2^{th}, Y^{th}, \log_{10} y_7^{th}) = p_2^{Gauss}(y_2^{th}) \times p_1^{Gauss}(Y^{th}) \times p_7^{Gauss}(\log_{10} y_7^{th}). \quad (2.62)$$

In Fig. 2.5, we have plotted the theoretical predictions for the light-element abundances (solid lines) with their one-sigma errors (dashed lines), as functions of  $\eta$ .

The dependences of the abundances on  $\eta$  can be seen intuitively [35, 36]. The  ${}^4\text{He}$  abundance is a gentle, monotonically increasing function of  $\eta$ . As  $\eta$  increases,  ${}^4\text{He}$  is produced earlier because the "deuterium bottleneck" is overcome at a higher temperature due to the higher baryon density. Fewer neutrons have had time to decay, so more  ${}^4\text{He}$  is synthesized. Since  ${}^4\text{He}$  is the most tightly bound of the light nuclei, D and  ${}^3\text{He}$  are fused into  ${}^4\text{He}$ . The surviving abundances of D and  ${}^3\text{He}$  are determined by the competition between their destruction rates and the expansion rate. The destruction rates are proportional to  $\eta$ , so the larger  $\eta$  is, the longer the destruction reactions continue. Therefore, D and  ${}^3\text{He}$  are monotonically decreasing functions of  $\eta$ . Moreover, the slope of D is steeper, because the binding energy of D is smaller than  ${}^3\text{He}$ .

The graph of  ${}^7\text{Li}$  has a "trough" near  $\eta \sim 3 \times 10^{-10}$ . For a low baryon density  $\eta \lesssim 3 \times 10^{-10}$ ,  ${}^7\text{Li}$  is produced by  ${}^4\text{He}(T, \gamma){}^7\text{Li}$  and is destroyed by  ${}^7\text{Li}(p, \alpha){}^4\text{He}$ . As  $\eta$  increases, the destruction reaction becomes more efficient and the produced  ${}^7\text{Li}$  tends to decrease. On the other hand for a high baryon density  $\eta \gtrsim 3 \times 10^{-10}$ ,  ${}^7\text{Li}$  is mainly produced through the electron capture of  ${}^7\text{Be}$ , which is produced by  ${}^3\text{He}(\alpha, \gamma){}^7\text{Be}$ . Because  ${}^7\text{Be}$  production becomes more effective as  $\eta$  increases, the synthesized  ${}^7\text{Li}$  increases. The "trough" results from the overlap of these two components. The dominant source of  ${}^6\text{Li}$  in SBBN is  $D(\alpha, \gamma){}^6\text{Li}$ . Thus, the  $\eta$  dependence of  ${}^6\text{Li}$  resembles that of D.

We have also plotted the  $2\text{-}\sigma$  observational constraints. The amount of overlap of the boxes is a rough measure of the consistency between theory and observations. We can also see the favored ranges of  $\eta$ . However, we will discuss the details of our analysis more carefully in the following section.

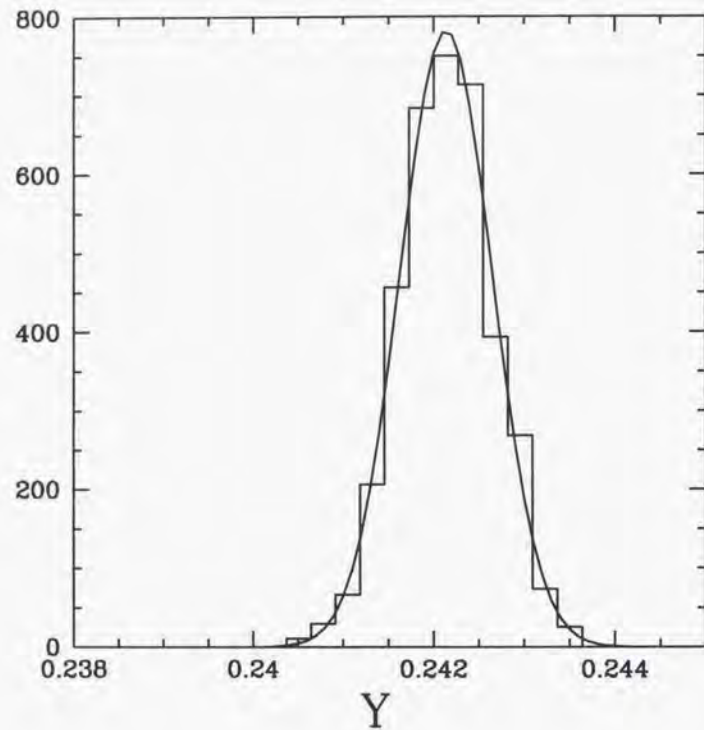


Figure 2.4: Histogram of the distribution of the theoretical value of  $Y$  computed by Monte Carlo simulation at  $\eta = 3.162 \times 10^{-10}$ . The solid curve denotes the gaussian distribution  $N(Y^{th}, \sigma_4^{th})$ . The unit of the vertical axis is arbitrary.

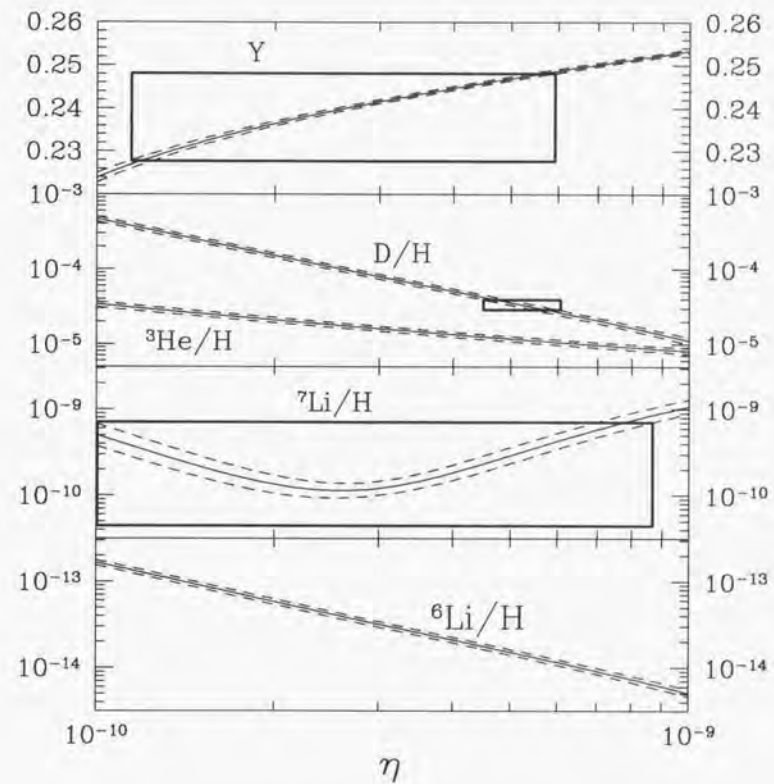


Figure 2.5: SBBN prediction of the abundances of the light elements. The solid lines are the central values of the predictions, and the dashed lines represents the  $1\text{-}\sigma$  uncertainties. The boxes denote the  $2\text{-}\sigma$  observational constraints.

## 2.4 Statistical Analysis and Results

Next, let us briefly explain how we quantify the consistency between theory and observation. For this purpose, we define the variable  $\chi^2$  as

$$\chi^2 = \sum_i \frac{(a_i^{th} - a_i^{obs})^2}{(\sigma_i^{th})^2 + (\sigma_i^{obs})^2} \quad (2.63)$$

where  $a_i = (y_2, Y, \log_{10} y_7)$ , and we add the systematic errors in quadrature:  $(\sigma_i^{obs})^2 = (\sigma_i^{stat})^2 + (\sigma_i^{sys})^2$ . (See the Appendix C for a detailed explanation of our use of  $\chi^2$  in SBBN.)  $\chi^2$  depends upon the parameters of our theory (viz.  $\eta$  in SBBN) through  $a_i^{th}$  and  $\sigma_i^{th}$ .

Notice that we do not include  ${}^6\text{Li}$  in the calculation of  $\chi^2$ , since the  ${}^6\text{Li}$  abundance has not been measured well. Instead, we check that  $y_6^{th}/y_7^{th}$  satisfies the bound (2.11). In the case of SBBN, we found that the  ${}^6\text{Li}$  abundance is small enough over the entire range of  $\eta$  from  $8.0 \times 10^{-11}$  to  $1.0 \times 10^{-9}$ . (Numerically,  $y_6^{th}/y_7^{th} < 5 \times 10^{-4}$ , which is well below the bound (2.11).)

With this  $\chi^2$  variable, we discuss how well the theoretical prediction agrees with observation. More precisely, we calculate from  $\chi^2$  the confidence level (C.L.) with which the SBBN theory is excluded, at a given point in the parameter space of our theory (for three degrees of freedom):

$$\text{C.L.} = \int_0^{\chi^2} \frac{1}{2^{3/2} \Gamma(\frac{3}{2})} y^{1/2} e^{-\frac{y}{2}} dy \quad (2.64)$$

$$= -\sqrt{\frac{2\chi^2}{\pi}} \exp\left(-\frac{\chi^2}{2}\right) + \text{erf}\left(\sqrt{\frac{\chi^2}{2}}\right), \quad (2.65)$$

In Fig. 2.6, we have plotted the  $\chi^2$  and confidence level at which SBBN theory is excluded by the observations, as a function of  $\eta$ . We find that SBBN is allowed at 68% C.L. at  $\eta \sim 5 \times 10^{-10}$  and allowed at 95% C.L. at  $\eta \sim (4.4 - 5.8) \times 10^{-10}$ . The above results mean that the predictions of SBBN agree with the observations excellently and the theory is reliable enough to test the history of the early universe around the BBN epoch.

Before closing this section, we apply our analysis to constrain the number of neutrino species. Here, we vary  $\eta$  and the number  $N_\nu$  of neutrino species, and we calculate the confidence level as a function of these variables. The results are shown in Fig. 2.7. We can see that the standard scenario ( $N_\nu = 3$ ) results in a good fit. In Table 2.3 we show the 68% C.L. and 95% C.L. bounds for the number of neutrino species  $N_\nu$  and  $\eta$ .

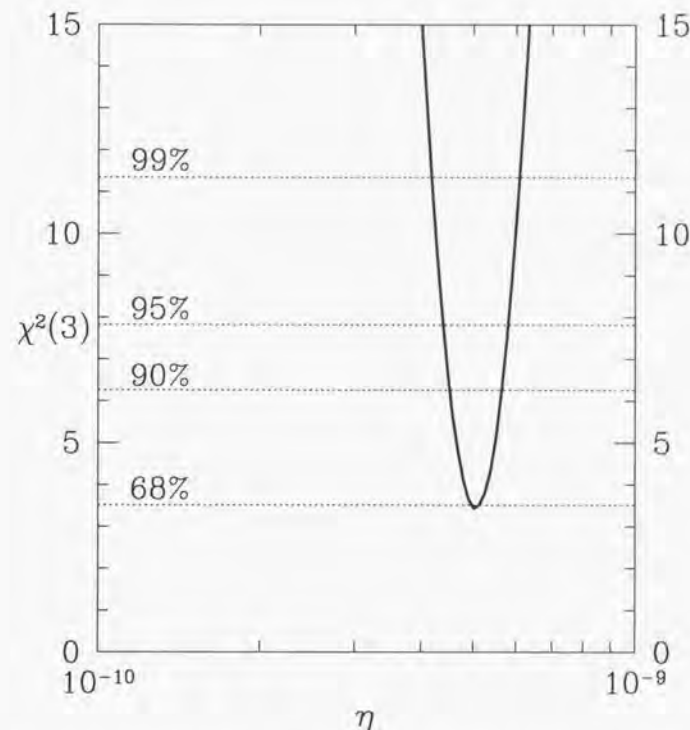


Figure 2.6:  $\chi^2$  as a function of  $\eta$ . The degree of freedom is three (D,  ${}^4\text{He}$ , and  ${}^7\text{Li}$ ).

	$N_\nu$	$\eta \times 10^{10}$
68 % C.L.	$2.3^{+0.7}_{-0.5}$	$4.7^{+0.8}_{-0.4}$
95 % C.L.	$2.3^{+1.1}_{-0.8}$	$4.7^{+1.2}_{-0.7}$

Table 2.3: Observational constraints on  $\eta$  and  $N_\nu$  in SBBN

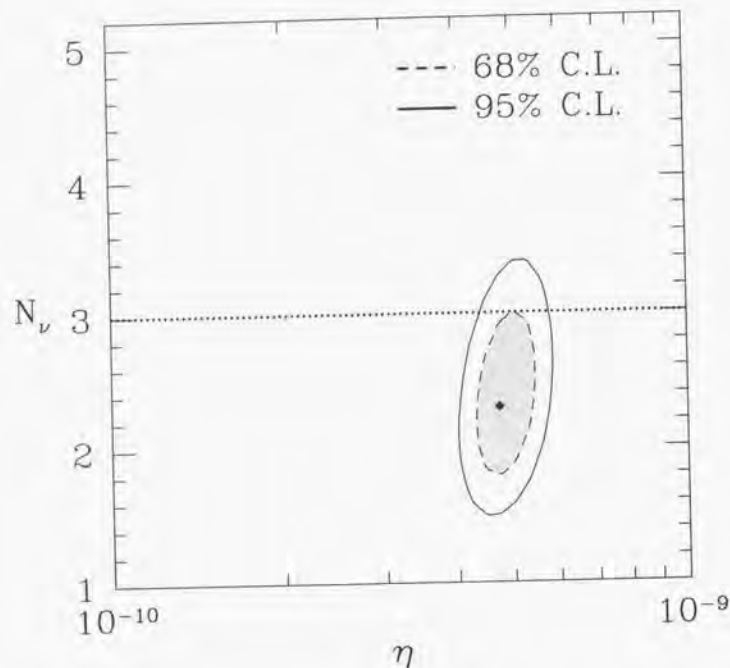


Figure 2.7: C.L. for BBN as a function of  $\eta$  and  $N_\nu$ . The filled diamond denotes the best-fit point.

## Chapter 3

### Late-time entropy production with hadron injection and Big Bang Nucleosynthesis

#### 3.1 Late-time entropy production : overview

In the standard big bang cosmology it had been assumed tacitly that the universe was dominated by the thermal radiation at the early epoch. Even in the paradigm of the modern cosmology it is commonly believed that thermal radiation was produced by the reheating process after the primordial inflation and they dominated the energy of the universe at the sufficiently early epoch. Here we ask, “How early should the universe be dominated by the radiation in order to success the standard big bang cosmology?”. We could say that the energy of the universe should be dominated by the radiation at least before the beginning of the big bang nucleosynthesis (BBN) epoch. In this chapter we answer the above question.

The various models of the modern particle physics beyond the standard model predict a number of unstable massive particles which have long lifetimes and decay at about the BBN epoch. The energy density of the non-relativistic particles or the oscillation energy density of the scalar fields (inflaton and so on) decreases as  $\rho_{NR}(t) \propto a(t)^{-3}$ , where  $a(t)$  is a scale factor. On the other hand since the radiation energy density decreases more rapidly  $\rho(t) \propto a(t)^{-4}$ , if the energy density of the massive non-relativistic particles or the oscillating scalar fields is large, it immediately dominates the universe as it expands, and the universe necessarily becomes the matter-dominated epoch until the cosmic time reaches to their lifetime. When the particles decay into standard particles (e.g. photon and electron), they produce the large entropy and the universe becomes radiation-dominated again. It is expected that such process would change the initial condition for the standard big bang scenario. We call the process “late-time entropy production”.

Now we have some interesting candidates for the late-time entropy production in models based on supersymmetry (SUSY). It is known that gravitino and Polonyi field which exist in local SUSY (i.e. supergravity) theories have masses of  $\sim \mathcal{O}(100\text{GeV} - 10\text{TeV})$  [38]. In

addition they have long lifetimes because they interact with the other particle only through the gravity. For example, since Polonyi field [39] which has a heavy mass  $\sim 10$  TeV cannot be diluted by the usual inflation, it immediately dominates the universe and decays at the BBN epoch. Moreover it is also known that in the superstring theories there exist a lot of light fields called dilaton and moduli which have the similar properties to the Polonyi field.

Recently Lyth and Stewart [40] considered a mini-inflation called "thermal inflation" which dilutes the above dangerous scalar fields. In the thermal inflation scenario, however, the flaton field which is responsible for the thermal inflation decays at late times. In particular, if the mass of Polonyi (moduli) is less than  $\sim 1$  GeV which is predicted in the framework of gauge-mediated SUSY breaking models [41], the sufficient dilution requires that the flaton decays just before BBN [42]. Thus in thermal inflation models one should take care of the late-time entropy production.

To keep the success of BBN, any long-lived massive particles or the coherent oscillation of any scalar fields which dominate the universe at that time must finally decay into the standard particles before the beginning of BBN. Moreover the decay products would have to be quickly thermalized through scatterings, annihilations, pair creations and further decays and make the thermal bath of photon, electron and neutrinos. Concerning photons and electrons which interact through the electromagnetic interaction, the interaction rate is much more rapid than the Hubble expansion rate at that time. Therefore it is expected that the photon and electron which are produced in the decay and subsequent scattering processes are efficiently thermalized. The problem is that neutrinos can interact only through the weak interaction. In the standard big bang cosmology the neutrinos usually decouple from the electromagnetic thermal bath at about  $T \simeq 2 - 3$  MeV. Therefore it is approximately inferred that they can not be sufficiently thermalized at the temperature  $T \lesssim$  a few MeV. Namely the reheating temperature after the entropy production process should be high enough to thermalize the neutrinos. Though people had ever used the rough constraints on the reheating temperature between 1 MeV - 10 MeV, in the previous separate publication [43] we pointed out that the neutrino thermalization is the most crucial for the successful BBN. In this thesis, we describe the detail of the method to obtain the neutrino spectrum and the formulations to integrate a set of Boltzmann equations numerically, and we study the constraint on the reheating temperature using the obtained neutrino spectrum and the full BBN network calculations with the revised observational light element abundances.

The above constraint is almost model-independent and hence conservative because we only assume that the massive particle decay produces the entropy. However, a more stringent constraint can be obtained if we assume a decay mode into quarks or gluons. In this case some modifications are needed for the above description. When the high energy quark-antiquark pairs or gluons are emitted, they immediately fragment into a lot of hadrons (pions, kaons, protons, neutrons, etc.). It is expected that they significantly influence the freeze-out value of neutron to proton ratio at the beginning of BBN through the strong interaction with the ambient protons and neutrons. In the previous work we did not consider such hadron

injection effects on BBN. Therefore we carefully treat the hadron injection effects in this thesis.

For another constraint, the late-time entropy production may induce the significant effects on the anisotropies of the cosmic microwave background radiation (CMB). Lopez *et al.* [44] pointed out that the CMB anisotropies are very sensitive to the equal time of matter and radiation though they investigated the effects in the other context. When the reheating temperature is so low that neutrinos do not be sufficiently thermalized, the radiation density which consists of photon and neutrinos becomes less than that in the standard big bang scenario. It may give distinguishable signals in the CMB anisotropies as a modification of the effective number of neutrino species  $N_\nu^{\text{eff}}$ . With the present angular resolutions and sensitivities of COBE observation [45] it is impossible to set a constraint on  $N_\nu^{\text{eff}}$ . But it is expected that future satellite experiments such as MAP [46] and PLANCK [47] will give us a useful information about  $N_\nu^{\text{eff}}$ . In addition the above effect may also induce the signals in the observed power spectrum of the density fluctuation for the large scale structure as a modification of the epoch of the matter-radiation equality.

## 3.2 Formulation of Neutrino Thermalization

### 3.2.1 Reheating Temperature

In order to discuss the late-time entropy production process, we should formulate the equations which describe the physical process. Here the reheating temperature  $T_R$  is an appropriate parameter to characterize the late-time entropy production. We define the reheating temperature  $T_R$  by

$$\Gamma \equiv 3H(T_R), \quad (3.1)$$

where  $\Gamma$  is the decay rate ( $=\tau^{-1}$ ) and  $H(T_R)$  is the Hubble parameter at the decay epoch ( $t = \tau$ ). Since the actual decay is not instantaneous, the matter-dominated universe smoothly changes into radiation-dominated one. Thus it is rather difficult to clearly identify the reheating temperature by observing the evolution of the cosmic temperature. Instead we "define" the reheating temperature formally by Eq. (3.1)

The Hubble parameter is expressed by

$$H = \left( \frac{g_* \pi^2}{90} \right)^{1/2} \frac{T_R^2}{M_G}, \quad (3.2)$$

where  $g_*$  is the statistical degrees of freedom for the massless particles and  $M_G$  is the reduced Planck mass ( $= 2.4 \times 10^{18}$  GeV). Then the reheating temperature is given by

$$T_R = 0.554 \sqrt{\Gamma M_G}. \quad (3.3)$$

Here we have used  $g_* = 43/4$ . From Eq. (3.3), we can see that the reheating temperature

has the one to one correspondence with the lifetime of the parent massive particle.

Here we define the effective number of neutrino species  $N_\nu^{\text{eff}}$  as a parameter which characterizes the time evolution of the energy density of neutrinos. Here  $N_\nu^{\text{eff}}$  is defined by

$$N_\nu^{\text{eff}} \equiv \frac{\rho_{\nu_e} + \rho_{\nu_\mu} + \rho_{\nu_\tau}}{\rho_{\text{std}}}, \quad (3.4)$$

where  $\rho_{\text{std}}$  is the total neutrino energy density in the standard big bang model (*i.e.* no late-time entropy production and three neutrino species).

### 3.2.2 Basic Equations

When a massive particle  $\phi$  which is responsible for the late-time entropy production decays, all emitted particles except neutrinos are quickly thermalized and make a thermal bath with temperature  $\sim T_R$ . For a relatively low reheating temperature  $T_R \lesssim 10\text{MeV}$  neutrinos are slowly thermalized. Since in realistic situations the decay branching ratio into neutrinos is very small, we assume that neutrinos are produced only through annihilations of electrons and positrons, *i.e.*  $e^+ + e^- \rightarrow \nu_i + \bar{\nu}_i$  ( $i = e, \mu, \tau$ ). The evolution of the distribution function  $f_i$  of the neutrino  $\nu_i$  is described by the momentum dependent Boltzmann equation [48]:

$$\frac{\partial f_i(\mathbf{p}, t)}{\partial t} - H(t)\mathbf{p} \frac{\partial f_i(\mathbf{p}, t)}{\partial \mathbf{p}} = C_{i,\text{coll}}, \quad (3.5)$$

where the right hand side is the total collision term.

The integrated Boltzmann equation [49] is not adequate in the present problem. As we show in Sec. 3.3, the spectral shape of the momentum distribution obtained by our scheme is much different from the equilibrium one. It should be noticed that the integrated Boltzmann equation assumes that the shape of the momentum distribution is the same as the equilibrium one. Thus we should solve the momentum dependent Boltzmann equation.

When the reaction is two bodies scattering  $1 + 2 \rightarrow 3 + 4$ , it is given by the expression,

$$C_{i,\text{coll}} = \frac{1}{2E_1} \sum \int \frac{d^3 p_2}{2E_2(2\pi)^3} \frac{d^3 p_3}{2E_3(2\pi)^3} \frac{d^3 p_4}{2E_4(2\pi)^3} \times (2\pi)^4 \delta^{(4)}(p_1 + p_2 - p_3 - p_4) \Lambda(f_1, f_2, f_3, f_4) S |M|_{i2 \rightarrow 34}^2, \quad (3.6)$$

where  $|M|^2$  is the scattering amplitude summed over spins of all particles,  $S$  is the symmetrization factor which is  $1/2$  for identical particles in initial and final states,  $\Lambda = f_3 f_4 (1 - f_1)(1 - f_2) - f_1 f_2 (1 - f_3)(1 - f_4)$  is the phase space factor including Pauli blocking of the final states. Then the total collision term  $C_{i,\text{coll}}$  is expressed by,

$$C_{i,\text{coll}} = C_{i,\text{ann}} + C_{i,\text{scat}}, \quad (3.7)$$

where  $C_{i,\text{ann}}$  is the collision term for annihilation processes and  $C_{i,\text{scat}}$  is the collision term

for elastic scattering processes. Here we consider the following processes:

$$\begin{aligned} \nu_i + \nu_i &\leftrightarrow e^+ + e^-, \\ \nu_i + e^\pm &\leftrightarrow \nu_i + e^\pm. \end{aligned}$$

In this chapter we have treated neutrinos as Majorana ones (*i.e.*,  $\nu = \bar{\nu}$ ). It should be noted that there are no differences between Majorana neutrinos and Dirac ones as long as they are massless, and since the temperature is  $\mathcal{O}(\text{MeV})$  at least in this situation, we could have treated them as if they were massless particles. The relevant reactions are presented in Table 3.1 for  $\nu_e$  and Table 3.2 for  $\nu_\mu$  and  $\nu_\tau$ .

Here we neglect the neutrino self-interactions. It may lead to underestimate the kinetic equilibrium rate for high reheating temperatures. However, we think that this effect does not change the results very much. The interactions between electrons and neutrinos are the most important because they transfer the energy of the thermal bath to neutrinos. The self-interactions of the neutrinos cannot increase the energy density of neutrinos but mainly change their momentum distribution. Furthermore, the neutrino number densities are much smaller than the electron number density at low reheating temperature with which we are concerned. Thus differences caused by the neutrino self interactions are expected to be small.

Process	$S M ^2$
$\nu_e + e^- \rightarrow \nu_e + e^-$	$32G_F^2 [(C_V + C_A)^2 (p_1 \cdot p_2)^2 + (C_V - C_A)^2 (p_1 \cdot p_4)^2]$
$\nu_e + e^+ \rightarrow \nu_e + e^+$	$32G_F^2 [(C_V - C_A)^2 (p_1 \cdot p_2)^2 + (C_V + C_A)^2 (p_1 \cdot p_4)^2]$
$\nu_e + \bar{\nu}_e \rightarrow e^+ + e^-$	$32G_F^2 [(C_V + C_A)^2 (p_1 \cdot p_4)^2 + (C_V - C_A)^2 (p_1 \cdot p_3)^2]$

Table 3.1: Matrix elements for electron neutrino interactions.  $G_F$  is the Fermi coupling constant. Here we take  $C_V = \frac{1}{2} + 2\sin^2\theta_W$ ,  $C_A = \frac{1}{2}$  and the weak mixing angle  $\sin^2\theta_W \simeq 0.231$ .

Process	$S M ^2$
$\nu_\mu + e^- \rightarrow \nu_\mu + e^-$	$32G_F^2 [(\tilde{C}_V + \tilde{C}_A)^2 (p_1 \cdot p_2)^2 + (\tilde{C}_V - \tilde{C}_A)^2 (p_1 \cdot p_4)^2]$
$\nu_\mu + e^+ \rightarrow \nu_\mu + e^+$	$32G_F^2 [(\tilde{C}_V - \tilde{C}_A)^2 (p_1 \cdot p_2)^2 + (\tilde{C}_V + \tilde{C}_A)^2 (p_1 \cdot p_4)^2]$
$\nu_\mu + \bar{\nu}_\mu \rightarrow e^+ + e^-$	$32G_F^2 [(\tilde{C}_V + \tilde{C}_A)^2 (p_1 \cdot p_4)^2 + (\tilde{C}_V - \tilde{C}_A)^2 (p_1 \cdot p_3)^2]$

Table 3.2: Matrix elements for muon neutrino or tau neutrino interactions.  $G_F$  is the Fermi coupling constant. Here we take  $\tilde{C}_V = C_V - 1 = -\frac{1}{2} + 2\sin^2\theta_W$ ,  $\tilde{C}_A = C_A - 1 = -\frac{1}{2}$  and the weak mixing angle  $\sin^2\theta_W \simeq 0.231$ .

The collision terms are quite complicated and expressed by nine dimensional integrations over momentum space. However, if we neglect electron mass and assume that electrons

obey the Boltzmann distribution  $e^{-p/T}$ , the collision terms are simplified to one dimensional integration form.<sup>1</sup>

Then  $C_{i,ann}$  is given by [52, 53]

$$C_{i,ann} = -\frac{1}{2\pi^2} \int p_i'^2 dp_i' (\sigma v)_i (f_i(p_i) f_i(p_i') - f_{eq}(p_i) f_{eq}(p_i')), \quad (3.8)$$

where  $f_{eq}(= 1/(e^{p_i/T} + 1))$  is the equilibrium distribution and  $(\sigma v)_i$  is the differential cross sections given by

$$(\sigma v)_e = \frac{4G_F^2}{9\pi} (C_V^2 + C_A^2) pp', \quad (3.9)$$

$$(\sigma v)_{\mu,\tau} = \frac{4G_F^2}{9\pi} (\tilde{C}_V^2 + \tilde{C}_A^2) pp', \quad (3.10)$$

$$(3.11)$$

where we take  $C_V = \frac{1}{2} + 2 \sin^2 \theta_W$ ,  $C_A = \frac{1}{2}$ ,  $\tilde{C}_V = C_V - 1$  ( $\tilde{C}_A = C_A - 1$ ) and  $\theta_W$  is Weinberg angle ( $\sin^2 \theta_W \simeq 0.231$ ) [32].

As for elastic scattering processes,  $C_{i,scat}$  is also simplified to one dimensional integration (see Appendix), and it is expressed as

$$C_{i,scat} = \frac{G_F^2}{2\pi^3} (C_V^2 + C_A^2) \left[ -\frac{f_i}{p_i'} \left( \int_0^{p_i'} dp_i' F_1(p_i, p_i') (1 - f_i(p_i')) + \int_{p_i'}^\infty dp_i' F_2(p_i, p_i') (1 - f_i(p_i')) \right) + \frac{1 - f_i(p_i)}{p_i^2} \left( \int_0^{p_i} dp_i' B_1(p_i, p_i') f_i(p_i') + \int_{p_i}^\infty dp_i' B_2(p_i, p_i') f_i(p_i') \right) \right], \quad (3.12)$$

where  $(C_V^2 + C_A^2)$  should be replaced by  $(\tilde{C}_V^2 + \tilde{C}_A^2)$  for  $i = \mu, \tau$ , and the functions  $F_1, F_2, B_1, B_2$  are given by

$$\begin{aligned} F_1(p, p') &= D(p, p') + E(p, p') e^{-p'/T}, \\ F_2(p, p') &= D(p', p) e^{(p-p')/T} + E(p, p') e^{-p'/T}, \\ B_1(p, p') &= F_2(p', p), \quad B_2(p, p') = F_1(p', p), \end{aligned} \quad (3.13)$$

where

$$D(p, p') = 2T^3(p^2 + p'^2 + 2T(p - p') + 4T^2).$$

<sup>1</sup>The errors due to neglecting the electron mass is small and the deviation is just a few percent. We show the reasons as follows. The difference between Fermi-Dirac and Maxwell-Boltzmann distribution " $df$ " is less than one at most  $df < 1.0$ . The weak interaction rate is almost expressed by  $(\sigma v)n_e/H(t)$ , where  $(\sigma v) \sim G_F^2 m_e^2$  and  $n_e$  is an electron number density. Then the error is at most estimated by,  $(\sigma v)n_e/H(t) \times df \lesssim 10^{-2}$  (for  $T \lesssim 0.5 \text{ MeV}$ ). Therefore the deviation is a few percent and the neglecting the electron mass does not change the results. The other methods of the approximation to reduce the integral from nine to two dimensions in which the electron mass is not neglected are presented in ref. [50, 51]

$$E(p, p') = -T^2 [p^2 p'^2 + 2pp'(p + p')T + 2(p + p')^2 T^2 + 4(p + p')T^3 + 8T^4]. \quad (3.14)$$

Together with the above Boltzmann equations, we should solve the energy-momentum conservation equation in the expanding universe:

$$\frac{d\rho(t)}{dt} = -3H(t)(\rho(t) + P(t)), \quad (3.15)$$

where  $\rho(t) = \rho_\phi + \rho_\gamma + \rho_e + \rho_\nu$  is the total energy density of  $\phi$ , photon, electron and neutrinos and it is given by

$$\rho(t) = \rho_\phi(t) + \frac{\pi^2 T_\gamma^4}{15} + \frac{2}{\pi^2} \int \frac{dq q^2 E_e}{\exp(E_e/T_\gamma) + 1} + \frac{1}{\pi^2} \int dq q^3 f_{\nu_e}(q) + \frac{2}{\pi^2} \int dq q^3 f_{\nu_\mu}(q), \quad (3.16)$$

where  $E_e = \sqrt{q^2 + m_e^2}$  is the electron energy.  $P(t) \equiv P_\gamma(t) + P_{e^\pm}(t) + P_\nu(t)$  is the total pressure,

$$P(t) = \frac{\pi^2 T_\gamma^4}{45} + \frac{2}{\pi^2} \int \frac{dq q^4}{3E_e [\exp(E_e/T_\gamma) + 1]} + \frac{1}{3\pi^2} \int dq q^3 f_{\nu_e}(q) + \frac{2}{3\pi^2} \int dq q^3 f_{\nu_\mu}(q), \quad (3.17)$$

$H(t)$  is the Hubble parameter,

$$H(t) = \frac{\dot{a}(t)}{a(t)} = \frac{1}{\sqrt{3}M_G} \sqrt{\rho(t)}. \quad (3.18)$$

The time evolution equation of  $\rho_\phi$  is given by

$$\frac{d\rho_\phi}{dt} = -\Gamma\rho_\phi - 3H\rho_\phi. \quad (3.19)$$

Practically we solve the time evolution of the photon temperature instead of Eq. (3.15),

$$\frac{dT_\gamma}{dt} = -\frac{-\rho_\phi/\tau_\phi + 4H\rho_\gamma + 3H(\rho_{e^\pm} + P_{e^\pm}) + 4H\rho_\nu + d\rho_\nu/dt}{\partial\rho_\gamma/\partial T_\gamma|_{a(t)} + \partial\rho_{e^\pm}/\partial T_\gamma|_{a(t)}}. \quad (3.20)$$

together with Eqs. (3.5), (3.18) and (3.19).

### 3.3 Neutrino Thermalization and BBN

#### 3.3.1 Time evolution of Neutrino spectrum

The evolution of the cosmic temperature  $T$  is shown in Fig. 3.1 (a) for  $T_R = 10 \text{ MeV}$ , and (b) for  $T_R = 2 \text{ MeV}$ . In Fig. 3.1 (a), it is seen that the temperature decreases slowly as  $t^{-1/4}$ , i.e.  $a^{-3/8}$  before the decay epoch,  $t \simeq \Gamma^{-1} (\simeq 5 \times 10^{-2} \text{ sec})$  which corresponds to  $T_R = 10 \text{ MeV}$ . This is because the actual decay is not instantaneous and  $\phi$  decays into the

radiation continuously at the rate  $\Gamma$  [54]. Then the universe is still in M.D. After the decay epoch  $t \gg \Gamma^{-1}$ , all  $\phi$ -particles decay and the temperature decreases as  $\propto a^{-1}$  ( $t^{-1/2}$ ). Then the universe becomes radiation-dominated epoch. Since at the temperature  $T \lesssim 0.5 \text{ MeV}$  ( $t \gtrsim 3 \text{ sec}$ ), electrons and positrons annihilate into photons  $e^+e^- \rightarrow 2\gamma$ , the temperature is slightly heated. From Fig. 3.1 (b) we can see that the temperature decreases as  $t^{-1/4}$  until the decay epoch ( $t \lesssim 0.1 \text{ sec}$ ) which corresponds to  $T_R = 2 \text{ MeV}$ . After the decay epoch, the temperature decreases as  $t^{-1/2}$  (R.D.). In the actual computation we take a initial condition that there exists the net radiation energy density though the universe is in M.D. This represents the situation that the massive particle necessarily dominated the universe as it expands. On the other hand even if there are at first no radiation  $\rho_R \simeq 0$ , i.e.  $T \simeq 0$  which corresponds to the initial condition of the oscillation epoch after the primordial inflation or thermal inflation, the cosmic temperature immediately tracks the same curve  $t^{-1/4}$  and then their decay establishes the radiation dominated universe  $T \propto t^{-1/2}$ . Therefore our treatment is quite a general picture for each entropy production scenario and it does not depend on whether the net initial radiation energy exists or not, only if once unstable non-relativistic particles dominate the energy density of the universe.

In Fig. 3.2 we show the evolutions of  $\rho_{\nu_e}$  and  $\rho_{\nu_\mu}$  ( $=\rho_{\nu_\tau}$ ) (a) for  $T_R = 10 \text{ MeV}$  and (b) 2 MeV. From Fig. 3.2(a) we can see that if  $T_R = 10 \text{ MeV}$ , cosmic energy density is as same as the case of standard big bang cosmology. As shown in Fig. 3.2(b), however, the energy density of each neutrino species for  $T_R = 2 \text{ MeV}$  is smaller than the case of standard scenario. Since the electron neutrinos interact with electrons and positrons through both charged and neutral currents, they are more effectively produced from the thermal bath than the other neutrinos which have only neutral current interactions. The final distribution functions  $f_e$  and  $f_\mu$  ( $=f_\tau$ ) are shown in Fig. 3.3 (a) for  $T_R = 10 \text{ MeV}$  and (b) 2 MeV. For  $T_R = 10 \text{ MeV}$ , each neutrino is thermalized well and the perfect Fermi-Dirac distribution is established. For  $T_R = 2 \text{ MeV}$ , however, the distributions are not thermal equilibrium

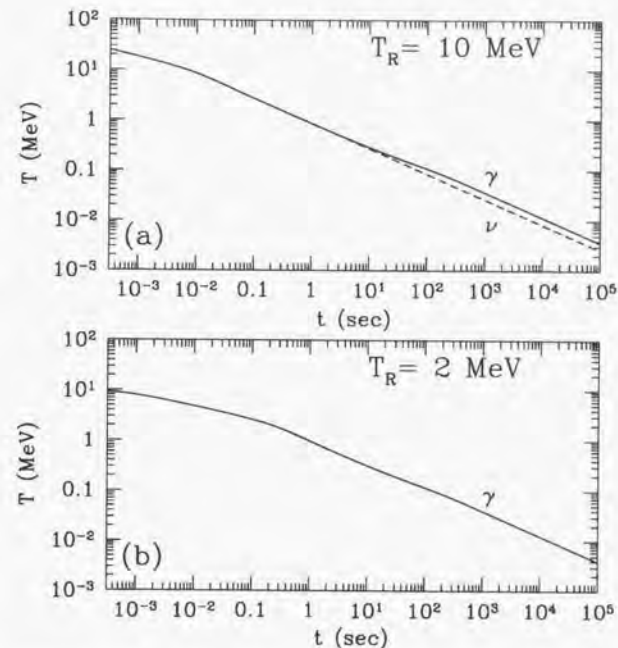


Figure 3.1: Time evolution of the cosmic temperature (a) for  $T_R = 10 \text{ MeV}$ , and (b) for  $T_R = 2 \text{ MeV}$ . The dashed line denotes the neutrino temperature which can be defined only when they are thermalized sufficiently and have the perfect Fermi-Dirac distribution.

forms.<sup>2</sup>

<sup>2</sup>As we noted in Sec. 3.2, we must not use the integrated Boltzmann equation instead of the momentum dependent Boltzmann equation in the present problem because the former assumes the equilibrium distribution. To see this, let us define the ratio  $R_E$  for a neutrino species by  $R_E = (\rho_\nu/n_\nu)/(3.151\tilde{T}_\nu)$ , where  $\rho_\nu$  is the neutrino energy density,  $n_\nu$  is the neutrino number density,  $\tilde{T}_\nu$  is the effective neutrino temperature which is defined by the neutrino number density as,  $\tilde{T}_\nu \equiv (2\pi^2/(3\zeta(3))n_\nu)^{1/3}$ . Here both  $\rho_\nu$  and  $n_\nu$  are computed by integrating the neutrino distribution function which is obtained by solving the momentum dependent Boltzmann equation. Approximately  $R_E$  represents a ratio of the mean energy per a neutrino to the thermal equilibrium one. If the neutrino is in thermal equilibrium,  $R_E$  is unity. In the case of the integrated Boltzmann equation, because it is assumed that the shape of the neutrino distribution is the same as the equilibrium one at any times,  $R_E$  is necessarily unity. On the other hand, in the case of our scheme, i.e. the momentum dependent Boltzmann equation,  $R_E$  might not be unity. We have computed the ratio  $R_E$  in some representative reheating temperatures for electron neutrino and have found that they deviated from unity more at the lower reheating temperatures,  $R_E = 1.00, 1.03$  and  $1.50$  (for  $T_R = 10 \text{ MeV}, 3 \text{ MeV}$  and  $1 \text{ MeV}$ ). Moreover at the lower reheating temperature than  $1 \text{ MeV}$ , the deviation is much larger. This

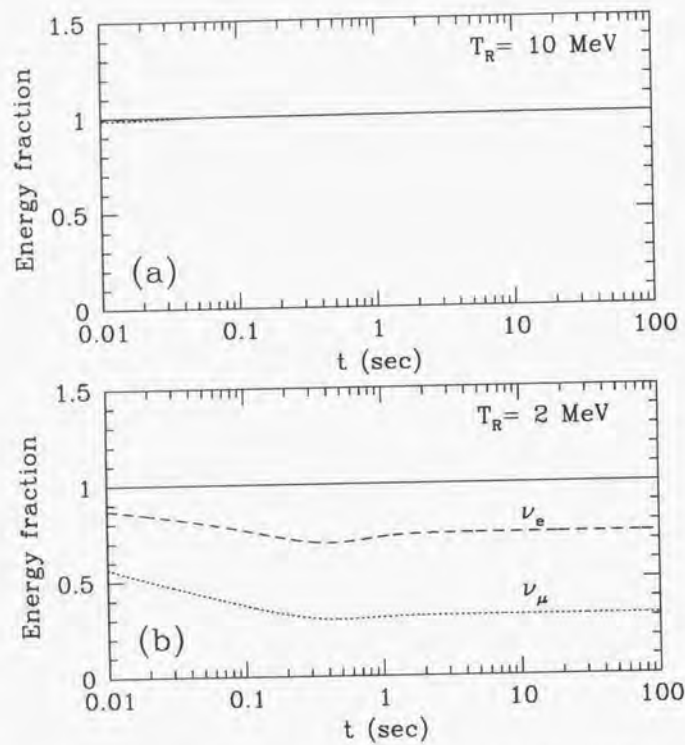


Figure 3.2: Time evolution of the fraction of the energy density of  $\nu_e$  (dashed curve) and  $\nu_\mu$  (dotted curve) to that of the standard big bang scenario for (a)  $T_R = 10$  MeV and (b)  $T_R = 2$  MeV. Since the interaction of  $\nu_\tau$  is as same as  $\nu_\mu$ , the curve of  $\nu_\mu$  also represents  $\nu_\tau$ .

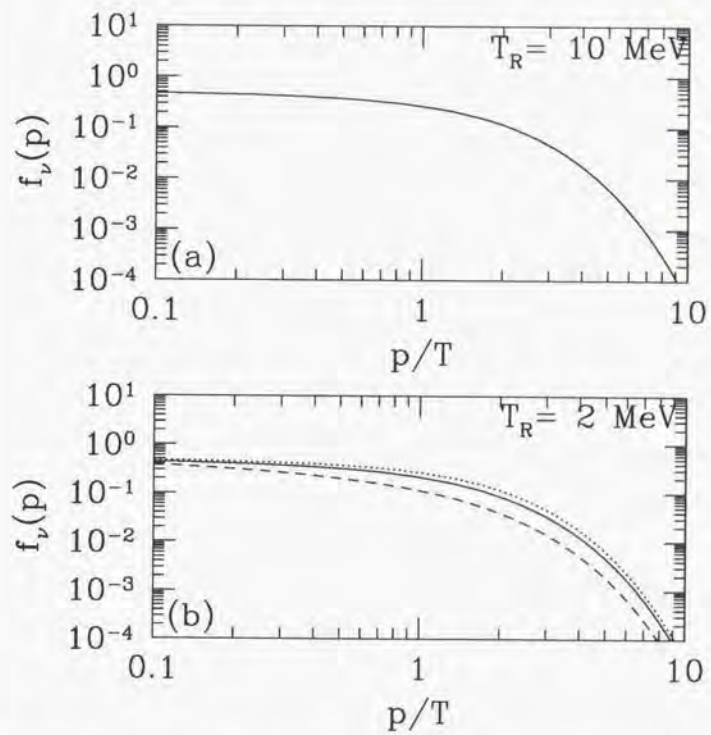


Figure 3.3: Distribution function of  $\nu_e$  (solid curve) and  $\nu_\mu$  (dashed curve) (a) for  $T_R = 10$  MeV and (b) for  $T_R = 2$  MeV. The dotted curve is the Fermi-Dirac distribution function. Since the interaction of  $\nu_\tau$  is as same as  $\nu_\mu$ , the curve of  $\nu_\mu$  also represents  $\nu_\tau$ .

In Fig. 3.4 we can see the change of the effective number of neutrino species  $N_\nu^{\text{eff}}$  as a function of the reheating temperature  $T_R$ . If  $T_R \gtrsim 7$  MeV,  $N_\nu^{\text{eff}}$  is almost equal to three and neutrinos are thermalized very well. We can regard it as the initial condition which has ever been used for the standard big bang cosmology. On the other hand, if  $T_R \lesssim 7$  MeV,  $N_\nu^{\text{eff}}$  becomes smaller than three.

### 3.3.2 Neutrino thermalization and neutron to proton ratio

If the neutrinos are not thermalized sufficiently and do not have the perfect Fermi-Dirac distribution, *i.e.* in this case there is the deficit of the neutrino distribution due to the low reheating temperature, it considerably influences the produced light element abundances. In particular, the abundance of the primordial  $^4\text{He}$  is drastically changed. The change of the neutrino distribution function influences the neutrino energy density and the weak interaction rates between proton and neutron. At the beginning of BBN ( $T \sim 1$  MeV - 0.1 MeV) the competition between the Hubble expansion rate  $H$  and the weak interaction rates  $\Gamma_{n \leftrightarrow p}$  determines the freeze-out value of the neutron to proton ratio  $n/p$ . After the freeze-out time, neutrons can change into protons only through the free decay with the life time  $\tau_n$ . Since  $^4\text{He}$  is the most stable light element and the almost all neutrons are synthesized into  $^4\text{He}$ , the abundance of the primordial  $^4\text{He}$  is sensitive to the freeze-out value of neutron to proton ratio.

If the neutrino energy density gets smaller than that of the standard BBN (SBBN), the Hubble expansion rate which is proportional to the square of the total energy density is also decreased. Then the freeze out time becomes later and the  $\beta$  equilibrium between neutrons and protons continues for longer time. As a result less neutrons are left. In this case the predicted  $^4\text{He}$  is less than the prediction of SBBN. The effect due to the speed-down expansion is approximately estimated by

$$\Delta Y \simeq -0.1(-\Delta\rho_{\text{tot}}/\rho_{\text{tot}}), \quad (3.21)$$

where  $Y$  is the mass fraction of  $^4\text{He}$  and  $\rho_{\text{tot}}$  is the total energy density of the universe.

Moreover, when the electron neutrino is not thermalized, there is interesting effect by which more  $^4\text{He}$  are produced. The weak reaction rates are computed by integrating neutrino distribution functions which are obtained by solving Boltzmann equations numerically. Using the neutrino distribution functions, the six weak interaction rates between neutron and proton are represented by

$$\Gamma_{n \rightarrow p e^- \bar{\nu}_e} = K \int_0^{Q-m_e} dp_{\nu_e} \left[ \sqrt{(p_{\nu_e} - Q)^2 - m_e^2} (Q - p_{\nu_e}) \frac{F_{\nu_e}^2}{1 + e^{(p_{\nu_e} - Q)/T}} (1 - f_{\nu_e}(p_{\nu_e})) \right] \quad (3.22)$$

result tells us that the neutrino distribution deviates from the thermal equilibrium shape considerably at the low reheating temperatures and we should solve the momentum dependent Boltzmann equation.  $R_E$  has a tendency to increase as the reheating temperature decreases. This is because neutrinos are produced by the annihilation of electrons-positron pairs whose mean energy per one particle is larger than that of neutrinos.

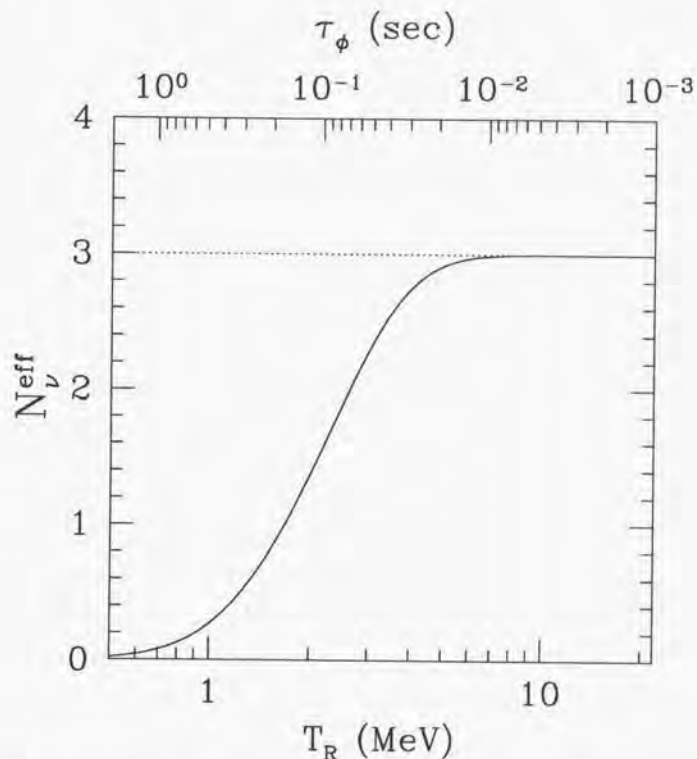


Figure 3.4: Effective number of neutrino species  $N_\nu^{\text{eff}}$  as a function of reheating temperature  $T_R$ . The top horizontal axis denotes the lifetime which corresponds to  $T_R$ .

$$\Gamma_{ne^+ \rightarrow p\bar{\nu}_e} = K \int_{Q+m_e}^{\infty} dp_{\nu_e} \left[ \sqrt{(p_{\nu_e} - Q)^2 - m_e^2} (p_{\nu_e} - Q) \frac{p_{\nu_e}^2}{e^{(p_{\nu_e} - Q)/T_\gamma} + 1} (1 - f_{\nu_e}(p_{\nu_e})) \right], \quad (3.23)$$

$$\Gamma_{\nu_e \rightarrow pe^-} = K \int_0^{\infty} dp_{\nu_e} \left[ \sqrt{(p_{\nu_e} + Q)^2 - m_e^2} (p_{\nu_e} + Q) \frac{p_{\nu_e}^2}{1 + e^{-(p_{\nu_e} + Q)/T_\gamma}} f_{\nu_e}(p_{\nu_e}) \right], \quad (3.24)$$

$$\Gamma_{pe^- \rightarrow n\nu_e} = K \int_0^{Q-m_e} dp_{\nu_e} \left[ \sqrt{(p_{\nu_e} - Q)^2 - m_e^2} (Q - p_{\nu_e}) \frac{p_{\nu_e}^2}{e^{-(p_{\nu_e} - Q)/T_\gamma} + 1} f_{\nu_e}(p_{\nu_e}) \right], \quad (3.25)$$

$$\Gamma_{pe^- \rightarrow n\bar{\nu}_e} = K \int_0^{\infty} dp_{\nu_e} \left[ \sqrt{(p_{\nu_e} + Q)^2 - m_e^2} (Q + p_{\nu_e}) \frac{p_{\nu_e}^2}{e^{(p_{\nu_e} + Q)/T_\gamma} + 1} (1 - f_{\nu_e}(p_{\nu_e})) \right], \quad (3.26)$$

$$\Gamma_{p\bar{\nu}_e \rightarrow ne^+} = K \int_{Q+m_e}^{\infty} dp_{\nu_e} \left[ \sqrt{(p_{\nu_e} - Q)^2 - m_e^2} (Q - p_{\nu_e}) \frac{p_{\nu_e}^2}{1 + e^{-(p_{\nu_e} - Q)/T_\gamma}} f_{\nu_e}(p_{\nu_e}) \right], \quad (3.27)$$

where  $Q = m_n - m_p = 1.29$  MeV and  $K$  is a normalization factor which is determined by the neutron life time  $\tau_n$  as  $K \simeq (1.636\tau_n)^{-1}$  and  $\tau_n$  is obtained by the experiments [32]. From the above equations we can see that if neutrino and anti-neutrino distribution functions are decreased, both  $\beta$  decay rates  $\Gamma_{n \rightarrow p} = \Gamma_{n \rightarrow pe^- \bar{\nu}_e} + \Gamma_{ne^+ \rightarrow p\bar{\nu}_e} + \Gamma_{\nu_e \rightarrow pe^-}$  and  $\Gamma_{p \rightarrow n} = \Gamma_{pe^- \bar{\nu}_e \rightarrow n} + \Gamma_{pe^- \rightarrow n\nu_e} + \Gamma_{p\bar{\nu}_e \rightarrow ne^+}$  are simultaneously decreased by the following reasons. The dominant effects by the deficit of the distribution functions are to decrease the rates  $\Gamma_{\nu_e \rightarrow pe^-}$ ,  $\Gamma_{pe^- \bar{\nu}_e \rightarrow n}$  and  $\Gamma_{p\bar{\nu}_e \rightarrow ne^+}$  which have the neutrino or anti-neutrino in the initial state. On the other hand, though the other rates  $\Gamma_{n \rightarrow pe^- \bar{\nu}_e}$ ,  $\Gamma_{ne^+ \rightarrow p\bar{\nu}_e}$  and  $\Gamma_{pe^- \rightarrow n\nu_e}$  which have the neutrino or anti-neutrino in the final state are slightly increased due to Fermi-blocking factor  $(1 - f_\nu)$ , the ratio of the difference  $\Delta f_\nu$  to  $(1 - f_\nu)$  is much smaller than that of  $\Delta f_\nu$  to  $f_\nu$ , *i.e.*

$$|\Delta f_\nu / (1 - f_\nu)| \ll |\Delta f_\nu / f_\nu| \quad \text{for } f_\nu \ll 1. \quad (3.28)$$

Therefore, the enhancement is small and the latter effect is not important. In total, both weak interaction rates  $\Gamma_{n \rightarrow p}$  and  $\Gamma_{p \rightarrow n}$  are decreased and become smaller than those of SBBN. In Fig. 3.5 the weak interaction rates  $\Gamma_{n \rightarrow p}$  and  $\Gamma_{p \rightarrow n}$  are plotted. The solid lines denote the case of  $T_R = 10$  MeV which correspond to the standard big bang scenario. The dotted lines denote the case of  $T_R = 1$  MeV. In the plot we can see that the insufficient thermalization of the neutrino distributions derives the changes of the weak interaction rates.

The decrease of weak interaction rates gives significant effects on the abundance of  $^4\text{He}$ . When the weak interaction rate  $\Gamma_{n \rightarrow p}$  decreases, the Hubble expansion rate becomes more rapid than that of the weak interaction rate earlier. Namely the freeze-out time becomes earlier. Then the freeze-out value of neutron to proton ratio becomes larger than in SBBN and it is expected that the predicted  $^4\text{He}$  abundance becomes larger. The above effect is approximately estimated by

$$\Delta Y \simeq +0.19(-\Delta\Gamma_{n \rightarrow p}/\Gamma_{n \rightarrow p}) \quad (3.29)$$

In Fig. 3.6 we plot the time evolution of the neutron to proton ratio. In Fig. 3.6(a) we change only the number of neutrino species in SBBN. The dotted line denotes the curve

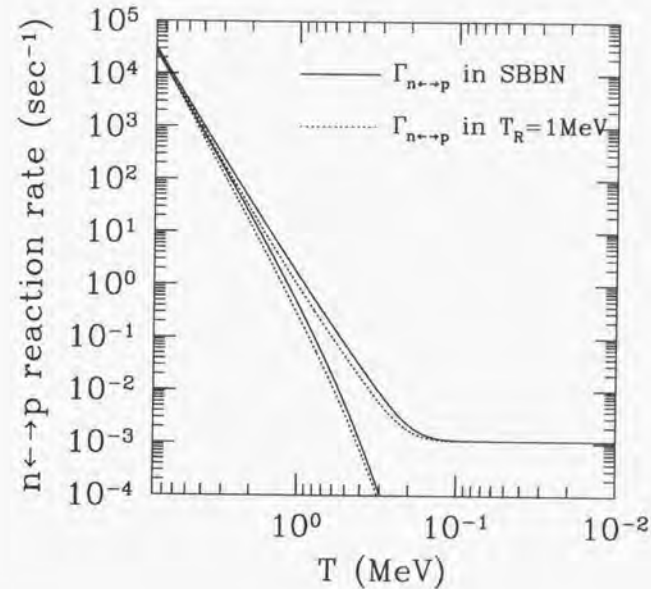


Figure 3.5: Weak interaction rates ( $\text{sec}^{-1}$ ) between neutron and proton. The upper curves are  $\Gamma_{n \rightarrow p}$ . The lower curves are  $\Gamma_{p \rightarrow n}$ . The solid lines denote the case of  $T_R = 10$  MeV which corresponds to the standard big bang scenario. The dotted lines denote the case of  $T_R = 1$  MeV in the late-time entropy production scenario. Notice that  $\Gamma_{n \rightarrow p}^{-1}$  reaches  $\tau_n = 887$  sec in the low temperature.

of  $N_\nu^{\text{eff}} = 1.37$  which corresponds to the effective number of neutrino species in the case of  $T_R = 2$  MeV in the late-time entropy production scenario. Then we find that the predicted  $n/p$  curve is lower than that of  $N_\nu^{\text{eff}} = 3$  due to only the speed down effect or the later decoupling. In Fig. 3.6(b) we plot the time evolution of  $n/p$  when we change the reheating temperature in the late-time entropy production scenario. The dotted line denotes the case of  $T_R = 2$  MeV. Comparing to the case of  $N_\nu^{\text{eff}} = 1.37$  in Fig. 3.6(a), the  $n/p$  ratio becomes larger. It is because the weak interaction rates are decreased by the deficit of the distribution function. Moreover in the case of  $T_R = 1$  MeV the  $n/p$  ratio becomes larger than the case of  $T_R = 10$  MeV.

### 3.3.3 Neutrino thermalization and light element abundances

Next we perform Monte Carlo simulation and the maximum likelihood analysis [55] to discuss how the theoretical predictions with the low reheating temperature scenario agree with the observational light element abundances.

In Fig. 3.7 we plotted  $^4\text{He}$  mass fraction  $Y$  as a function of  $T_R$  at  $\eta = 5 \times 10^{-10}$  (solid line). The dashed line denotes the virtual  $^4\text{He}$  mass fraction computed by including only the speed down effect due to the change of the effective number of neutrino species which is shown in Fig. 3.4. The dotted line denotes the predicted value of  $Y$  in SBBN at  $\eta = 5 \times 10^{-10}$ . For  $T_R \gtrsim 7$  MeV, the solid line and dashed line are quite equal to the value in SBBN. As  $T_R$  decreases, both the solid and dashed lines gradually decrease because of the speed down effect due to the change of  $N_\nu^{\text{eff}}$ . The dashed line continues to decrease as the reheating temperature decreases.

On the other hand, for  $T_R \lesssim 2$  MeV the effect that the weak interaction rates are weakened due to the deficit of the neutrino distribution function begins to become important and the predicted value of  $Y$  begins to increase as  $T_R$  decreases. For  $T_R \lesssim 1$  MeV, since it is too late to produce enough electrons whose mass is about  $m_e = 0.511$  MeV, the weak interaction rates are still more weakened and  $Y$  steeply increases as  $T_R$  decreases.

In Fig. 3.8 we plot the contours of the confidence levels in the  $\eta$ - $T_R$  plane. The solid line denotes 95 % C.L. and the dotted line denotes 68 % C.L. The filled square is the best fit point between the observation and theoretical predictions. The observational data are consistent with the high baryon to photon ratio,  $\eta \sim (3 - 6) \times 10^{-10}$ . From Fig. 3.8 we find that  $T_R \lesssim 0.7$  MeV is excluded at 95 % C.L. In other words  $T_R$  as low as 0.7 MeV is consistent with BBN. Then  $N_\nu^{\text{eff}}$  can be as small as 0.1 and it definitely influences the formation of the large scale structure and CMB anisotropy as is seen in Sec.3.5.

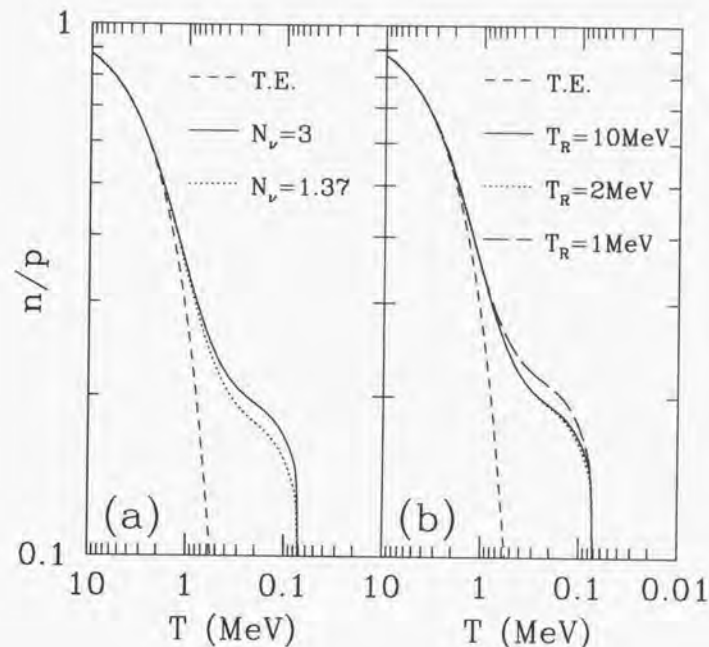


Figure 3.6: Evolution of neutron to proton ratio as a function of the temperature, (a) when we change only the number of neutrino species in the standard big bang scenario, and (b) when we change the reheating temperature in the late-time entropy production scenario. The dashed line is the thermal equilibrium curve ( $= e^{-Q/T}$ ).

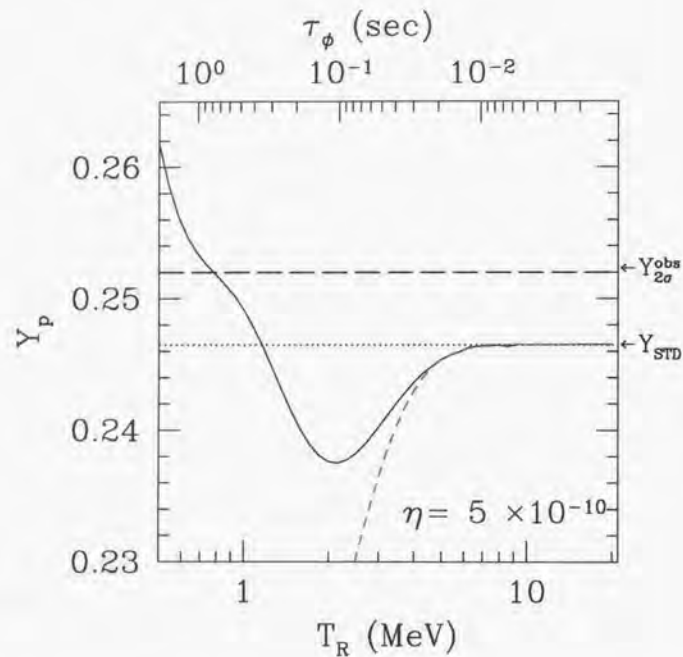


Figure 3.7:  ${}^4\text{He}$  mass fraction  $Y_p$  as a function of  $T_R$  (solid line) at  $\eta = 5 \times 10^{-10}$ . The dashed line denotes the virtual  ${}^4\text{He}$  mass fraction computed by including only the speed down effect due to the change of the effective number of neutrino species which is shown in Fig. 3.4. The dotted line denotes the value predicted in SBBN at  $\eta = 5 \times 10^{-10}$ . The long-dashed line denotes the observational  $2\sigma$  upper bound,  $Y_p^{\text{obs}} \sim 0.252$  which is obtained by summing the errors in quadrature. The top horizontal axis denotes the lifetime which corresponds to  $T_R$ .

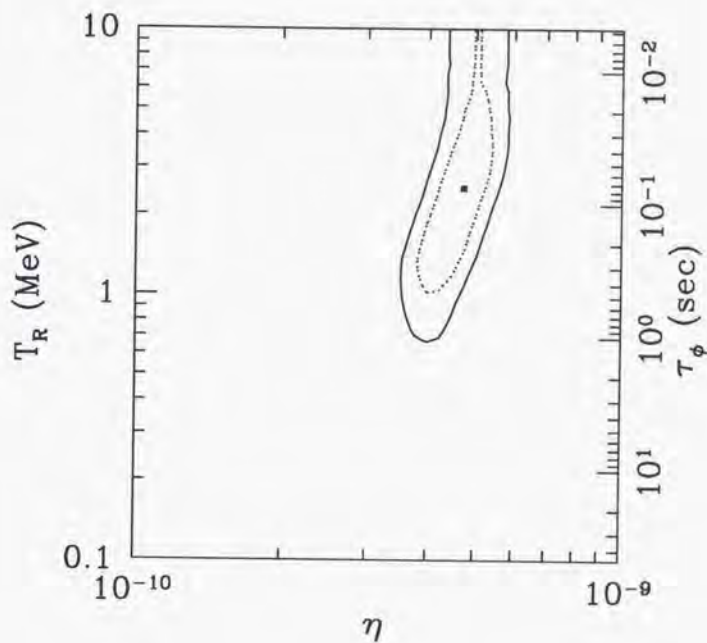


Figure 3.8: Contours of the confidence levels in  $(\eta, T_R)$  plane. The inner (outer) curve is 68% (95%) C.L. The filled square denotes the best fit point. The right vertical axis represents the lifetime which corresponds to  $T_R$ .

### 3.4 Hadron injection by massive particle decay

#### 3.4.1 Hadron Jets and $e^+e^-$ collider experiments

In the previous section we discussed only the case in which the parent massive particle  $\phi$  decays into photons or the other electro-magnetic particles. In this section we consider the entropy production process along with the hadron injection, *i.e.* the case in which the massive particle has some decay modes into quarks or gluons. Then the emitted quark-antiquark pairs or gluons immediately fragment into hadron jets and as a result a lot of mesons and baryons, *e.g.* pions, kaons, nucleons (protons and neutrons) are emitted into the electro-magnetic thermal bath which is constituted by photon, electron and nucleons.

For example, if the gravitino  $\psi_\mu$  is the parent particle which produces the large entropy, it could have a hadronic decay mode (*e.g.*  $\psi_\mu \rightarrow \tilde{\gamma}q\bar{q}$ ) with the branching ratio  $B_h \simeq \mathcal{O}(\alpha)$  at least even if the main decay mode is only  $\psi_\mu \rightarrow \tilde{\gamma}\gamma$  ( $\tilde{\gamma}$ : photino) [56]. Then about 0.6 - 3 hadrons are produced for  $m_\phi \simeq 1 - 100$  TeV. In addition the emitted high energy photons whose energy is about  $m_\phi/2$  scatter off the background photons and could also produce the quark-antiquark pairs through the electromagnetic interaction. For the cosmic temperature  $\simeq \mathcal{O}(\text{MeV})$ , the energy in the center of mass frame is  $\sqrt{s} \simeq 2 - 20$  GeV for  $m_\phi \simeq 1 - 100$  TeV. Then the number of the produced hadrons is about 2 - 7 which effectively corresponds to the hadron branching ratio  $B_h \sim 10^{-2}$  if we assume that the hadron fragmentation is similar to the results of  $e^+e^-$  collider experiments. Thus  $B_h$  should not become less than about  $10^{-2}$  for gravitino decay.<sup>3</sup> For the other candidate, if the "flaton" is the parent particle as in thermal inflation model, it would also have a hadronic decay mode ( $\phi \rightarrow gg$ ) [40] if the flaton mass is larger than 1 GeV.

If once such hadrons are emitted to the electro-magnetic thermal bath in the beginning of the BBN epoch (at  $T \simeq 10 \text{ MeV} - 0.1 \text{ MeV}$ ), they quickly transfer all the kinetic energy into the thermal bath through the electro-magnetic interaction or the strong interaction. Through such thermalization processes the emitted high energy hadrons scatter off the background particles, and then they induce some effects on BBN. Especially, the emitted hadrons extraordinarily inter-convert the ambient protons and neutrons each other through the strong interaction even after the freeze-out time of the neutron to proton ratio  $n/p$ . For the relatively short lifetime ( $\tau_\phi \simeq 10^{-2} \text{ sec} - 10^2 \text{ sec}$ ) in which we are interested, the above effect induces the significant change in the previous discussion. Namely protons which are more abundant than neutrons are changed into neutrons by the hadron-proton collisions and the ratio  $n/p$  increases extremely. Because  ${}^4\text{He}$  is the most sensitive to the freeze out value of  $n/p$ , the late-time hadron injection scenario tends to increase  $Y_p$ .

Reino and Seckel [57] investigated the influences of the hadron injection on the early stage of BBN. They constrained the lifetime of the parent particle and the number density comparing the theoretical prediction of the light element abundances with the observational

<sup>3</sup>If the decay mode  $\psi_\mu \rightarrow \tilde{g}g$  ( $\tilde{g}$ : gluino) is kinematically allowed, the hadronic branching ratio becomes close to one.

data. Here we basically follow their treatment and apply it to the scenario of late-time entropy production with hadron injections.

The emitted hadrons do not scatter off the background nucleons directly. At first hadrons scatter off the background photons and electrons because they are much more abundant than nucleons. For  $t \lesssim 200 \text{ sec}$ , the emitted high energy hadrons are immediately thermalized through the electro-magnetic scattering and they reach to the kinetic equilibrium before they interact with the ambient protons and neutrons. Then we use the threshold cross section  $\langle\sigma v\rangle_{N \rightarrow N'}^{H_i}$  for the strong interaction process  $N + H_i \rightarrow N' + \dots$  between hadron  $H_i$  and the ambient nucleon  $N$ , where  $N$  denotes proton  $p$  or neutron  $n$ . The strong interaction rate is estimated by

$$\begin{aligned} \Gamma_{N \rightarrow N'}^{H_i} &= n_N \langle\sigma v\rangle_{N \rightarrow N'}^{H_i} \\ &\simeq 10^8 \text{ sec}^{-1} f_N \left(\frac{\eta}{10^{-9}}\right) \left(\frac{\langle\sigma v\rangle_{N \rightarrow N'}^{H_i}}{10 \text{ mb}}\right) \left(\frac{T}{2 \text{ MeV}}\right)^3, \end{aligned} \quad (3.30)$$

where  $n_N$  is the number density of the nucleon species  $N$ ,  $\eta$  is the baryon to photon ratio ( $= n_B/n_\gamma$ ),  $n_B$  denotes the baryon number density ( $= n_p + n_n$ ) and  $f_N$  is the nucleon fraction ( $\equiv n_N/n_B$ ). This equation shows that every hadron whose lifetime is longer than  $\mathcal{O}(10^{-6})$  sec contributes to the inter-converting interaction between neutron and proton at the beginning of BBN. Hereafter we will consider only the following long-lived hadrons, (mesons,  $\pi^\pm$ ,  $K^\pm$  and  $K_L$ , and baryons,  $p$ ,  $\bar{p}$ ,  $n$ , and  $\bar{n}$ ). As we will also discuss in detail in the next chapter (Sec. 4.1), for the relevant process ( $N + \pi^\pm \rightarrow N' \dots$ , and  $N + K^\pm \rightarrow N' \dots$ , etc.), we can obtain the cross sections in [57, 58]. Here we ignore  $K^+$  interaction because  $n + K^+ \rightarrow p + K^0$  is the endothermic reaction which has  $Q = 2.8 \text{ MeV}$ .

We estimate the average number of emitted hadron species  $H_i$  per one  $\phi$  decay as

$$N^{H_i} = B_h N_{jet} f_{H_i} \frac{\langle N_{ch} \rangle}{2}, \quad (3.31)$$

where  $\langle N_{ch} \rangle$  is the averaged charged-particle multiplicity which represents the total number of the charged particles emitted per two hadron jets,  $f_{H_i}$  is the number fraction of the hadron species  $H_i$  to all the emitted charged particles,  $B_h$  is the branching ratio of the hadronic decay mode and  $N_{jet}$  is the number of the produced jets per one  $\phi$  decay.

It is reasonable to assume that the averaged charged-particle multiplicity is independent of the source of the hadron jet. In this thesis we use the data obtained by the  $e^+e^-$  collider experiments and extrapolate it to higher energy scales. A number of experimental data are available at least up to  $\sqrt{s} \simeq 100 \text{ GeV}$  where  $\sqrt{s}$  denotes the center of mass energy. Recently LEP II experiments (ALEPH, DELPHI, L3 and OPAL) yielded useful data for  $\sqrt{s} = 130 - 172 \text{ GeV}$ . One can fit the data by a function,  $\langle N_{ch} \rangle = a + b \exp(c\sqrt{\ln(s/\Lambda^2)})$ , where  $\Lambda$  is the cut-off parameter in the perturbative calculations associated with the onset of the hadronization and  $a$ ,  $b$  and  $c$  are constants [95]. The above functional shape is motivated

by the next-to-leading order perturbative QCD calculations. We fit the data of the  $e^+e^-$  collider experiments for  $\sqrt{s} = 1.4 - 172$  GeV [32] and we find

$$\langle N_{ch} \rangle = 1.73 + 0.268 \exp\left(1.42\sqrt{\ln(s/\Lambda^2)}\right), \quad (3.32)$$

with  $\chi^2 = 90.3$  for 93 data points and the error of the fitting is about 10%. Here we have taken  $\Lambda = 1$  GeV. We assigned systematic errors of 10% for  $\sqrt{s} = 1.4 - 7.8$  GeV because MARK I and  $\gamma\gamma 2$  experiments do not include the systematic errors in their data, see [32]. In Fig. 3.9 and Fig. 3.10 we plot  $\langle N_{ch} \rangle$  for the center of mass energy  $\sqrt{s} = 1$  GeV - 300 GeV and  $\sqrt{s} = 1$  GeV - 100 TeV.

Using the available data [32, 58, 59], we obtain the emitted hadron fraction  $f_{H_i} \equiv n^{H_i}/\langle N_{ch} \rangle$ ,

$$\begin{aligned} f_{\pi^+} &= 0.64, & f_{\pi^-} &= 0.64, \\ f_{K^+} &= 0.076, & f_{K^-} &= 0.076, & f_{K_L} &= 0.054 \\ f_p &= f_{\bar{p}} = 0.035, & f_n &= f_{\bar{n}} = 0.034, \end{aligned} \quad (3.33)$$

where  $n^{H_i}$  is the number of the emitted hadron species  $H_i$  which is defined as the value after both  $K_S$  and  $\Lambda^0$  had completely finished to decay.<sup>4</sup> As we find easily, almost all the emitted particles are pions which are the lightest mesons. To apply the data of the  $e^+e^-$  collider experiments, we take  $\sqrt{s} = 2E_{jet}$  in  $\langle N_{ch} \rangle$  where  $E_{jet}$  denotes the energy of one hadron jet because the  $\langle N_{ch} \rangle$  is obtained by the result for two hadron jets.

### 3.4.2 Formulation in Hadron Injection Scenario

In this section we formulate the time evolution equations in the late-time hadron injection scenario. As we mentioned in the previous section, the hadron injection at the beginning of BBN enhances the inter-converting interactions between neutron and proton equally and the freeze out value of  $n/p$  can be extremely increased. Then the time evolution equations for the number density of a nucleon  $N(=p, n)$  is represented by

$$\frac{dn_N}{dt} + 3H(t)n_N = \left[ \frac{dn_N}{dt} \right]_{weak} - \Gamma_\phi n_\phi (K_{N \rightarrow N'} - K_{N' \rightarrow N}), \quad (3.34)$$

where  $H(t)$  is the Hubble expansion rate,  $[dn_N/dt]_{weak}$  denotes the contribution from the weak interaction rates which are obtained by integrating the neutrino distribution functions as discussed in Sec. 3.3, see Eqs. (3.22 - 3.27),  $n_\phi = \rho_\phi/m_\phi$  is the number density of  $\phi$ ,

<sup>4</sup>Although the summation of  $f_{H_i}$  is obviously more than one, it is because the experimental fitting of  $\langle N_{ch} \rangle$  is defined as a value before  $K_S$  and  $\Lambda^0$  begin to decay [59]. Here we assume that  $f_{H_i}$  do not change significantly in the energy range  $\sqrt{s} \simeq 10$  GeV - 100 TeV. Since we do not have any experimental data for the high energy region more than about 200 GeV, we extrapolate  $\langle N_{ch} \rangle$  to the higher energy regions and we take  $f_{H_i}$  as a constant.

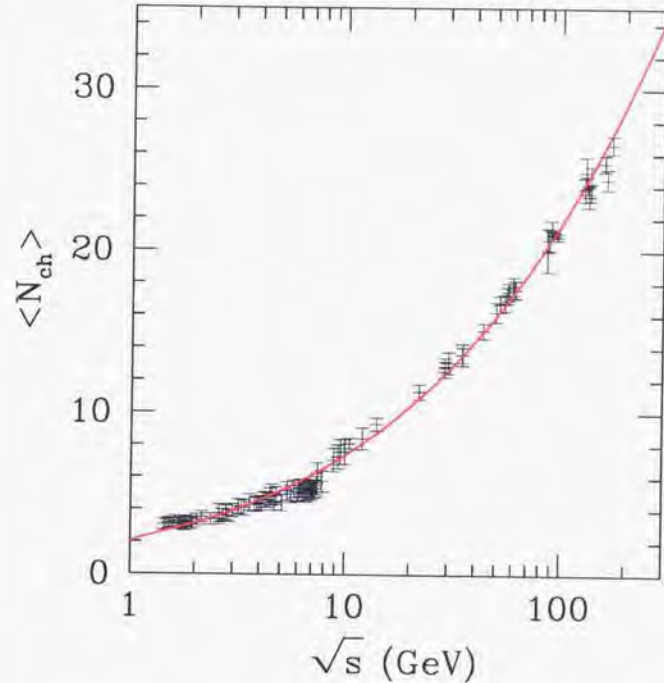


Figure 3.9: Plot of the charged particle multiplicity  $\langle N_{ch} \rangle$  for the center of mass energy  $\sqrt{s}$ . At about  $\sqrt{s} \simeq 91.2$  GeV the experimental data are spread horizontally by authors. We assigned systematic errors of 10% for  $\sqrt{s} = 1.4 - 7.8$  GeV.

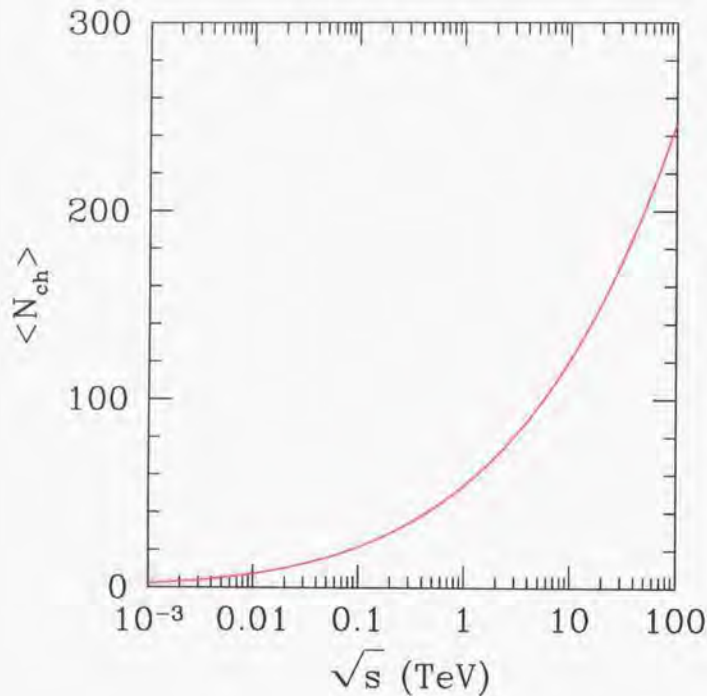


Figure 3.10: Plot of the charged particle multiplicity  $\langle N_{ch} \rangle$  for the center of mass energy  $\sqrt{s} = 1 \text{ GeV} - 100 \text{ TeV}$ .

$K_{N \rightarrow N'}$  denotes the average number of the transition  $N \rightarrow N'$  per one  $\phi$  decay.

The average number of the transition  $N \rightarrow N'$  is expressed by

$$K_{N \rightarrow N'} = \sum_{H_i} N^{H_i} R_{N \rightarrow N'}^{H_i}, \quad (3.35)$$

where  $H_i$  runs the hadron species which are relevant to the nucleon inter-converting reactions,  $N^{H_i}$  denotes the average number of the emitted hadron species  $H_i$  per one  $\phi$  decay which is given by Eq. (3.31) and  $R_{N \rightarrow N'}^{H_i}$  denotes the probability that a hadron species  $H_i$  induces the nucleon transition  $N \rightarrow N'$ ,

$$R_{N \rightarrow N'}^{H_i} = \frac{\Gamma_{N \rightarrow N'}^{H_i}}{\Gamma_{dec}^{H_i} + \Gamma_{abs}^{H_i}}, \quad (3.36)$$

where  $\Gamma_{dec}^{H_i} = \tau_{H_i}^{-1}$  is the decay rate of the hadron  $H_i$  and  $\Gamma_{abs}^{H_i} \equiv \Gamma_{N \rightarrow N'}^{H_i} + \Gamma_{N' \rightarrow N}^{H_i} + \Gamma_{N \rightarrow N}^{H_i} + \Gamma_{N' \rightarrow N'}^{H_i}$  is the total absorption rate of  $H_i$ .

### 3.4.3 Hadron injection and BBN

In this subsection we compare the theoretical prediction of the light element abundances in the hadron injection scenario to the observational light element abundances. In the computations we assume that the massive particle decays into three bodies ( $E_{jet} = m_\phi/3$ ) and two jets are produced at the parton level ( $N_{jet} = 2$ )<sup>5</sup>. In the computing we take the branching ratio of the hadronic decay mode  $B_h = \mathcal{O}(10^{-2} - 1)$ .

As we noted in the previous subsections, it is a remarkable feature that the predicted  $Y_p$  tends to increase in the hadron injection scenario because  ${}^4\text{He}$  is the most sensitive to the freeze-out value of the neutron to proton ratio. Since protons which are more abundant than neutrons are changed into neutrons through the strong interactions rapidly, the freeze out value of  $n/p$  increase extremely if once the net hadrons are emitted. In Fig. 3.11 we plot the predicted  ${}^4\text{He}$  mass fraction  $Y_p$  as a function of  $T_R$  for (a)  $m_\phi = 100 \text{ TeV}$  and (b)  $m_\phi = 10 \text{ GeV}$ . The solid curve denotes the predicted  $Y_p$ . Here we take the branching ratio of the hadronic decay mode as  $B_h = 1$  (right one) and  $B_h = 0.01$  (left one). The dot-dashed line denotes  $B_h = 0$ . The dashed line denotes the virtual value of  $Y_p$  computed by including only the speed down effect due to the change of the effective number of neutrino species. The dotted line denotes the prediction in SBBN.

As we mentioned in the previous section, the speed down effect due to deficit of the electron neutrino distribution function are not important for  $T_R \gtrsim 7 \text{ MeV}$ . In addition since it is high enough to keep  $n/p \simeq 1$  for the cosmic temperature  $T \gtrsim 7 \text{ MeV}$ , the enhancements

<sup>5</sup>The above choice of a set of model parameters  $E_{jet}$  and  $N_{jet}$  is not unique in general and is obviously model dependent. However, since  $\langle N_{ch} \rangle$  has the logarithmic dependence of  $E_{jet}$ , we should not be worried about the modification of  $E_{jet}$  by just a factor of two so seriously. On the other hand in Eq. (3.34), the second term in the right hand side scales as  $\propto N_{jet}/m_\phi$ . For the modification of  $N_{jet}$ , therefore, we only translate the obtained results according to the above scaling rule and push the responsibility off onto  $m_\phi$ .

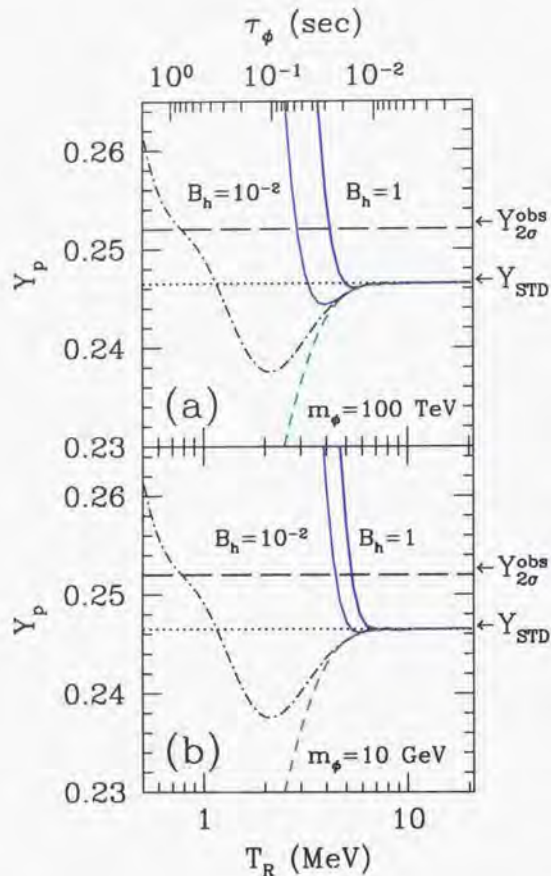


Figure 3.11: Plot of the predicted  ${}^4\text{He}$  mass fraction  $Y_p$  as a function of  $T_R$  for (a)  $m_\phi=100$  TeV and (b)  $m_\phi=10$  GeV at  $\eta = 5 \times 10^{-10}$ . The solid curve denotes the predicted  $Y_p$  where we take the branching ratio of the hadronic decay mode as  $B_h = 1$  (right one) and  $B_h = 0.01$  (left one). The dot-dashed line denotes  $B_h = 0$ . The dashed line denotes the virtual  $Y_p$  curve computed by including only the speed down effect due to the change of the effective number of neutrino species. The dotted line denotes  $Y_p$  in SBBN. The long-dashed line denotes the rough observational two  $\sigma$  upper bound that  $Y_p$  should be less than about 0.252. The top horizontal axis represents the lifetime which corresponds to  $T_R$ .

of the inter-converting interaction between  $n$  and  $p$  due to the hadron emission do not induce any changes on the freeze-out value of  $n/p$ . As  $T_R$  decreases ( $T_R \lesssim 7\text{MeV}$ ),  $Y_p$  also decreases gradually because the speed down effect on the freeze-out value of  $n/p$  begins to be important. On the other hand, if a lot of hadrons are emitted when the cosmic temperature is  $T \lesssim 6 - 7$  MeV and the ratio  $n/p$  is less than one, they enhance the inter-converting interactions more rapidly. As a result, the ratio  $n/p$  attempt to get closer to one again although the cosmic temperature is still low. Thus the above effects extremely increase the freeze-out value of  $n/p$  and is much more effective than the speed down effects. Namely the produced  $Y_p$  becomes larger very sensitively only if  $T_R$  is just a little lower than 6 - 7 MeV. One can obviously find that this effect becomes more remarkable for the larger  $B_h$ .

To understand how it depends on mass, it is convenient to introduce the yield variable  $Y_\phi$  which is defined by

$$Y_\phi \equiv n_\phi/s, \quad (3.37)$$

where  $s$  denotes the entropy density in the universe. Because  $Y_\phi$  is a constant only while the universe expands without any entropy production, it represents the net number density of  $\phi$  per comoving volume. For the simplicity let's consider the instantaneous decay of  $\phi$  and assume that the reheating process has been completed quickly. Because the radiation energy in the thermal bath or entropy  $s = 2\pi^2 g_*/45T_R^3$  is produced only from the decay products of  $\phi$ ,  $Y_\phi$  is approximately estimated using  $T_R$  and  $m_\phi$  by

$$Y_\phi \simeq 0.28 \frac{T_R}{m_\phi}. \quad (3.38)$$

From the above equation, we can see that for the fixed value of  $T_R$  the net number of  $\phi$ , i.e. the net number of the emitted hadrons, becomes larger for the smaller mass. Comparing Fig. 3.11 (a) with Fig. 3.11 (b), we find that the theoretical curve of  $Y_p$  for the case of  $m_\phi = 10$  GeV is enhanced more steeply and the starting point to increase  $Y_p$  becomes higher than for the case of  $m_\phi = 100$  TeV.

Since the other elements ( $D$  and  ${}^7\text{Li}$ ) are not so sensitive as  ${}^4\text{He}$ , it is expected that the observational value of  $Y_p$  constrains  $T_R$  most strongly. In order to discuss how a low reheating temperature is allowed by comparing the theoretical predictions with observational values ( $D$ ,  ${}^4\text{He}$  and  ${}^7\text{Li}$ ), we perform the Monte Carlo simulation and maximum likelihood analysis as discussed in Sec. 3.3. In addition to the case of Sec. 3.3 we take account of the following uncertainties, the error for the fitting of  $\langle N_{ch} \rangle$  as 10% [58] and the experimental error for each cross section of the hadron interaction as 50%. Because there are not any adequate experimental data for the uncertainties of cross sections [57, 58], here we take the larger values to get a conservative constraint.

In Fig. 3.12 we plot the contours of the confidence level for  $m_\phi = 100$  TeV in the  $(\eta-T_R)$  plane for (a)  $B_h = 1$  and (b)  $B_h = 10^{-2}$ . The solid line denotes 95 % C.L., the dotted line denotes 68 % C.L. and the filled square is the best fit point between the observation and

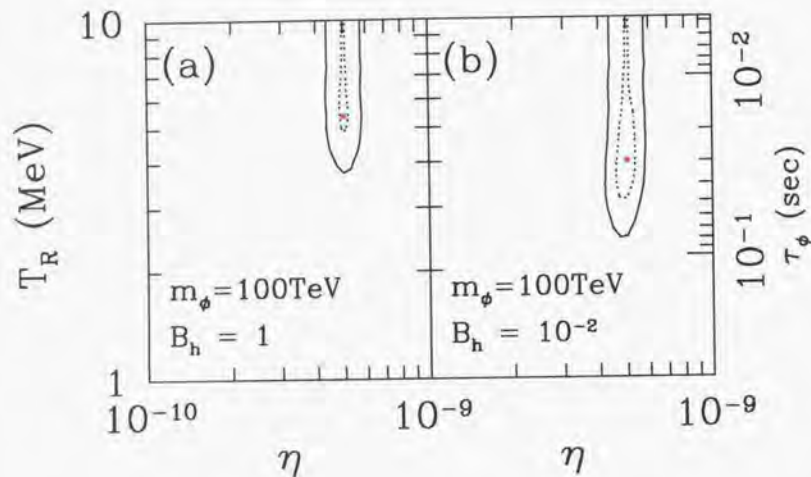


Figure 3.12: Contours of the confidence levels for  $m_\phi = 100$  TeV in  $(\eta, T_R)$  plane for the branching ratio of the hadronic decay mode (a)  $B_h = 1$  and (b)  $B_h = 10^{-2}$ . The solid line denotes 95 % C.L. and the dotted line denotes 68 % C.L. The filled square is the best fit point between the observation and theoretical prediction for D,  ${}^4\text{He}$  and  ${}^7\text{Li}$ . The right vertical axis represents the lifetime which corresponds to  $T_R$ .

theoretical prediction for D,  ${}^4\text{He}$  and  ${}^7\text{Li}$ . The baryon to photon ratio which is consistent with the observational data is restricted in the narrow region,  $\eta \simeq (4 - 6) \times 10^{-10}$ . From Fig. 3.12(a), we find that  $T_R \lesssim 3.7$  MeV is excluded at 95 % C.L. for  $B_h = 1$ . On the other hand, from Fig. 3.12(b) we obtain the milder constraint that  $T_R \lesssim 2.5$  MeV is excluded at 95 % C.L. for  $B_h = 10^{-2}$ . In Fig. 3.13 we plot the contours of the confidence level for  $m_\phi = 10$  GeV in the same way as Fig. 3.12. Compared to Fig. 3.12, as we mentioned above, we find that the lower bound on the reheating temperature becomes higher for a smaller mass. From Fig. 3.13 we get the lower bound on the reheating temperature that  $T_R \gtrsim 5.0$  MeV (4.0 MeV) at 95 % C.L. for  $B_h = 1$  ( $B_h = 10^{-2}$ )

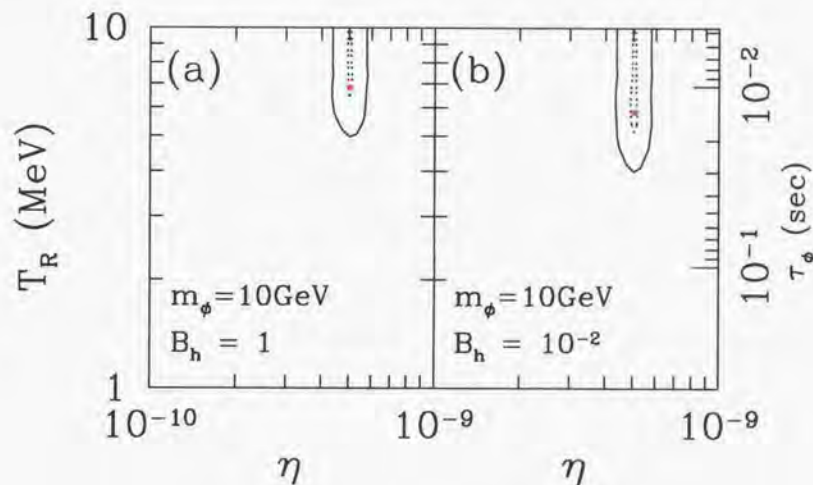


Figure 3.13: Contours of the confidence levels for  $m_\phi = 10$  GeV for the same theory parameters as in Fig. 3.12.

In Fig. 3.14 the lower bound on  $T_R$  as a function of  $m_\phi$  are plotted for (a)  $B_h = 1$  and (b)  $B_h = 10^{-2}$ . The solid line denotes 95 % C.L. and the dotted line denotes 68 % C.L. As it is expected, the curve of the lower bound on  $T_R$  is a gentle monotonic decreasing function

of  $m_\phi$ . In Fig. 3.14(a), we can see that  $T_R$  should be higher than 4 MeV at 95 % C.L. for  $B_h = 1$  in  $m_\phi = 10 \text{ GeV} - 10^2 \text{ TeV}$ <sup>6</sup>. On the other hand, in Fig. 3.14(b) we find that the constraint gets milder for  $B_h = 10^{-2}$ . It is shown that  $T_R \lesssim 2.5 \text{ MeV}$  is excluded at 95 % C.L. for  $B_h = 10^{-2}$ . In Fig. 3.4 we find that  $N_\nu^{\text{eff}}$  can be allowed as small as 2.8 for  $B_h = 1$  (1.9 for  $B_h = 10^{-2}$ ). As we show in the next section, these modifications on  $N_\nu^{\text{eff}}$  might be detected by the future satellite experiments.

### 3.4.4 Summary of hadron injection

In this section we have seen that the BBN constraint on the reheating temperature becomes much more stringent if a massive particle has a branching to hadrons. For successful BBN the reheating temperature should be higher than 2.5 – 4 MeV for the branching ratio  $B_h = 1 - 10^{-2}$ . The hadron injection generally occurs if the late-time reheating is caused by the heavy particle with mass larger than  $\sim 1 \text{ GeV}$ . Many candidates for the late-time reheating such as SUSY particles and flatons have such large masses and hence the constraint obtained here is crucial in constructing particle physics models based on SUSY or thermal inflation models.

For the lower limit of the reheating temperature, the effective number of the neutrino species  $N_\nu^{\text{eff}}$  is given by 2.8 and 1.9 for  $B_h = 1$  and  $10^{-2}$ , respectively. Since the limiting temperature is close to the neutrino decoupling temperature, the deviation of  $N_\nu^{\text{eff}}$  from the standard value (i.e. 3) is small and hence the detection may not be easy.

However, from more general point of view, it is possible that light particles with mass  $\lesssim 1 \text{ GeV}$  are responsible for the late-time reheating. In this case, as seen in the previous section, the reheating temperatures as low as  $\sim 0.7 \text{ MeV}$  are allowed. For such low reheating temperature, neutrinos cannot be produced sufficiently. Thus the effective number of the neutrino species  $N_\nu^{\text{eff}}$  becomes much less than 3. This leads to very interesting effects on the formation of large scale structures and CMB anisotropies, which we discuss in the next section.

## 3.5 Constraints from Large Scale Structure and CMB anisotropy

In this section, we discuss possibility to set constraints on the late-time entropy production from the large scale structure and CMB anisotropies. Hereafter, we only consider flat universe models with cosmological constant which are suggested by recent distant Supernovae (SNe) surveys [60, 61] and measurements of CMB anisotropies [62].

The late-time entropy production influences formation of the large scale structure and

<sup>6</sup>Though we have adopted the experimental error of the each hadron interaction cross section as 50% in the Monte Carlo simulation because of no data, the lower bound on  $T_R$  might become about 10% higher than the above values if we adopt the more sever experimental error as 10% instead of 50%.

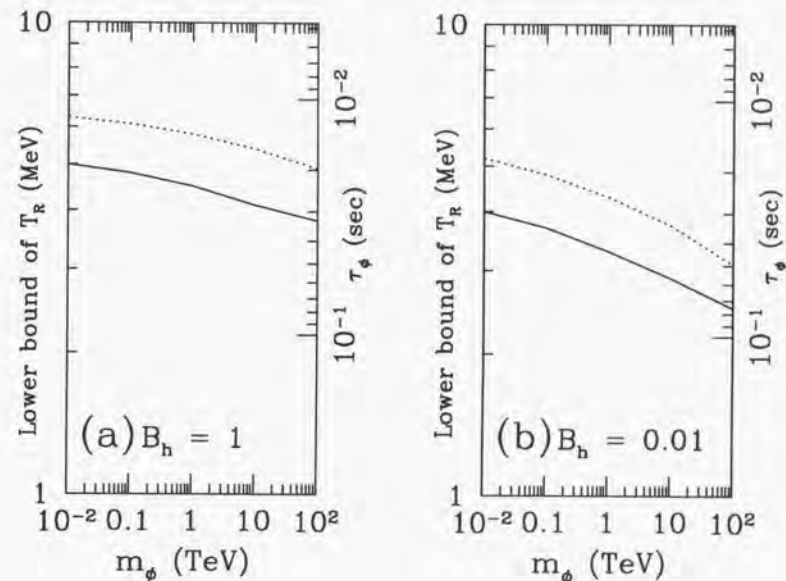


Figure 3.14: Lower bound on  $T_R$  as a function of  $m_\phi$  for the branching ratio of the hadronic decay mode (a)  $B_h = 1$  and (b)  $B_h = 10^{-2}$ . The solid line denotes 95 % C.L. and the dotted line denotes 68 % C.L. The right vertical axis represents the lifetime which corresponds to  $T_R$ .

CMB anisotropies since the matter-radiation equality epoch is shifted if the effective number of neutrino species changes. The ratio of neutrino density to black-body photon density is  $\rho_\nu/\rho_\gamma = (7/8)(4/11)^{4/3} N_\nu$ . Therefore the redshift of matter-radiation equality can be written as a function of  $N_\nu$ :

$$1 + z_{\text{eq}} = 4.03 \times 10^4 \Omega_0 h^2 \left( 1 + \frac{7}{8} \left( \frac{4}{11} \right)^{4/3} N_\nu \right)^{-1}, \quad (3.39)$$

where  $\Omega_0$  is the density parameter and  $h$  is the non-dimensional Hubble constant normalized by 100 km/s/Mpc.

Let us now discuss distribution of galaxies on large scales. For a quantitative analysis, we define the matter power spectrum in Fourier space as  $P(k) \equiv \langle |\delta_k|^2 \rangle$ , where  $\delta_k$  is the Fourier transform of density fluctuations and  $\langle \rangle$  denotes the ensemble average. Hereafter, we assume the Harrison-Zel'dovich power spectrum, which is motivated by the inflation scenario, as an initial shape of the power spectrum, i.e.,  $P(k) \propto k$ . As fluctuations evolve in the expanding universe, the shape of the power spectrum is changed. One often introduces the transfer function  $T(k)$  to describe this modification of the initial power spectrum as  $P(k) = AkT(k)^2$ , where  $A$  is an arbitrary constant. In case of standard cold dark matter (CDM) dominated models, Bardeen et al. [63] found a fitting formula:

$$T(k) = \frac{\ln(1 + 2.34q)}{2.34q} [1 + 3.89q + (16.1q)^2 + (5.46q)^3 + (6.71q)^4]^{-1/4}, \quad (3.40)$$

where  $q = k/\Omega_0 h^2 \text{Mpc}^{-1}$  when the baryon density is negligible small compared to the total density. It is easy to explain why  $q$  is parameterized by  $\Omega_0 h^2$ . This is because CDM density fluctuations cannot evolve and stagnate during a radiation dominated era. Only after the matter-radiation equality epoch, fluctuations can evolve. Therefore the CDM power spectrum has a peak which corresponds to the horizon scale of the matter-radiation equality epoch. In fact, the wave number of the horizon scale at the equality epoch can be written as  $k_{\text{eq}} = \sqrt{2\Omega_0(1 + z_{\text{eq}})} H_0$ , where  $H_0$  is the Hubble constant at present, that is proportional to  $\Omega_0 h^2$ . In the actual observations, distances in between galaxies are measured in the units of  $h^{-1} \text{Mpc}$ . Therefore to fit the observational data by the CDM type power spectrum, we usually introduce so-called *shape parameter*  $\Gamma_s = \Omega_0 h$ . It is known that we can fit the galaxy distribution if  $\Gamma_s \simeq 0.25 \pm 0.05$  [64] which suggests a low density universe. If the late-time entropy production takes place, however, we need to take into account  $N_\nu^{\text{eff}}$  dependence of the matter-radiation equality epoch (Eq. (3.39)). Therefore  $\Gamma_s$  should be written as

$$\Gamma_s = 1.68 \Omega_0 h / (1 + 0.227 N_\nu^{\text{eff}}). \quad (3.41)$$

We plot contours of  $\Gamma_s$  on  $\Omega_0 - N_\nu^{\text{eff}}$  plane in Fig. 3.15. It is shown that smaller  $\Omega_0$  is preferable for  $N_\nu^{\text{eff}} < 3$  with the same value of  $\Gamma_s$ . We also plot the power spectra for  $\Omega_0 = 0.3$  and  $h = 0.7$  with different  $N_\nu^{\text{eff}}$ 's in Fig. 3.16. Here we do not simply employ the fitting formula

but numerically solve the evolution of density fluctuations [65]. It is shown that the peak location of a model with smaller  $N_\nu^{\text{eff}}$  shifts to the smaller scale (larger in  $k$ ) since smaller  $N_\nu^{\text{eff}}$  makes the equality epoch earlier which means the horizon scale at the equality epoch becomes smaller. We have hope that current large scale structure surveys such as 2DF and Sloan Digital Sky Survey (SDSS) may determine the precise value of  $\Gamma_s$ .

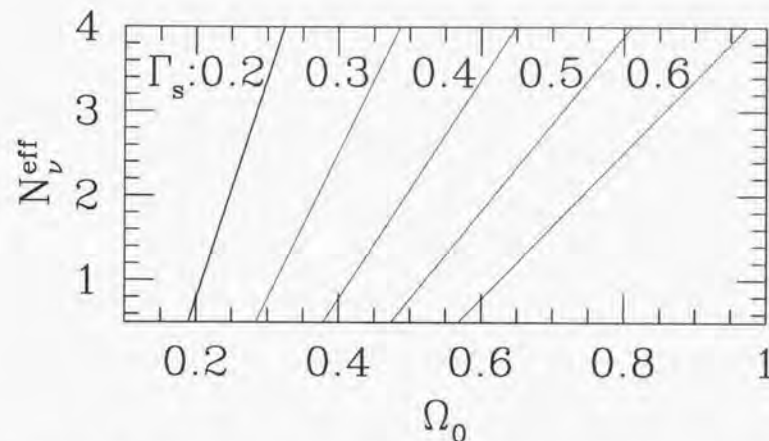


Figure 3.15: Contours of  $\Gamma_s = 0.2$  (bold), 0.3, 0.4, 0.5 and 0.6 on the  $(\Omega_0, N_\nu^{\text{eff}})$  plane for  $h = 0.7$ .

Besides the shape of the power spectrum, the amplitude is another important observational quantities to test models. On very large scales, the amplitude of the power spectrum is determined by CMB anisotropies which are measured by COBE/DMR [45]. Since COBE/DMR scales are much larger than the horizon scale of the matter-radiation equality epoch, however, it is not sensitive to the transfer function  $T(k)$  but the overall amplitude  $A$ . In order to compare the expected amplitude of the power spectrum from each CDM model with large scale structure observations, we employ the specific mass fluctuations within a sphere of a radius of  $8h^{-1} \text{Mpc}$ , i.e.,  $\sigma_8$  which is defined as

$$\begin{aligned} \sigma_8^2 &= \langle (\delta M/M(R))^2 \rangle_{R=8h^{-1} \text{Mpc}} \\ &= \frac{1}{2\pi^2} \int dk k^2 P(k) W(kR)^2 |_{R=8h^{-1} \text{Mpc}}, \end{aligned} \quad (3.42)$$

where  $W(kR)$  is a window function for which we employ a top hat shape as  $W(kR) \equiv 3(\sin(kR) - kR \cos(kR))/(kR)^3$ . Eke et al. [66] obtained the observational value of  $\sigma_8$  which

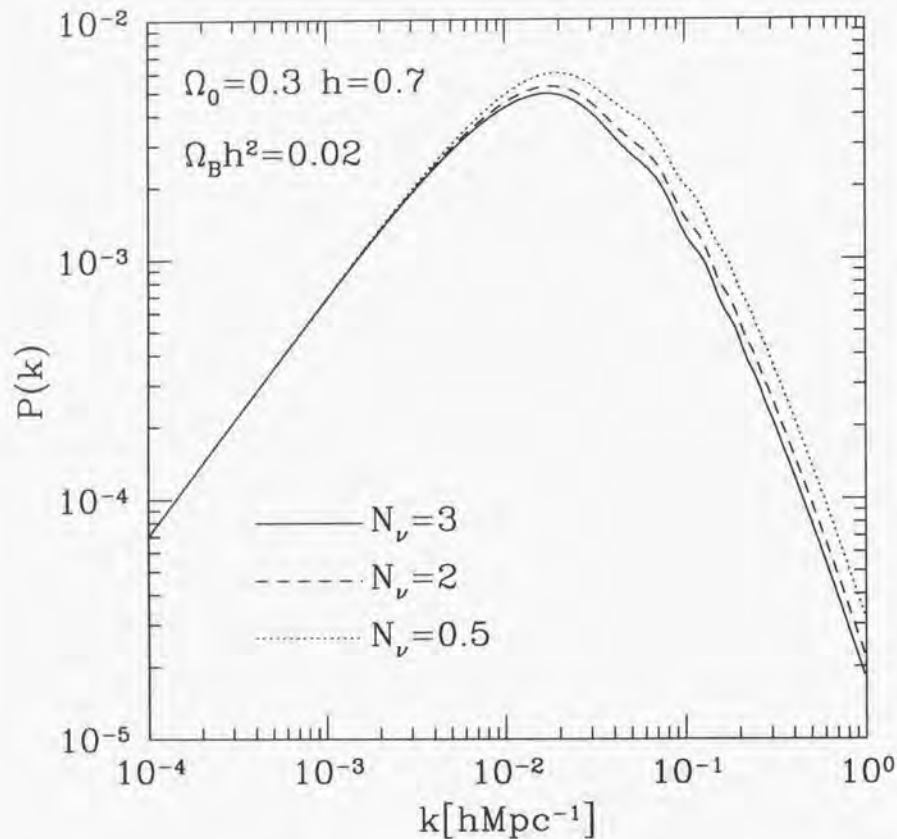


Figure 3.16: Matter power spectra  $P(k)$  of CDM models with  $N_\nu^{\text{eff}} = 0.5, 2, \text{ and } 3$ . We take  $\Omega_0 = 0.3, h = 0.7$ , and  $\Omega_B h^2 = 0.02$  where  $\Omega_B$  is the baryon density parameter.

is deduced from the rich cluster abundance at present as

$$\sigma_8 = (0.52 \pm 0.04) \Omega_0^{-0.52+0.13\Omega_0}. \quad (3.43)$$

Other estimates of  $\sigma_8$  [67] are agreed with their result. For CDM models with standard thermal history, the value of  $\sigma_8$  is a function of  $\Omega_0$  and  $h$ . With the late-time reheating, however,  $\sigma_8$  for fixed  $\Omega_0$  and  $h$  becomes larger. The reason is following. Since we fix  $\Omega_0$  and  $h$ , the normalization factor  $A$  is same regardless of the value of  $N_\nu^{\text{eff}}$ . As is shown in Fig. 3.16, the amplitude of the power spectrum on  $8h^{-1}\text{Mpc}$ , i.e.,  $\sigma_8$ , is larger for smaller  $N_\nu^{\text{eff}}$ . In Fig. 3.17, we show the allowed region on the  $\Omega_0 - h$  plane for  $N_\nu^{\text{eff}} = 0.5, 2$  and  $3$  for COBE-normalized flat CDM models with the Harrison-Zel'dovich spectrum. The shaded region satisfies the matching condition with the cluster abundance Eq. (3.43). For fixed  $h$ , models with smaller  $N_\nu^{\text{eff}}$  prefer lower  $\Omega_0$ . Recently, the HST key project on the Extragalactic Distance Scale has reported that  $h = 0.71 \pm 0.06$  ( $1\sigma$ ) by using various distant indicators [68]. From SNe measurements,  $\Omega_0 = 0.28 \pm 0.8$  for flat models (see Fig. 7 of [61]). CDM models with  $N_\nu^{\text{eff}} = 0.5 \sim 3$  are still consistent with above value of  $h$  and  $\Omega_0$ . However we expect further precise determination of  $\Omega_0, h$  (from distant SNe surveys and measurements of CMB anisotropies) and  $\sigma_8$  (from 2DF or SDSS) will set a stringent constraint on  $N_\nu^{\text{eff}}$  and  $T_R$  in near future.

Finally we discuss the CMB constraint on  $T_R$ . Let us introduce temperature angular power spectrum  $C_\ell$  where  $\ell$  is the multipole number of the spherical harmonic decomposition. The rms temperature anisotropy of CMB can be written as  $\langle |\Delta T/T|^2 \rangle = \sum_\ell (2\ell+1) C_\ell / 4\pi$ . Using  $C_\ell$ , we can extract various important information of cosmology, such as the curvature of the universe,  $\Omega_0$ , cosmological constant,  $h$  and so on (see, e.g., [69]). In fact, we can measure the matter radiation equality epoch by using the height of peaks of  $C_\ell$ . The peaks are boosted during the matter-radiation equality epoch. If the matter-radiation equality is earlier, the correspondent horizon scale is smaller. Therefore we expect lower heights for first one or two peaks since these peaks are larger than the horizon scale at the equality epoch and do not suffer the boost as is shown in Fig. 3.18. With the present angular resolutions and sensitivities of COBE observation [45] or current balloon and ground base experiments, however, it is impossible to set a constraint on  $N_\nu^{\text{eff}}$ . It is expected that future satellite experiments such as MAP [46] and PLANCK [47] will give us a useful information about  $N_\nu^{\text{eff}}$ . From Lopez et al.'s analysis [44], MAP and PLANCK have sensitivities that  $\delta N_\nu^{\text{eff}} \gtrsim 0.1$  (MAP) and  $0.03$  (PLANCK) including polarization data, even if all cosmological parameters are determined simultaneously (see also Fig. 3.18). From such future observations of anisotropies of CMB, it is expected that we can precisely determine  $T_R$ .

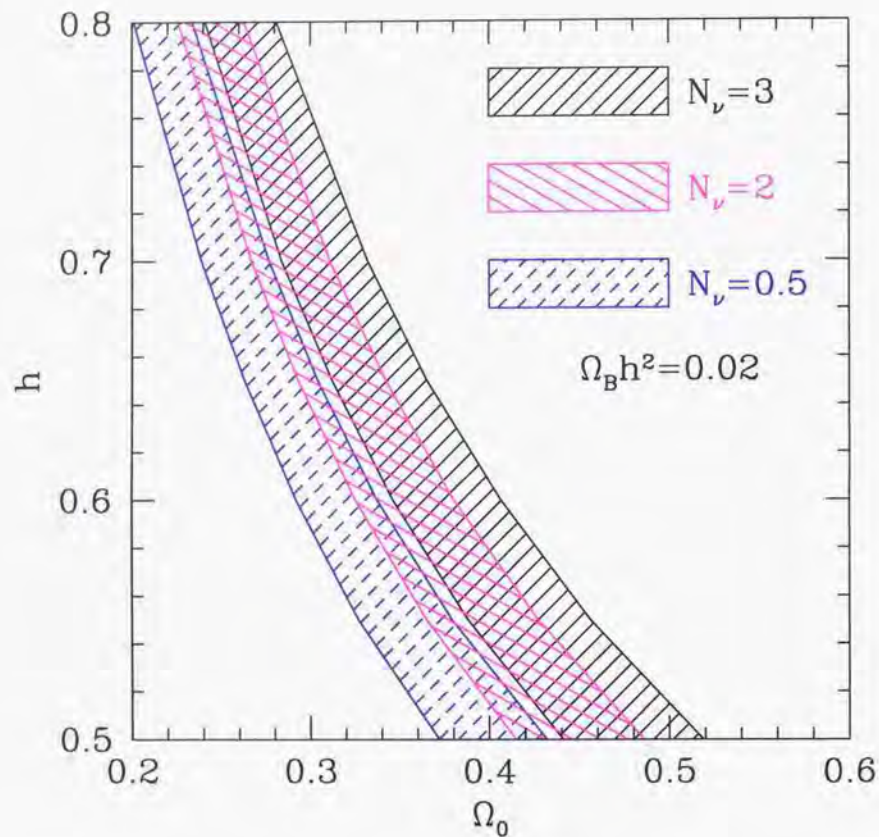


Figure 3.17: Allowed region on  $\Omega_0 - h$  plane from observational values of  $\sigma_8$  deduced from the rich cluster abundance at present for flat CDM models. Models with  $N_\nu^{\text{eff}} = 0.5, 2$ , and 3 are plotted.

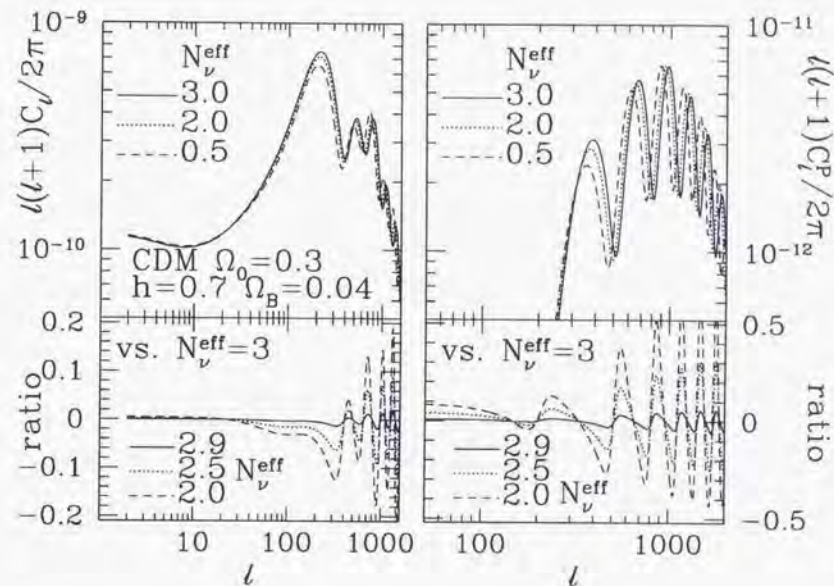


Figure 3.18: Power spectra of CMB anisotropies (left top panel) and polarization (right top panel) of models with  $N_\nu^{\text{eff}} = 3, 2$  and  $0.5$ . Bottom two panels show  $(C_l(N_\nu^{\text{eff}}) - C_l(3))/C_l(3)$  with  $N_\nu^{\text{eff}} = 2.9, 2.5$  and  $2.0$  for CMB anisotropies (left bottom) and polarization (right bottom).

### 3.6 Lower bound of reheating temperature : Summary

In this chapter we have investigated the various cosmological effects induced by the late-time entropy production due to the massive particle decay. The neutrino distribution functions have been obtained by solving the Boltzmann equations numerically. We have found that if the large entropy is produced at about  $t \simeq 1$  sec, the neutrinos are not thermalized very well and hence do not have the perfect Fermi-Dirac distribution. The deficits of the neutrino distribution functions due to the insufficient thermalization decrease the Hubble expansion rate and weaken the weak interaction rates between proton and neutron. The above two effects change the freeze-out value of  $n/p$  significantly. Especially the produced  ${}^4\text{He}$  mass fraction  $Y$  is so sensitive to  $n/p$  that the predicted value of  $Y$  is changed drastically. Comparing the theoretical predictions of D,  ${}^4\text{He}$  and  ${}^7\text{Li}$  to the observational data, we have estimated the lower bound on the reheating temperature  $T_R$  after the entropy production. We have found that  $T_R \lesssim 0.7$  MeV is excluded at 95 % C.L. In other words,  $T_R$  can be as low as 0.7 MeV. Then the effective number of neutrino species  $N_\nu^{\text{eff}}$  can be as small as 0.1. It is enough sensitive for the ongoing large scale structure observations such as 2DF and SDSS or future satellite experiments (MAP and PLANCK) of CMB anisotropies to detect such modifications on  $N_\nu^{\text{eff}}$  and we can find out the vestige of the late-time entropy production.

Furthermore, we have also studied the case in which the massive particle has some decay modes into quarks or gluons. In this scenario, a lot of hadrons, *e.g.* pions, kaons, protons and neutrons, which are originated by the fragmentation of the high energy quarks and gluons, are injected into thermal bath. The emitted hadrons extraordinarily inter-convert the ambient protons and neutrons each other through the strong interaction even after the freeze-out time of the neutron to proton ratio  $n/p$ . Then the predicted value of  $Y$  increases extremely and we can constrain  $T_R$  and the branching ratio of the hadronic decay mode  $B_h$  comparing to the observational light element abundances. We have found  $T_R$  should be higher than 2.5 MeV - 4 MeV at 95 % C.L. for  $B_h = 10^{-2} - 1$ . The above results tell us that  $N_\nu^{\text{eff}}$  can be as small as 1.9 - 2.8 even in the hadron injection scenario for  $B_h = 10^{-2} - 1$ . Then it still may be possible to detect the modifications on  $N_\nu^{\text{eff}}$  by MAP and PLANCK.

## Chapter 4

# Hadron injection from Primordial Black holes and BBN

### 4.1 Evaporation of Primordial Black Hole and BBN : overview

Primordial black holes (PBHs) are formed in the hot early Universe if overdensity of order of unity exists and a perturbed region enters the Hubble radius [70]. They serve as a unique probe of primordial density fluctuations on small scales. For example, if massive compact halo objects (MACHOs) [71] found by gravitational microlensing observation toward the Large Magellanic Clouds turn out to be the PBHs, which originate from density fluctuations generated during inflation, we can determine model parameters of the inflation model with high accuracy [72]. In fact, this possibility is attracting more attention these days because none of the conventional candidates of MACHOs are plausible from various astrophysical considerations and observations.

Even the nonexistence of PBHs over some mass ranges, however, would provide useful informations on the primordial spectrum of density fluctuations. In this sense it is very important to obtain accurate constraints on the abundance of PBHs on each mass scale.

Cosmological constraints on the mass spectrum of the PBHs can be classified to three classes. The first one applies to heavy black holes with mass  $M > 4 \times 10^{14}\text{g}$  which have not evaporated by now. Current mass density of such holes should not exceed the total mass density of the universe. More stringent constraints are obtained from the microlensing experiments on holes with sub-solar masses [71]. The second class is due to the radiation of high energy particles from evaporating black holes [73, 74]. Various constraints have been imposed from primordial big-bang nucleosynthesis (BBN) [75, 76, 77, 78, 79], microwave background radiation [80], and gamma-ray background radiation [81]. Finally, there may be yet another class of constraints if PBHs do not evaporate completely but leave relics with mass of order of the Planck mass or larger [82]. Their mass density should remain small enough.

The purpose of this chapter is to reanalyze the effects of evaporating primordial black

holes on BBN in order to improve constraints on their mass spectrum. Although extensive work was done on this issue in 1970s just after the idea of PBH was proposed, to our knowledge, it has not been studied almost two decades now, and old constraints are still used in the literature [83, 84]. In order to compare the previous work with the modern view of BBN and high energy physics, we start with a brief review of what has been done on the subject.

Vainer and Nasel'skii [75] studied the effects of the injection of high-energy neutrinos and antineutrinos which change the epoch of the freeze out of the weak interactions and also the neutron-to-proton ratio at the onset of the nucleosynthesis. This results in the increase of  ${}^4\text{He}$ . Demanding that its primordial abundance,  $Y_p$ , should satisfy  $Y_p < 0.33$ , they concluded the ratio of the energy density of PBHs to that of baryons should be smaller than  $10^{-10}$  for holes with mass  $M = 10^9 - 3 \times 10^{11}$  g. This approximately corresponds to  $\beta(M) < 10^{-22} - 10^{-19}$ , where  $\beta(M)$  is the initial fraction of PBHs with mass  $M$  to the total energy density of the universe when the horizon mass is equal to  $M$ , *i.e.*  $\beta(M) \equiv (\rho_{\text{PBH}}/\rho_{\text{tot}})_i$ . These authors also studied the effects of entropy generation from PBHs but they obtained a modest constraint that the energy density of the relevant holes should be smaller than that of the photons at evaporation.

More detailed numerical analysis of the latter effect was done by Miyama and Sato [76], who calculated the effect of entropy production from PBHs with mass  $M = 10^9 - 10^{13}$  g evaporating during or after the nucleosynthesis. If these PBHs were too abundant, the baryon-to-entropy ratio at the nucleosynthesis should be increased which would result in overproduction of  ${}^4\text{He}$  and underproduction of D. They demanded that  $Y_p < 0.29$  and that mass fraction of D should be larger than  $1 \times 10^{-5}$ . If we approximate their result with a single power law, we find

$$\beta(M) < 10^{-15} M_{10}^{-5/2}, \quad (4.1)$$

for  $M = 10^9 - 10^{13}$  g, where  $M_{10} \equiv M/10^{10}$  g.

Zel'dovich et al [77], on the other hand, studied the effect of emission of high-energy nucleons and antinucleons from PBHs. They claimed such emission would increase deuterium abundance due to capture of free neutrons by protons and spallation of  ${}^4\text{He}$  by emitted particles. Their conclusions were

$$\begin{aligned} \beta(M) &< 6 \times 10^{-18} M_{10}^{-1/2}, & \text{for } M = 10^9 - 10^{10} \text{ g,} \\ &< 6 \times 10^{-22} M_{10}^{-1/2}, & \text{for } M = 10^{10} - 5 \times 10^{10} \text{ g,} \\ &< 3 \times 10^{-23} M_{10}^{5/2}, & \text{for } M = 5 \times 10^{10} - 5 \times 10^{11} \text{ g,} \\ &< 3 \times 10^{-21} M_{10}^{-1/2}, & \text{for } M = 10^{11} - 10^{13} \text{ g.} \end{aligned} \quad (4.2)$$

Vainer, Dryzhakova, and Nasel'skii [78] then performed numerical integration of nucleosynthesis network in the presence of neutron-antineutron injection, taking the neutron

lifetime to be  $918(\pm 14)$  sec and using the observational data  $Y_p = 0.29 \pm 0.04$  and the mass fraction of D to be  $5 \times 10^{-5}$ . They calculated spallation of  ${}^4\text{He}$  and resultant extra production of D assuming that PBHs were produced out of scale-invariant density fluctuations. As a result they obtained the constraint  $\beta < 10^{-26}$  for the relevant mass range.

Lindley [79] considered another effect of evaporating PBHs with mass  $M > 10^{10}$  g, namely, photodissociation of deuterons produced in the nucleosynthesis. He found the constraint  $\beta \lesssim 3 \times 10^{-20} M_{10}^{1/2}$ , and concluded that photodestruction was comparable to the extra production of deuterons discussed in [77].

Since these papers were written, both observational data of light elements and the neutron lifetime have changed considerably [85]. More important, however, is the change in our view of high energy physics of the energy scale relevant to PBHs evaporating in the nucleosynthesis era. That is, hadrons are not emitted in the form of nucleons or mesons but as a quark-gluon jet in the modern view of quantum chromodynamics (QCD). Thus we should adopt the Elementary Particle Picture of Carr [74] and assume that elementary particles in the standard model are emitted from PBHs and they generate jets. In fact, the number of jet-generated particles far exceeds that of directly emitted counterparts. In this sense the previous calculation of BBN in the presence of evaporating PBHs should be entirely revised. The above procedure has already been taken in the analysis of cosmic rays from evaporating PBHs [86]. We incorporate emission of various hadrons from PBH-originated jets to BBN for the first time.

We adopt a simple and conventional view that PBHs are produced with a single mass,  $M$ , when the horizon mass is equal to  $M$ , namely at  $t = 2.4 \times 10^{-29} M_{10} \text{ sec} \equiv t_{\text{form}}$ , and obtain an improved constraints on their initial abundance at each mass scale. Recent numerical calculations of PBH formation, however, have revealed the mass spectrum of PBHs spreads rather widely even if the spectrum of primordial density fluctuation is sharply peaked on a specific scale [87, 88]. In particular, the authors of [87] discovered the critical behavior and its cosmological consequences have been discussed in [89]. By convolving our results with the mass functions obtained in these papers, one can obtain constraints on PBH formation in more realistic situations.

When PBHs evaporate and emit various particles in the BBN epoch, *i.e.* at  $T = 10 \text{ MeV} - 1 \text{ keV}$ , such high energy particles interact with the ambient photons, electrons and nucleons and they finally transfer all the kinetic energy into the thermal bath through the electromagnetic interaction or the strong interaction. Through the above process, such dangerous high energy particles possibly induce the various effects on the background and change the standard scenario considerably.

Once quark-antiquark pairs or gluons are emitted from a PBH, a lot of hadrons, *e.g.* pions, kaons and nucleons (protons and neutrons) are produced through their hadronic fragmentation. They inter-convert the ambient protons and neutrons each other through the strong interaction. If the inter-conversion rate between neutrons and protons becomes large again after the freeze-out time of the weak interactions in the standard BBN (SBBN) or

$t \simeq 1$  sec, the protons which are more abundant than the neutrons at that time are changed into neutrons. That is, this results in an excess of neutrons compared to SBBN. Therefore, the hadron injection significantly influences the freeze-out value of the neutron-to-proton ratio and the final abundances of  ${}^4\text{He}$ , D and  ${}^7\text{Li}$  are drastically changed. In this case it is expected that both  ${}^4\text{He}$  and D tend to become more abundant than in SBBN. If PBHs are so massive that they continue to emit particles even after  ${}^4\text{He}$  are produced, then spallation of  ${}^4\text{He}$  due to high energy particles will tend to increase the final D <sup>1</sup>. In this chapter, as a first step of the full analysis, we concentrate on the low-mass PBHs and consider only the former effects. The latter issue will be addressed in a separate publication [94].

Reno and Seckel [57] investigated the detail of the physical mechanism and the influences of the hadron injection from long-lived massive decaying particles on BBN. They constrained the parent particle's lifetime and the number density comparing the theoretical prediction of the light element abundances with the observational data. Here we basically follow their treatment and apply it to the hadron injection originated in the PBH evaporation.

## 4.2 Evaporation and Jets

First we briefly summarize basic results of PBH evaporation. As was first shown by Hawking [73], a black hole with mass  $M$  emits thermal radiation with the temperature given by

$$T_{\text{BH}} = \frac{1}{8\pi GM} = 1.06 M_{10}^{-1} \text{TeV}. \quad (4.3)$$

More precisely, a neutral non-rotating black hole emits particles with energy between  $Q$  and  $Q + dQ$  at a rate

$$d\dot{N}_s = \frac{\Gamma_s dQ}{2\pi} \frac{1}{e^{(Q/T_{\text{BH}})} - (-1)^{2s}}, \quad (4.4)$$

where  $s$  is the spin of the emitted particle.  $\Gamma_s$  is its dimensionless absorption coefficient whose functional shape is found in [90]. It is related with the absorption cross section  $\sigma_s(M, Q)$  as  $\Gamma_s(M, Q) = Q^2 \sigma_s(M, Q)/\pi$ . In the high-energy limit  $Q \gg T$ ,  $\sigma_s$  approaches to the geometric optics limit  $\sigma_g \equiv 27\pi G^2 M^2$ .

The average energies of a neutrino, an electron, and a photon are given by  $E_\nu = 4.22T_{\text{BH}}$ ,  $E_e = 4.18T_{\text{BH}}$ , and  $E_\gamma = 5.71T_{\text{BH}}$ , respectively. The peak energy of the flux and that of the power are within 7% of the above values [91]. Averaging over degrees of freedoms of quarks and gluons in the standard model, we find the average energy  $\bar{E} = 4.4T_{\text{BH}}$ .

MacGibbon elaborated on the lifetime of a PBH,  $\tau_{\text{BH}}$ , summing up the contribution of

<sup>1</sup>This situation has been studied in [93] in the context of late-decaying particles.

all the emitted particles and integrating the mass loss rate

$$\frac{dM_{10}}{dt} = -5.34 \times 10^{-5} f(M) M_{10}^{-2} \text{sec}^{-1}, \quad (4.5)$$

over the lifetime [92]. The result is approximately given by

$$\tau_{\text{BH}} = 6.24 \times 10^3 f(M)^{-1} M_{10}^3 \text{sec}. \quad (4.6)$$

Here  $f(M)$  is a function of the number of emitted particle species normalized to unity for  $M \gg 10^{17}$ g holes which emit only photons, three generations of neutrinos and anti-neutrinos, and gravitons. Depending on the spin  $s$ , each relativistic degree of freedom contributes to  $f(M)$  as [92]

$$\begin{aligned} f_{s=0} &= 0.267, & f_{s=1} &= 0.060, & f_{s=3/2} &= 0.020, & f_{s=2} &= 0.007, \\ f_{s=1/2} &= 0.147 \text{ (neutral)}, & f_{s=1/2} &= 0.142 \text{ (charge } = \pm e). \end{aligned} \quad (4.7)$$

Summing up contributions of all the particles in the standard model, we find  $f(M) = 14.34$ . In this case the lifetime reads

$$\tau_{\text{BH}} = 435 M_{10}^3 \text{sec}, \quad (4.8)$$

or

$$M = 1.32 \times 10^9 \left( \frac{\tau_{\text{BH}}}{1 \text{sec}} \right)^{\frac{1}{3}} \text{g}. \quad (4.9)$$

Thus a PBH evaporating by the end of BBN  $t \simeq 10^3$  sec has a mass  $M \lesssim 10^{10}$ g and the temperature  $T_{\text{BH}} \gtrsim 1$ TeV.

For such a PBH with temperature higher than the QCD scale,  $\Lambda_{\text{QCD}} \sim 10^{2.5}$ MeV, it has been argued [91] that particles radiated from it can be regarded as asymptotically free at emission. The emitted quarks and gluons fragment into further quarks and gluons until they cluster into the observable hadrons when they have traveled a distance  $\Lambda_{\text{QCD}}^{-1} \sim 10^{-13}$ cm. The hadron jet thus produced would be similar to that produced in  $e^+e^-$  annihilation.

We now estimate the average number of the emitted hadron species  $H_i$  per jet as

$$N^{H_i} = f_{H_i} \frac{\langle N_{ch} \rangle}{2}, \quad (4.10)$$

where  $\langle N_{ch} \rangle$  is the averaged charged-particle multiplicity which represents the total number of the charged particles emitted per two hadron jets,  $f_{H_i}$  is the number fraction of the hadron species  $H_i$  to all the emitted charged particles.

Here it is reasonable to assume that the averaged charged particle multiplicity  $\langle N_{ch} \rangle$  is independent of the the source because the physical mechanism which governs the production of hadron jets is quite similar and does not depend on the detail of the origin only if the high energy quark-antiquark pairs or gluons are emitted. We adopt the data which are obtained by the  $e^+e^-$  collider experiments. We have the following fitting function for  $\sqrt{s} = 1.4 - 172$

GeV [58], which is discussed in the last chapter, see Eq. (3.32).

$$\langle N_{ch} \rangle = 1.73 + 0.268 \exp\left(1.42\sqrt{\ln(s/\Lambda^2)}\right). \quad (4.11)$$

Here we have taken  $\Lambda = 1$  GeV. We assigned systematic errors of 10% for  $\sqrt{s} = 1.4 - 7.8$  GeV and we can find the plots for the center of mass energy  $\sqrt{s} = 1$  GeV - 300 GeV and  $\sqrt{s} = 1$  GeV - 100 TeV in Fig. 3.9 and Fig. 3.10. When we apply the results of the  $e^+e^-$  collider experiments to the case of PBH evaporation, we take  $\sqrt{s} = 2\bar{E}$  as the energy of two hadron jets from the PBH evaporation because we assume that two hadron jets are induced per one quark-antiquark pair emission here. Then we can approximately estimate the average energy of an emitted hadron species  $H_i$  as  $E_{H_i} \simeq \bar{E}/\langle N_{ch} \rangle$ .

The next issue is to find  $f_{H_i}$ . In this thesis we adopt the experimental data of  $f_{H_i}$  at  $\sqrt{s} = 91.2$  GeV, which is the highest energy for which these data are available [32], and we assume that  $f_{H_i}$  do not change significantly in the energy range  $\sqrt{s} \simeq 100$  GeV - 20 TeV.<sup>2</sup> From the table of  $f_{H_i}$  in [32] we must estimate effective  $f_{H_i}$  for each hadron species on the relevant time scale. That is, we must also take into account the decay products of those particles whose lifetime is too short to affect BBN.

Let us estimate the time scale at which we should estimate  $f_{H_i}$ . The emitted hadrons do not scatter off the ambient nucleons directly. At first the emitted high energy hadrons scatter off the background photons and electrons because they are much more abundant than the nucleons. For the most part of the epoch at the cosmic time  $t \lesssim 10^4$  sec, as we can see later, it is expected that the emitted particles are quickly thermalized and they have the kinetic equilibrium distributions before they interact with the ambient nucleons. In addition as we show in Sec. 4.4, it is reasonable to treat the emitted hadrons to be homogeneously distributed. Then we use the thermally averaged cross sections  $\langle \sigma v \rangle_{N \rightarrow N'}$  for the strong interaction between hadron  $H_i$  and the ambient nucleon  $N$ , where  $N$  denotes proton  $p$  or neutron  $n$ . As we discussed in the last chapter, for a hadron interaction process  $N + H_i \rightarrow N' + \dots$ , the strong interaction rate is estimated by

$$\Gamma_{N \rightarrow N'}^{H_i} \simeq 10^8 \text{ sec}^{-1} f_N \left(\frac{\eta_i}{10^{-9}}\right) \left(\frac{\langle \sigma v \rangle_{N \rightarrow N'}^{H_i}}{10 \text{ mb}}\right) \left(\frac{T_\nu}{2 \text{ MeV}}\right)^3, \quad (4.12)$$

where  $n_N$  is the number density of the nucleon species  $N$ ,  $\eta_i$  is the initial baryon to photon ratio ( $= n_B/n_\gamma$  at  $T \gtrsim 10$  MeV),  $n_B = n_p + n_n$  denotes the baryon number density,  $f_N \equiv n_N/n_B$ , and  $T_\nu$  is the neutrino temperature<sup>3</sup>.

<sup>2</sup>The above energy range is approximately the PBH's temperature corresponding to the lifetime  $\tau_{\text{BH}} = 10^{-1} - 10^4$  sec. For  $\sqrt{s} \gtrsim 350$  GeV,  $t$ - $\bar{t}$  pairs would be produced and they would change the form of the charged particle multiplicity and the hadron fraction. Since we do not have the experimental data for such high energy regions, we extrapolate  $\langle N_{ch} \rangle$  to the higher energy regions and we take  $f_{H_i}$  as a constant.

<sup>3</sup>The  $T_\nu$  dependence comes from that the baryon number density decrease as  $n_B \propto R(t)^{-3}$  and the scale factor exactly decrease as  $R(t) \propto T_\nu^{-1}$  while the universe adiabatically expands. If large entropy is produced, the above relation must be changed. In the hadron injection scenario, however, the large entropy

production region is severely excluded. Therefore Eq. (4.12) is a good estimate of the time scale of the hadron interactions.

$$\begin{aligned} n^{\pi^+} &= 14.1, & n^{\pi^-} &= 14.1, \\ n^{K^+} &= 1.67, & n^{K^-} &= 1.67, & n^{K_L} &= 1.19 \\ n^p &= n^{\bar{p}} = 0.772, & n^n &= n^{\bar{n}} = 0.772. \end{aligned} \quad (4.13)$$

In estimating  $n^n$  we have assumed that the number of neutrons emitted directly from a jet is the same as that of protons. Then we obtain the number fraction  $f_{H_i}$  by

$$f_{H_i} = \frac{n^{H_i}}{\langle N_{ch}(\sqrt{s} = 91.2 \text{ GeV}) \rangle}. \quad (4.14)$$

## 4.3 Hadron injection and BBN

### 4.3.1 Hadron scattering off the background particles

When there are sufficient electrons and positrons in the universe ( $T \gtrsim 0.025$  MeV), it is expected that such charged mesons are quickly thermalized through the Coulomb scattering. Since the stopping time to lose the relativistic energy is estimated as

$$\tau_{ch} \simeq 10^{-14} \text{ sec} (E/\text{GeV}) / (T/\text{MeV})^2 \quad (4.15)$$

where  $E$  is the kinetic energy of a charged meson, the long-lived charged mesons are thermalized and scatter off the ambient nucleons by the threshold cross section before they decay [57]. The thermally averaged cross sections for  $\pi^\pm$  are obtained by [57]

$$\langle \sigma v \rangle_{n \rightarrow p}^{\pi^+} = 1.7 \text{ mb}, \quad (4.16)$$

$$\langle \sigma v \rangle_{p \rightarrow n}^{\pi^-} = 1.5 C^H(T) \text{ mb}, \quad (4.17)$$

where  $C^H(T)$  is the Coulomb correction factor. Because the reaction  $p^+ + \pi^- \rightarrow n + \dots$  is enhanced due to the opposite-sign charge of the initial state particles, we correct the strong interaction rates by multiplying  $C^H(T)$  to that which are obtained by ignoring the Coulomb corrections. The Coulomb correction factor is estimated by

$$C^H(T) = \frac{2\pi\xi_i(T)}{1 - e^{-2\pi\xi_i(T)}}, \quad (4.18)$$

production region is severely excluded. Therefore Eq. (4.12) is a good estimate of the time scale of the hadron interactions.

where  $\xi_n(T) = \alpha \sqrt{\mu_i/2T}$ ,  $\alpha$  is the fine structure constant and  $\mu_i$  is the reduced mass of the hadron  $H_i$  and the nucleon.

The cross sections for  $K^-$  are obtained by [57]

$$\langle \sigma v \rangle_{n \rightarrow p}^{K^-} = 26 \text{ mb}, \quad (4.19)$$

$$\langle \sigma v \rangle_{n \rightarrow n}^{K^-} = 34 \text{ mb}, \quad (4.20)$$

$$\langle \sigma v \rangle_{p \rightarrow n}^{K^-} = 31 C^K(T) \text{ mb}, \quad (4.21)$$

$$\langle \sigma v \rangle_{p \rightarrow p}^{K^-} = 14.5 C^K(T) \text{ mb}. \quad (4.22)$$

Following Reno and Seckel [57] we ignore  $K^+$  interaction because  $n + K^+ \rightarrow p + K^0$  is the endothermic reaction which has  $Q = 2.8 \text{ MeV}$ .

On the other hand, among neutral kaons,  $K_L$  has a long lifetime  $\mathcal{O}(10^{-8}) \text{ sec}$ . Since  $K_L$  does not stop through the electro-magnetic interactions, we adopt the following strong interaction cross sections which are obtained by the initial energy distribution in the hadron fragmentation [57],

$$\langle \sigma v \rangle_{n \rightarrow p}^{K_L} = 7 \text{ mb}, \quad (4.23)$$

$$\langle \sigma v \rangle_{n \rightarrow n}^{K_L} = 10 \text{ mb}, \quad (4.24)$$

$$\langle \sigma v \rangle_{p \rightarrow n}^{K_L} = 7 \text{ mb}, \quad (4.25)$$

$$\langle \sigma v \rangle_{p \rightarrow p}^{K_L} = 10 \text{ mb}. \quad (4.26)$$

As for the emitted high energy nucleons, we should treat the thermalization process more carefully because the stopping process is not so simple. Proton and antiproton are stable and we should worry about the efficiency to lose the kinetic energy at the lower temperature. At least  $T \gtrsim 0.02 \text{ MeV}$ , protons are quickly thermalized through Coulomb scattering off the electrons and Inverse Compton scattering off the photons. For  $t \gtrsim 3 \times 10^3 \text{ sec}$ , on the other hand, the stopping process of protons proceeds through the nuclear collisions with the ambient protons and light elements. In this case such high energy protons may induce the  ${}^3\text{He}$  fissions because  ${}^4\text{He}$  has already been synthesized at around  $t \simeq 300 \text{ sec}$ . For neutron and antineutron the efficiency of the thermalization is more severe. Neutrons are efficiently stopped by the electron scattering until  $T \simeq 0.09 \text{ MeV}$ . Thus the late time emission of the high energy neutron would induce the light element fissions. However, in this thesis we treat the neutrons as if they are approximately thermalized in the entire parameter range because we are primarily concerned with the effects of low-mass PBHs here. We follow the Reno and Seckel's treatment that a nucleon-antinucleon pair is regarded as a meson  $N\bar{N}$ . Then the  $N\bar{N}$  meson induces the inter-converting reactions like  $N + N\bar{N} \rightarrow N' + \dots$  and the thermally averaged cross sections are given by [57]

$$\langle \sigma v \rangle_{n \rightarrow n}^{n\bar{n}} = 37 \text{ mb}, \quad (4.27)$$

$$\langle \sigma v \rangle_{p \rightarrow n}^{n\bar{n}} = 28 \text{ mb}, \quad (4.28)$$

$$\langle \sigma v \rangle_{n \rightarrow p}^{p\bar{p}} = 28 \text{ mb}, \quad (4.29)$$

$$\langle \sigma v \rangle_{p \rightarrow p}^{p\bar{p}} = 37 \text{ mb}. \quad (4.30)$$

The above treatment may underestimate the deuterium abundance because it will be produced by the hadro-dissociation of  ${}^4\text{He}$  if PBHs are so massive that they continue to emit high-energy hadrons even after  ${}^4\text{He}$  are formed. The hadron-induced dissociation process of the light elements will be discussed in a separate paper [94]. For the other mesons and baryons whose lifetimes are much shorter, e.g.  $\pi^0 \rightarrow 2\gamma$  with  $\tau_{\pi^0} \simeq \mathcal{O}(10^{-16}) \text{ sec}$ , they quickly decay into the standard particles and do not influence the standard scenario.

On the other hand, for the even longer lifetime  $\tau_{\text{PBH}} \gtrsim 10^4 \text{ sec}$ , there is another interesting effects on BBN. The emitted photons or charged particles induce the electro-magnetic cascade showers and produce many soft photons. Their spectrum has a cutoff at  $E_\gamma^{\text{max}} \simeq m_e^2/(22T)$ , where  $m_e$  is the electron mass [55]. If  $E_\gamma^{\text{max}}$  exceeds the binding energies of the light elements, these photons dissociate light elements and change their abundances. In fact, the energy of the photon spectrum which are produced by the PBH evaporation at  $t \gtrsim 10^4 (10^6) \text{ sec}$  exceeds the deuterium ( ${}^4\text{He}$ ) binding energy  $B_2 \simeq 2.2$  ( $B_4 \simeq 20$ ) MeV. In this case PBH's number density and the lifetime are severely constrained by the observational data of the light element abundances [79].

### 4.3.2 Formulation

As we mentioned in the previous section, the hadron emission mechanism by the PBH evaporation at  $t \lesssim 10^4 \text{ sec}$  induces extra interactions between emitted hadrons and ambient nucleons. That is, they enhance the inter-converting interaction rates between neutron and proton even after the weak interactions has already frozen out in the standard scenario and the freeze out values of  $n/p$  ratio can be increased. The time evolution of the PBH's mass is given by

$$M(t) = \begin{cases} M \left( \frac{\tau_{\text{PBH}} - t}{\tau_{\text{PBH}}} \right)^{\frac{1}{2}} & (\text{for } t \lesssim \tau_{\text{PBH}}), \\ 0 & (\text{for } \tau_{\text{PBH}} \lesssim t), \end{cases} \quad (4.31)$$

where  $M$  is the initial mass of PBH when it was formed.

Then the time evolution equations for the number density of a nucleon  $N (= p, n)$  is represented by

$$\frac{dn_N}{dt} + 3H(t)n_N = \left[ \frac{dn_N}{dt} \right]_{\text{SBBN}} - B_h J(t) (K_{N \rightarrow N'} - K_{N' \rightarrow N}), \quad (4.32)$$

where  $H(t)$  is the cosmic expansion rate,  $[dn_N/dt]_{\text{SBBN}}$  denotes the contribution from the standard weak interaction rates [85] and nuclear interaction rates,  $B_h$  is the hadronic branching ratio,  $J(t)$  denotes the emission rate of the hadron jet per unit time and  $K_{N \rightarrow N'}$  denotes the average number of the transition  $N \rightarrow N'$  per one hadron jet emission. The emission

rate of the hadron jet is estimated by

$$J(t) = \frac{n_{\text{BH}}(t) dM(t)}{E(t) dt}, \quad (4.33)$$

where  $n_{\text{BH}}(t)$  is the number density of the PBHs.

Though PBHs generally emit not only quarks and gluons but also all lighter particle species than the temperature of PBH, the emitted neutrinos, photons and the other electromagnetic particles do not influence the light element abundances significantly for the relatively short lifetime. As we noted in the previous section, for  $\tau_{\text{BH}} \lesssim 10^4$  sec the injection of photon or the other electro-magnetic particles do not induce the photo-dissociation of the light elements. On the other hand, the emitted neutrinos scatter off the background neutrinos and produce the electron-positron pairs. Although they also induce the electro-magnetic cascade, we should not be worried about photo-dissociation for the same reason. Hence we concentrate on the effects of hadron injection in the BBN epoch. Then the resultant upper bound on the abundance of PBHs,  $\beta$ , turns out to be proportional to  $B_h^{-1}$ . Below we analyze the case  $B_h = 1$ , because its magnitude is not precisely known, although we expect  $B_h = \mathcal{O}(0.1 - 1)$ . Anyway the constraint for other cases with  $B_h \neq 1$  can easily be obtained from the above scaling law.

The average number of the transition  $N \rightarrow N'$  per jet is expressed by

$$K_{N \rightarrow N'} = \sum_{H_i} N^{H_i} R_{N \rightarrow N'}^{H_i}, \quad (4.34)$$

where  $H_i$  runs the hadron species which are relevant to the nucleon inter-converting reactions,  $N^{H_i}$  denotes the average number of the emitted hadron species  $H_i$  per jet which is given by Eq. (3.31) and  $R_{N \rightarrow N'}^{H_i}$  denotes the probability that a hadron species  $H_i$  induces the nucleon transition  $N \rightarrow N'$ . The transition probability is estimated by

$$R_{N \rightarrow N'}^{H_i} = \frac{\Gamma_{N \rightarrow N'}^{H_i}}{\Gamma_{dec}^{H_i} + \Gamma_{abs}^{H_i}}, \quad (4.35)$$

where  $\Gamma_{dec}^{H_i} = \tau_{H_i}^{-1}$  is the decay rate of the hadron  $H_i$ ,  $\Gamma_{abs}^{H_i}$  is the total absorption rate of  $H_i$ . For  $K_L$ , which is not stopped, the decay rate is approximately estimated by  $\Gamma_{dec}^{K_L} = m_{K_L}/E_{K_L} \tau_{K_L}^{-1}$  where  $E_{K_L}$  is the averaged energy of the emitted  $K_L$ .

### 4.3.3 Observational constraints

The details of the recent observational light element abundances were discussed in Sec 2.1. In this section, however, in order to get the conservative bound for the hadron injection induced by PBH evaporation, we adopt the following mild observational bounds due to

some ambiguities in the spectrum of the emitted hadrons,

$$Y_p \leq 0.252 (2\sigma), \quad (4.36)$$

$$D/H \leq 4.0 \times 10^{-5} (2\sigma) \quad (4.37)$$

$$3.3 \times 10^{-11} \leq {}^7\text{Li}/H \leq 9.2 \times 10^{-10} (2\sigma), \quad (4.38)$$

where we summed all the errors in quadrature.

## 4.4 Results

In this section we compare the theoretical predictions of the light-element abundances in the hadron injection scenario with the observational constraints. Now we have three free parameters, the baryon to photon ratio  $\eta$ , the PBH's lifetime  $\tau_{\text{BH}}$ , and the initial number density of the PBH normalized by the entropy density,  $s$ ,  $Y_{\text{BH}} \equiv n_{\text{BH}}/s$ . We start the BBN calculation at the cosmic temperature  $T = 100$  MeV. Since  $\eta$  is the value at present time, the initial value  $\eta_i$  should be set to an appropriate value which turns out to the present  $\eta$  after the possible entropy production due to PBH evaporation and the photon heating due to  $e^+e^-$  annihilation. As we noted in the previous sections, the lifetime  $\tau_{\text{BH}}$  characterizes not only the decay epoch, but also the PBH's initial mass  $M$  and the initial PBH temperature  $T_{\text{BH}}$ . Here we can relate  $Y_{\text{BH}}$  to the initial mass fraction  $\beta$  by the following equation:

$$\beta = 5.4 \times 10^{21} \left( \frac{\tau_{\text{BH}}}{1 \text{ sec}} \right)^{\frac{1}{2}} Y_{\text{BH}}. \quad (4.39)$$

Since the hadron injection tends to increase the produced D and  ${}^4\text{He}$  abundances in the present situation, the parameter range of  $\eta$  is necessarily restricted to a narrow region if we adopt a set of the observational upper bounds for D and  ${}^4\text{He}$ . In this situation the baryon-to-photon ratio is roughly restricted in  $\eta = (4.7 - 8.6) \times 10^{-10}$ .

In Fig. 4.1 we plot the upper bounds for  $\beta$  which come from the observational constraints of  ${}^4\text{He}$ , D and  ${}^7\text{Li}$  for the PBH mass  $M = 10^8 - 3 \times 10^{10}$  g at  $\eta = 6.0 \times 10^{-10}$ . The above mass range corresponds to the lifetime  $\tau_{\text{BH}} = 4.4 \times 10^{-4} - 10^4$  sec. As we noted earlier, the shorter lifetime,  $\tau_{\text{BH}} \lesssim 10^{-2}$  sec, do not affect the freeze-out value of  $n/p$  and do not change any predictions of SBBN. However, if the lifetime becomes  $\tau_{\text{BH}} \gtrsim 10^{-2}$  sec, the freeze-out value of  $n/p$  ratio is increased by the hadron-induced inter-converting interactions and the produced neutron increases the  ${}^4\text{He}$  abundance because most of the free neutrons burned into  ${}^4\text{He}$  through D. Then PBH abundance is strongly constrained by the upper bound of the observational  ${}^4\text{He}$  abundance. For  $\tau_{\text{BH}} \gtrsim 10^2$  sec, since the produced free D can no longer burn into  ${}^4\text{He}$ , the extra free neutrons remain in D. Then  $\beta$  is severely constrained by the upper bound of the observational D/H. Though  ${}^7\text{Li}$  abundance traces D abundance for the longer lifetime  $\tau_{\text{BH}} \gtrsim 10^2$  sec and is produced more than SBBN at the relatively high  $\eta$  ( $\gtrsim 3 \times 10^{-10}$ ), the constraint is much weaker than D.

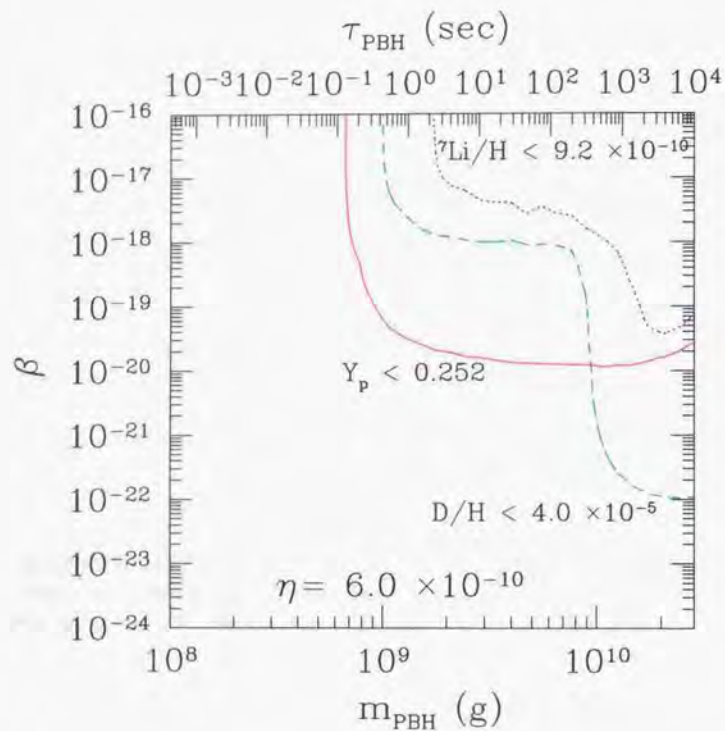


Figure 4.1: Upper bounds for  $\beta$  which come from the observational constraints of  ${}^4\text{He}$  (solid line),  $\text{D}$  (dashed line) and  ${}^7\text{Li}$  (dotted line) as a function of the PBH's mass at  $\eta = 6.0 \times 10^{-10}$ .

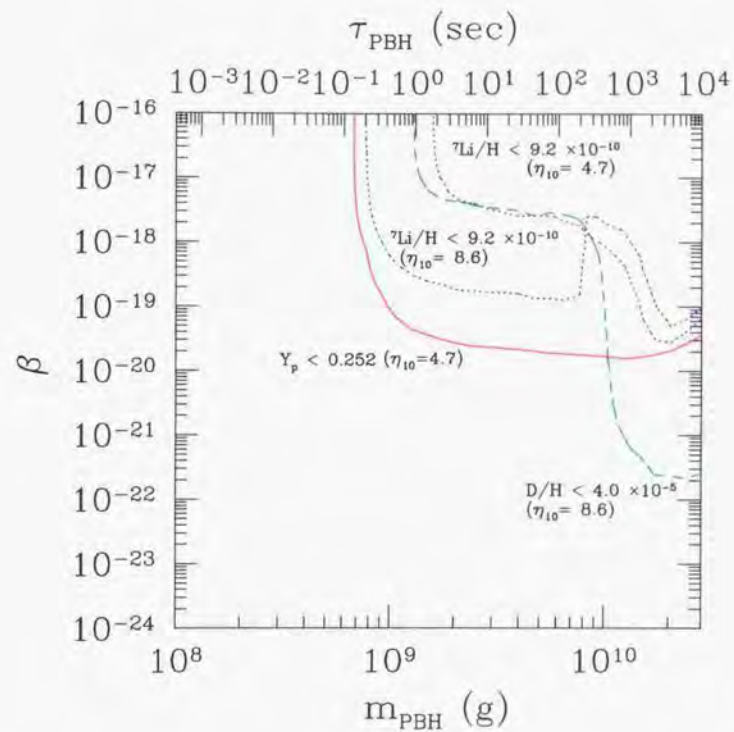


Figure 4.2: The most conservative upper bounds for  ${}^4\text{He}$  (solid line),  $\text{D}$  (dashed line) and  ${}^7\text{Li}$  (dotted line) as mild as possible in the parameter region  $\eta_{10} = 4.7 - 8.6$ , where  $\eta_{10} \equiv \eta \times 10^{10}$ . Here we take "LowD" as a deuterium observational constraint.

In Fig. 4.2 we plot the most conservative bounds in the parameter region  $\eta = (4.7 - 8.6) \times 10^{-10}$ . For  $\tau_{\text{BH}} \lesssim 4 \times 10^2 \text{ sec}$  such a bound is obtained by  $Y_p$  at  $\eta = 4.7 \times 10^{-10}$ . For  $4 \times 10^2 \lesssim \tau_{\text{BH}} \lesssim 10^4 \text{ sec}$ , the prediction of D/H at  $\eta = 8.6 \times 10^{-10}$  gives the most conservative bound for  $\beta$ , but constraints in this region is not quantitatively accurate because we did not include spallation of  ${}^4\text{He}$  produced.

Finally we estimate the number of PBHs within the neutron diffusion length  $d_n(t)$  at  $t = \tau_{\text{BH}}$ . The neutron diffusion length is given by [96]

$$d_n(t) = 5.8 \times 10^2 \left( \frac{T}{1 \text{ MeV}} \right)^{-\frac{5}{2}} \left( \frac{\sigma_t}{3 \times 10^{-30} \text{ cm}} \right)^{-\frac{1}{2}}, \quad (4.40)$$

where  $\sigma_t$  is a transport cross section. Using Eq. (4.8), the number of PBHs within the horizon length at  $t = \tau_{\text{BH}}$  is given by

$$N_H(\tau_{\text{BH}}) = \left( \frac{\tau_{\text{BH}}}{t_{\text{form}}} \right)^{\frac{3}{2}} \beta = 7.7 \times 10^{46} M_{10}^3 \beta. \quad (4.41)$$

Then the number of PBHs within the neutron diffusion length is estimated by

$$N_d(\tau_{\text{BH}}) = \begin{cases} 1.2 \times 10^{21} \beta & , \quad (\text{for } \tau_{\text{BH}} = 1 \text{ sec}), \\ 2.3 \times 10^{46} \beta & , \quad (\text{for } \tau_{\text{BH}} = 10^3 \text{ sec}). \end{cases} \quad (4.42)$$

Compared to Figs. 4.1 - 4.2, we can see that there exist sufficiently many PBHs within the neutron diffusion length in the relevant parameter spaces in which we are interested and the number of PBHs is observationally constrained. Therefore it is justified that we can take the emitted hadrons as a homogeneously distributed background.

## 4.5 Constraints of the PBH evaporation : summary

We have investigated the influence of hadron injection from evaporating PBHs in the early stage of the BBN epoch ( $t \simeq 10^{-3} - 10^4 \text{ sec}$ ). The above lifetimes correspond to the mass range of PBHs  $M \simeq 10^8 - 3 \times 10^{10} \text{ g}$ . When quark-antiquark pairs or gluons are emitted from PBH, they immediately fragment into a lot of hadrons (pions, kaons and little nucleons) and the produced hadron jets are injected into the thermal plasma which is constituted by photons, electrons and nucleons. After the emitted hadrons are sufficiently stopped through the electro-magnetic interaction with the ambient photons and electrons, they can scatter off the ambient nucleons and they inter-convert proton and neutron each other. As a result more neutrons are produced and the synthesized light element abundances are drastically changed. In particular,  ${}^4\text{He}$  and D abundances are very sensitive to the neutron abundance and tend to increase in this scenario. Comparing with the observational data, we can constrain PBH's density and their lifetime. The hadron injection which are originated by the direct quark-antiquark pairs or gluons emission from PBHs has never considered at

all in the literature. In this chapter we pointed out that the hadron induced inter-converting interactions between protons and neutrons are very important and the energy density of PBH is severely constrained by the observational data.

We obtain the following upper bounds for the initial mass fraction of PBH  $\beta$  as a function of the initial mass of PBH when they are formed  $\beta \lesssim 10^{-20}$  (for  $10^8 \text{ g} \lesssim M \lesssim 10^{10} \text{ g}$ ) and  $\beta \lesssim 10^{-22}$  (for  $10^{10} \text{ g} \lesssim M \lesssim 3 \times 10^{10} \text{ g}$ ).

## Chapter 5

# Radiative decay of a long-lived massive particle and BBN

### 5.1 BBN + $X$

In this section, we discuss the implications of a radiatively decaying particle  $X$  for BBN. For this purpose, we first discuss the behavior of the photon spectrum induced by  $X$ . Then we show the abundances of the light elements, including the effects of the photodissociation induced by  $X$ . Comparing these abundances with observations, we constrain the parameter space for  $\eta$  and  $X$ .

#### 5.1.1 Photon Spectrum

In order to discuss the effect of high-energy photons on BBN, we need to know the shape of the photon spectrum induced by the primary high-energy photons from  $X$  decay.

In the background thermal bath (which, in our case, is a mixture of photons  $\gamma_{\text{BG}}$ , electrons  $e_{\text{BG}}$ , and nucleons  $N_{\text{BG}}$ ), high-energy photons lose their energy by various cascade processes. In the cascade, the photon spectrum is induced, as discussed in various literature [99]. The important processes in our case are:

- Double-photon pair creation ( $\gamma + \gamma_{\text{BG}} \rightarrow e^+ + e^-$ )
- Photon-photon scattering ( $\gamma + \gamma_{\text{BG}} \rightarrow \gamma + \gamma$ )
- Pair creation in nuclei ( $\gamma + N_{\text{BG}} \rightarrow e^+ + e^- + N$ )
- Compton scattering ( $\gamma + e_{\text{BG}} \rightarrow \gamma + e^-$ )
- Inverse Compton scattering ( $e^\pm + \gamma_{\text{BG}} \rightarrow e^\pm + \gamma$ )

(We may neglect double Compton scattering  $\gamma + e_{\text{BG}} \rightleftharpoons \gamma + \gamma + e^-$ , because Compton scattering is more important for thermalizing high-energy photons.) In our analysis, we numerically solved the Boltzmann equation including the above effects, and obtained the distribution function of photons,  $f_\gamma(E_\gamma)$ . (For details, see Refs. [97, 98].)

In Fig. 5.1.1, we show the photon spectrum for several temperatures  $T$ . Roughly speaking, we can see a large drop-off at  $E_\gamma \sim m_e^2/22T$  for each temperature. Above this threshold, the photon spectrum is extremely suppressed.

The qualitative behavior of the photon spectrum can be understood in the following way. If the photon energy is high enough, then double-photon pair creation is so efficient that this process dominates the cascade. However, once the photon energy becomes much smaller than  $O(m_e^2/T)$ , this process is kinematically blocked. Numerically, this threshold is about  $m_e^2/22T$ , as we mentioned. Then, photon-photon scattering dominates. However, since the scattering rate due to this process is proportional to  $E_\gamma^3$ , photon-photon scattering becomes unimportant in the limit  $E_\gamma \rightarrow 0$ . Therefore, for  $E_\gamma \ll O(m_e^2/T)$ , the remaining processes (pair creation in nuclei and inverse Compton scattering) are the most important.

The crucial point is that the scattering rate for  $E_\gamma \gtrsim m_e^2/22T$  is much larger than that for  $E_\gamma \ll m_e^2/22T$ , since the number of targets in the former case is several orders of magnitude larger than in the latter. This is why the photon spectrum is extremely suppressed for  $E_\gamma \gtrsim m_e^2/22T$ . As a result, if the  $X$  particle decays in a thermal bath with temperature  $T \gtrsim m_e^2/22Q$  (where  $Q$  is the binding energy of a nuclide) then photodissociation is not effective.

#### 5.1.2 Abundance of Light Elements with $X$

Once the photon spectrum is formed, it induces the photodissociation of the light nuclei, which modifies the result of SBBN. This process is governed by the following Boltzmann equation:

$$\frac{dn_N}{dt} + 3Hn_N = \left[ \frac{dn_N}{dt} \right]_{\text{SBBN}} - n_N \sum_{N'} \int dE_\gamma \sigma_{N'\gamma \rightarrow N'}(E_\gamma) f_\gamma(E_\gamma) + \sum_{N''} n_{N''} \int dE_\gamma \sigma_{N''\gamma \rightarrow N}(E_\gamma) f_\gamma(E_\gamma), \quad (5.1)$$

where  $n_N$  is the number density of the nuclei  $N$ , and  $[dn_N/dt]_{\text{SBBN}}$  denotes the SBBN contribution to the Boltzmann equation. To take account of the photodissociation processes, we modified the Kawano code [31], and calculated the abundances of the light elements. The photodissociation processes we included in our calculation are listed in Table 5.1.

The abundances of light nuclides will be functions of the lifetime of  $X$  ( $\tau_X$ ), the mass of  $X$  ( $m_X$ ), the abundance of  $X$  before electron-positron annihilation

$$Y_X^* = n_X/n_\gamma, \quad (5.2)$$

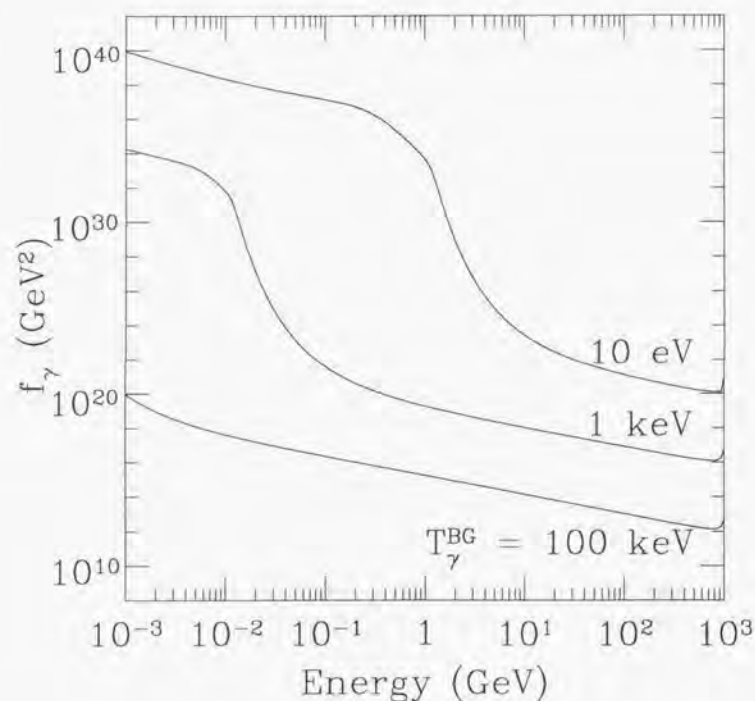


Figure 5.1: Photon spectrum  $f_\gamma = dn_\gamma/dE_\gamma$  for several background temperatures  $T_\gamma^{\text{BG}}$ .

Photofission Reactions	$1\sigma$ Uncertainty	Threshold Energy	Ref.
1. $D + \gamma \rightarrow p + n$	6%	2.2 MeV	[100]
2. $T + \gamma \rightarrow n + D$	14%	6.3 MeV	[101, 102]
3. $T + \gamma \rightarrow p + 2n$	7%	8.5 MeV	[102]
4. ${}^3\text{He} + \gamma \rightarrow p + D$	10%	5.5 MeV	[103]
5. ${}^3\text{He} + \gamma \rightarrow n + 2p$	15%	7.7 MeV	[103]
6. ${}^4\text{He} + \gamma \rightarrow p + T$	4%	19.8 MeV	[103]
7. ${}^4\text{He} + \gamma \rightarrow n + {}^3\text{He}$	5%	20.6 MeV	[104, 105]
8. ${}^4\text{He} + \gamma \rightarrow p + n + D$	14%	26.1 MeV	[106]
9. ${}^6\text{Li} + \gamma \rightarrow \text{anything}$	4%	5.7 MeV	[107]
10. ${}^7\text{Li} + \gamma \rightarrow 2n + \text{anything}$	9%	10.9 MeV	[107]
11. ${}^7\text{Li} + \gamma \rightarrow n + {}^6\text{Li}$	4%	7.2 MeV	[107]
12. ${}^7\text{Li} + \gamma \rightarrow {}^4\text{He} + \text{anything}$	9%	2.5 MeV	[107]
13. ${}^7\text{Be} + \gamma \rightarrow p + {}^6\text{Li}$			
14. ${}^7\text{Be} + \gamma \rightarrow \text{anything except } {}^6\text{Li}$			

Table 5.1: Photodissociation processes, and the  $1\sigma$  uncertainty in the cross sections. Since there is no experimental data on photodissociation of  ${}^7\text{Be}$ , we assume that the rate for Reaction 13 is the same as for Reaction 11, and the rate for Reaction 14 is the sum of the rates for Reactions 10 and 12.

and the baryon-to-photon ratio ( $\eta$ ). In our numerical BBN simulations, we found that the nuclide abundances depend only on the mass abundance  $m_X Y_X$ , not on  $m_X$  and  $Y_X$  separately. In Figs. 5.2 - 5.6, we show the abundances of light nuclei in the  $m_X Y_X$  vs.  $\tau_X$  plane, at fixed  $\eta$ .

We can understand the qualitative behaviors of the abundances in the following way. First of all, if the mass density of  $X$  is small enough, then the effects of  $X$  are negligible, and hence we reproduce the result of SBBN. Once the mass density gets larger, the SBBN results are modified. The effects of  $X$  strongly depend on  $\tau_X$ , the lifetime of  $X$ . As we mentioned in the previous section, photons with energy greater than  $\sim m_X^2/22T$  participate in pair creation before they can induce photofission. Therefore, if the above threshold energy is smaller than the nuclear binding energy, then photodissociation is not effective.

If  $\tau_X \lesssim 10^4$  sec, then  $m_X^2/22T \lesssim 2\text{MeV}$  at the decay time of  $X$ , and photodissociation is negligible for all elements. In this case, the main effect of  $X$  is on the  ${}^4\text{He}$  abundances: if the abundance of  $X$  is large, its energy density speeds up the expansion rate of the universe, so the neutron freeze-out temperature becomes higher. As a result,  ${}^4\text{He}$  abundance is enhanced relative to SBBN.

If  $10^4$  sec  $\lesssim \tau_X \lesssim 10^6$  sec, then  $2\text{ MeV} \lesssim m_X^2/22T \lesssim 20\text{ MeV}$ . In this case,  ${}^4\text{He}$  remains intact, but  $D$  is effectively photodissociated through the process  $D + \gamma \rightarrow p + n$ . When  $\tau_X \gtrsim 10^5$  sec,  $m_X^2/22T \gtrsim 7.7\text{ MeV}$  (the binding energy of  ${}^3\text{He}$ ), so  ${}^3\text{He}$  is dissociated for  $\tau_X \sim 10^5$  sec and large enough abundances  $m_X Y_X \gtrsim 10^{-8}$  GeV. However,  $D$  is even more

	$\tau_X = 10^4$ sec	$10^5$ sec	$10^6$ sec	$10^7$ sec	$10^8$ sec	$10^9$ sec
95% C.L.	$1 \times 10^{-11}$	$8 \times 10^{-9}$	$9 \times 10^{-10}$	$5 \times 10^{-12}$	$6 \times 10^{-13}$	$4 \times 10^{-13}$
68% C.L.	$8 \times 10^{-6}$	$6 \times 10^{-9}$	$8 \times 10^{-10}$	$2 \times 10^{-12}$	$2 \times 10^{-13}$	$2 \times 10^{-13}$

Table 5.2: Upper bound on  $m_X Y_X$  in units of GeV.

fragile than  ${}^3\text{He}$ , so the ratio  ${}^3\text{He}/\text{D}$  actually *increases* relative to SBBN in this region, since it is dominated by D destruction. If the lifetime is long enough ( $\tau_X \gtrsim 10^6$  sec),  ${}^4\text{He}$  can also be destroyed effectively. In this case, the destruction of even a small fraction of the  ${}^4\text{He}$  can result in significant production of D and  ${}^3\text{He}$ , since the  ${}^4\text{He}$  abundance is originally much larger than that of D. This can be seen in Figs. 5.2 and 5.3: for  $\tau_X \gtrsim 10^6$  sec and  $10^{-10}$  GeV  $\lesssim m_X Y_X \lesssim 10^{-9}$  GeV, the abundance of D changes drastically due to the photodissociation of  ${}^4\text{He}$ . Moreover, two-body decays of  ${}^4\text{He}$  into  ${}^3\text{He}$  or T (which decays into  ${}^3\text{He}$ ) are preferred over the three-body decay  ${}^4\text{He} + \gamma \rightarrow p + n + \text{D}$ , so the  ${}^3\text{He}/\text{D}$  ratio increases, relative to SBBN. If  $m_X Y_X$  is large enough, all the light elements are destroyed efficiently, resulting in very small abundances.

So far, we have discussed the theoretical calculation of the light-element abundances in a model with  $X$  decay. In the next section, we compare the theoretical calculations with observations, and derive constraints on the properties of  $X$ .

### 5.1.3 Comparison with Observation

Now, we compare the theoretical calculations with the observed abundances and show how we can constrain the model parameters. Since observationally the D abundance (2.6) and  ${}^4\text{He}$  abundance (2.9) both prefer a relatively middle value of  $\eta$ , the SBBN prediction can be consistent with observation. Therefore, BBN is robust enough to constrain the model parameters. As we discussed for the case of SBBN in Chapter 2, we statistically analyze the theoretical values and the observational data and we find the C.L. at each point in the three dimensional space ( $\eta$ ,  $\tau_X$ , and  $m_X Y_X$ ). In Fig. 5.7, we show the C.L. contours projected along the  $\eta$  axis into the  $\tau_X - m_X Y_X$  plane. As we noted in the last sections, since the small  $m_X Y_X$  reproduces the results of SBBN, the parameter regions below the lines are allowed. Table 5.2 gives the upper bounds on  $m_X Y_X$  (GeV) which correspond to 68% and 95% C.L., for some typical values of the lifetime.

### 5.1.4 Additional Constraints

We now mention additional constraints on our model. Since the cosmic microwave background radiation (CMBR) has been observed by COBE [30] to very closely follow a blackbody spectrum, one may be concerned about the constraint this gives on particles with

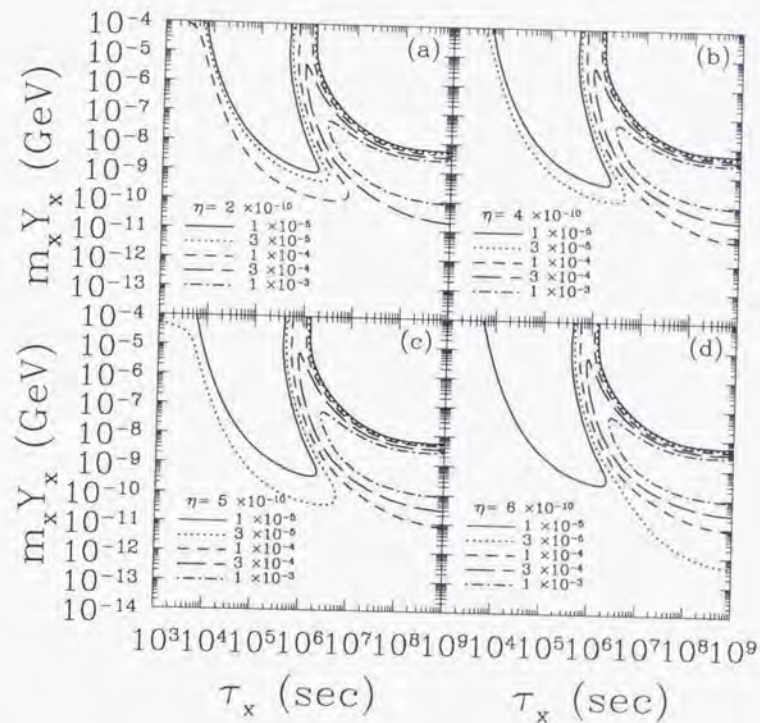


Figure 5.2: The abundance of D/H in the  $m_X Y_X$  vs.  $\tau_X$  plane with (a)  $\eta = 2 \times 10^{-10}$ , (b)  $\eta = 4 \times 10^{-10}$ , (c)  $\eta = 5 \times 10^{-10}$ , and (d)  $\eta = 6 \times 10^{-10}$ .

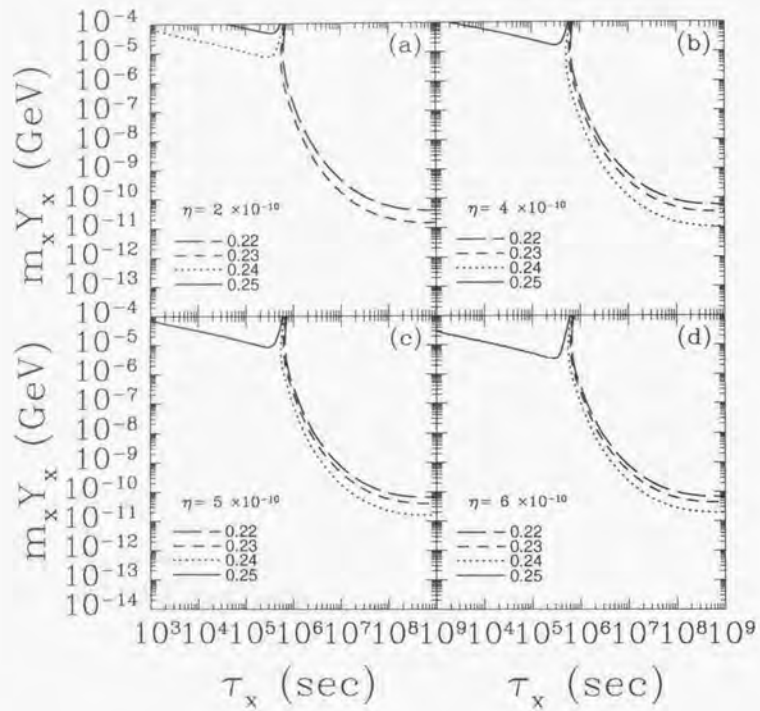


Figure 5.3: The mass fraction of  ${}^4\text{He}$ , for the same theory parameters as in Fig. 5.2.

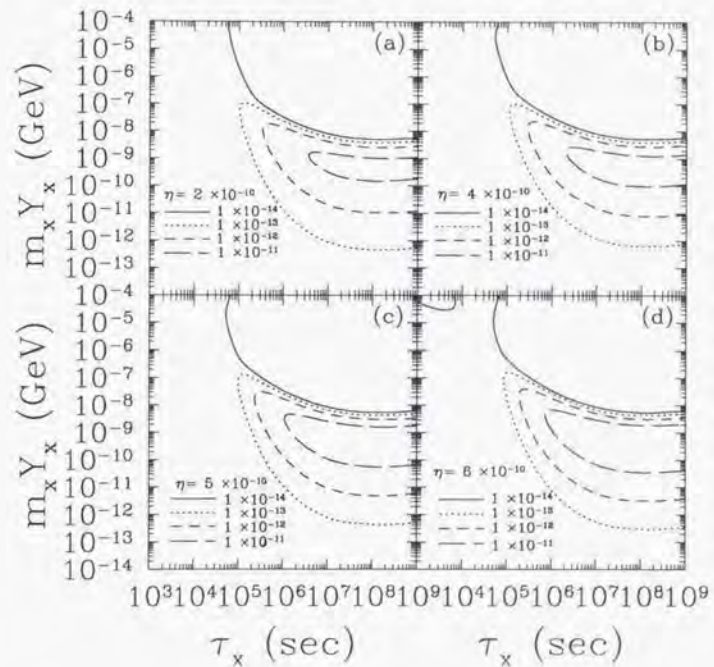


Figure 5.4: The abundance of  ${}^6\text{Li}/\text{H}$ , for the same theory parameters as in Fig. 5.2.

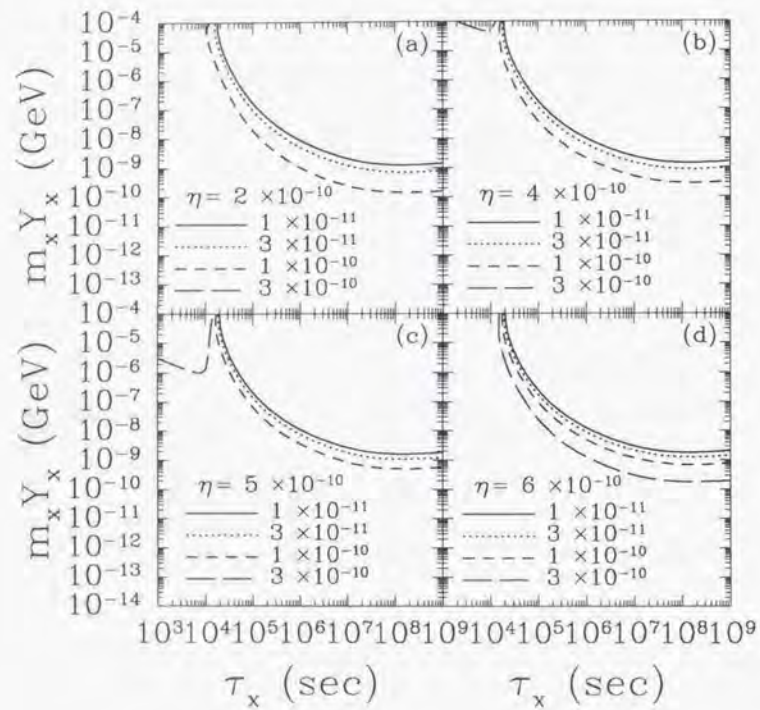


Figure 5.5: The abundance of  ${}^7\text{Li}/\text{H}$ , for the same theory parameters as in Fig. 5.2.

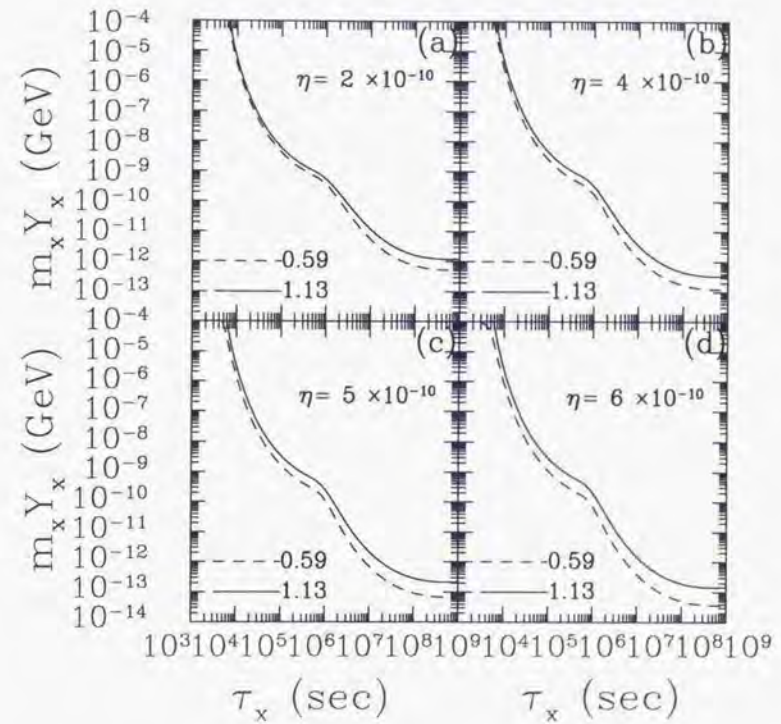


Figure 5.6: The abundance of  ${}^3\text{He}/\text{D}$ , for the same theory parameters as in Fig. 5.2.

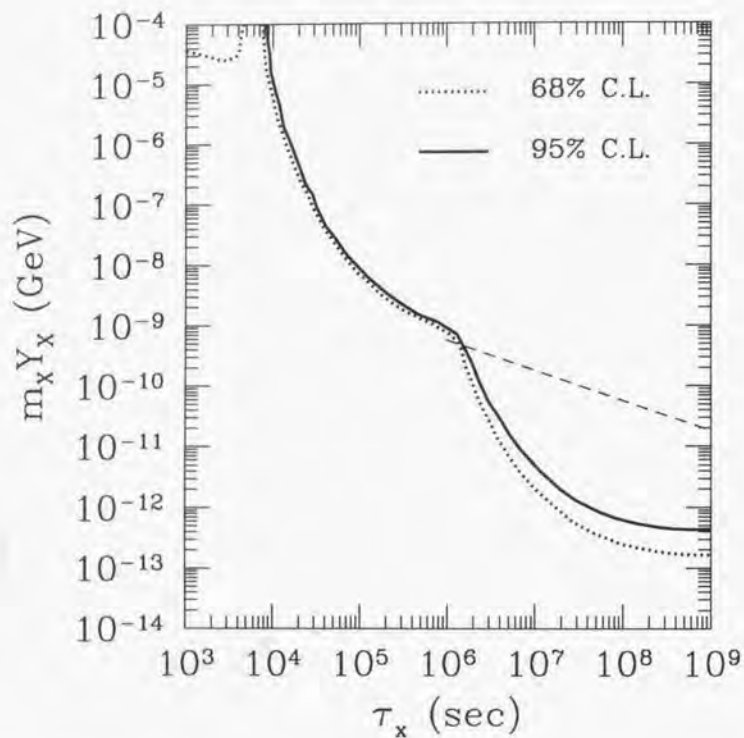


Figure 5.7: Contours of C.L. projected on  $\eta$  axis. The dotted line denotes the 68% C.L. and the solid line denotes the 95% C.L. The dashed line is the upper bound from the cosmic microwave background radiation which will be discussed in the next subsection.

lifetime longer than  $\sim 10^6$  sec [108], which is when the double Compton process ( $\gamma + e^- \rightleftharpoons \gamma + \gamma + e^-$ ) freezes out [109].<sup>1</sup> After this time, photon number is conserved, so photon injection from a radiatively decaying particle would cause the spectrum of the CMBR to become a Bose-Einstein distribution with a finite chemical potential  $\mu$ . COBE [30] observations give us the constraint  $|\mu| \lesssim 9.0 \times 10^{-5}$ . For small  $\mu$ , the ratio of the injected to total photon energy density is given by  $\delta\rho_\gamma/\rho_\gamma \sim 0.71\mu$ . Thus, we have the constraint

$$m_X Y_X \lesssim 6 \times 10^{-10} \text{GeV} \left( \frac{\tau_X}{10^6 \text{sec}} \right)^{-\frac{1}{2}} \quad \text{for } 10^6 \text{sec} \lesssim \tau_X \lesssim 4 \times 10^{10} \text{sec}. \quad (5.3)$$

In Fig. 5.7 we also plot the above upper bound. Note that the CMBR constraint is not as strong as the bounds we have obtained from BBN. In particular,  ${}^3\text{He}/\text{D}$  gives us our strongest constraint for lifetimes longer than  $10^6$  sec, because  ${}^3\text{He}$  photofission overproduces  ${}^3\text{He}$  [20].

In this thesis, we have considered only radiative decays; *i.e.*, decays to photons and invisible particles. If  $X$  decayed to charged leptons, the effects would be similar to those of the decay to photons, because charged leptons also generate electromagnetic cascades, resulting in many soft photons. On the other hand, if  $X$  decayed only to neutrinos, the constraints would become much weaker. In the minimal supersymmetric standard model (MSSM), the  $X$  particle would decay to neutrinos and sneutrinos. The emitted neutrinos would scatter off of background neutrinos, producing electron-positron pairs, which would trigger an electromagnetic cascade. Because the interaction between the emitted and background neutrinos is weak, the destruction of the light elements does not occur very efficiently [110]. In contrast, if  $X$  decayed to hadrons, we expect that our bounds would tighten, because hadronic showers could be a significant source of  $\text{D}$ ,  ${}^3\text{He}$ ,  ${}^6\text{Li}$ ,  ${}^7\text{Li}$ , and  ${}^7\text{Be}$  [93]. In fact, even though we have assumed that  $X$  decays only to photons, these photons may convert to hadrons. Thus, the branching ratio to hadrons is at least of order 1%, if kinematically allowed [56]. Since we have neglected this effect, our photodissociation bounds are conservative.

## 5.2 Models

So far, we have discussed general constraints from BBN on radiatively decaying particles. In the minimal standard model, there is no such particle. However, some extensions of the standard model naturally result in such exotic particles, and the light-element abundances may be significantly affected in these cases. In this section, we present several examples of such radiatively decaying particles, and discuss the constraints.

Our first example is the gravitino  $\psi$ , which appears in all the supergravity models. The gravitino is the superpartner of the graviton, and its interactions are suppressed by inverse

<sup>1</sup>This constraint applies only to particles with lifetime shorter than  $\sim 4 \times 10^{10}$  sec, which corresponds to the decoupling time of Compton/inverse Compton scattering. After this time, injected photons do not thermalize with the CMBR.

powers of the reduced Planck scale  $M_* \simeq 2.4 \times 10^{18}$  GeV. Because of this suppression, the lifetime of the gravitino is very long. Assuming that the gravitino's dominant decay mode is to a photon and its superpartner (the photino), the gravitino's lifetime is given by

$$\tau_{3/2} \simeq 4 \times 10^5 \text{ sec} \times (m_{3/2}/1 \text{ TeV})^{-3}, \quad (5.4)$$

where  $m_{3/2}$  is the gravitino mass. Notice that the gravitino mass is  $O(100 \text{ GeV} - 1 \text{ TeV})$  in a model with gravity-mediated supersymmetry (SUSY) breaking, resulting in a lifetime which may affect BBN.

If the gravitino is thermally produced in the early universe, and decays without being diluted, it completely spoils the success of SBBN. Usually, we solve this problem by introducing inflation, which dilutes away the primordial gravitinos. However, even with inflation, gravitinos are produced through scattering processes of thermal particles after reheating. The abundance  $Y_{3/2} = n_{3/2}/n_\gamma$  of the gravitino depends on the reheating temperature  $T_R$ , and is given by [97]

$$Y_{3/2} \simeq 3 \times 10^{-11} \times (T_R/10^{10} \text{ GeV}). \quad (5.5)$$

Therefore, if the reheating temperature is too high, then gravitinos are overproduced, and too many light nuclei are photodissociated.

We can transform our constraints on  $(\tau_X, m_X Y_X)$  into constraints on  $(m_{3/2}, T_R)$ . In particular, we use the projected 95% C.L. boundaries from Fig. 5.7. For several values of the gravitino mass, we read off the most conservative upper bound on the reheating temperature from Fig. 5.8, and the results are given by

$$\begin{aligned} m_{3/2} = 100 \text{ GeV} \quad (\tau_{3/2} \simeq 4 \times 10^8 \text{ sec}) & : T_R \lesssim 2 \times 10^6 \text{ GeV}, \\ m_{3/2} = 1 \text{ TeV} \quad (\tau_{3/2} \simeq 4 \times 10^5 \text{ sec}) & : T_R \lesssim 6 \times 10^8 \text{ GeV}, \\ m_{3/2} = 3 \text{ TeV} \quad (\tau_{3/2} \simeq 1 \times 10^4 \text{ sec}) & : T_R \lesssim 2 \times 10^{11} \text{ GeV}. \end{aligned}$$

If the gravitino is heavy enough ( $m_{3/2} \gtrsim 5 \text{ TeV}$ ), then its lifetime is too short to destroy even D. In this case, our only constraint is from the overproduction of  ${}^4\text{He}$ . If the gravitino mass is lighter, then the lifetime is long enough to destroy D,  ${}^3\text{He}$ , or even  ${}^4\text{He}$ . In this case, our constraint on the reheating temperature is more severe. For reference, we also show the plot in  $(m_{3/2}, n_{3/2}/s)$  plane where  $s$  denotes the entropy density.

Another example of our decaying particle is the lightest superparticle in the MSSM sector, if it is heavier than the gravitino. In particular, if the lightest neutralino is the lightest superparticle in the MSSM sector, then it can be a source of high-energy photons, since it will decay into a photon and a gravitino. In this case, we may use BBN to constrain the MSSM.

The abundance of the lightest neutralino is determined when it freezes out of the thermal

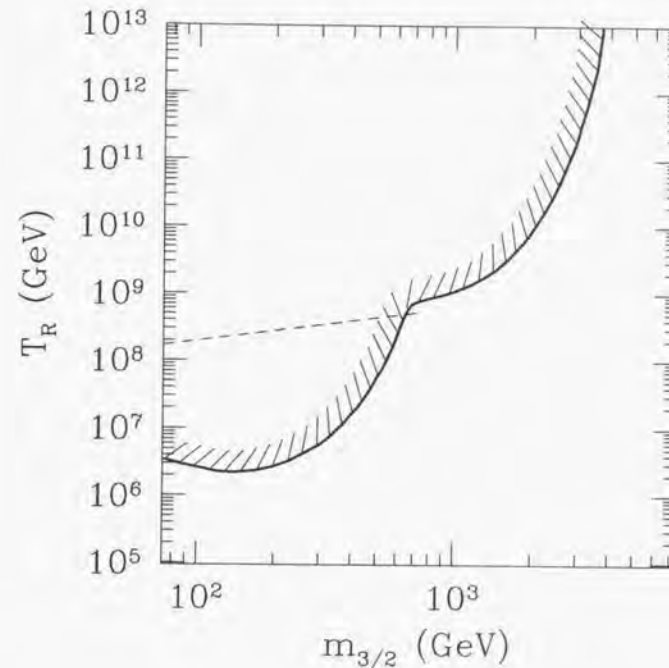


Figure 5.8: Contours of 95% C.L., yielding an upper bound on the reheating temperature, as a function of the gravitino mass. The dashed line denotes the upper bound from the observation of the cosmic microwave background, see Eq. (5.3).

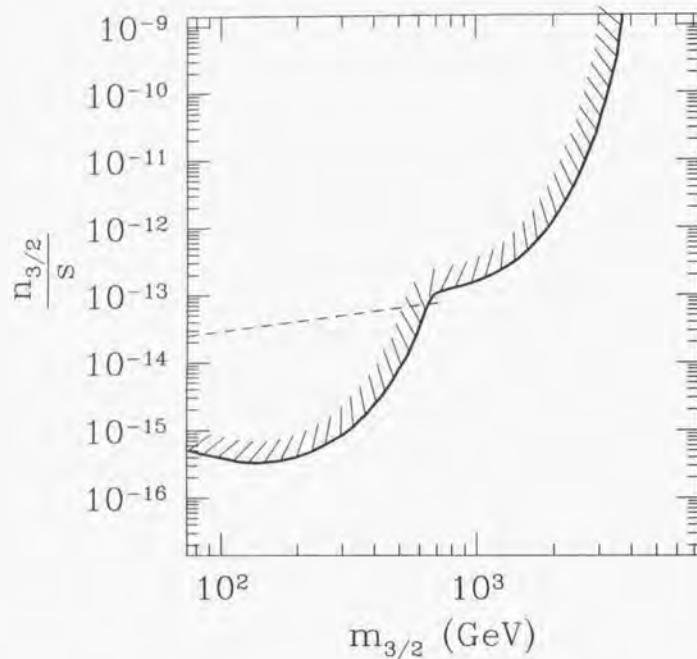


Figure 5.9: Contours of 95% C.L. in  $(m_{3/2}, n_{3/2}/s)$  plane. The dashed line denotes the upper bound from the observation of the cosmic microwave background, see Eq. (5.3).

bath. The abundance is a function of the masses of the superparticles, and it becomes larger as the superparticles get heavier. Thus, the upper bound on  $m_X Y_X$  can be translated into an upper bound on the mass scale of the superparticles.

In order to investigate this scenario, we consider the simplest case where the lightest neutralino is (almost) purely bino  $\tilde{B}$ . In this case, the lightest neutralino pair-annihilates through squark and slepton exchange. In particular, if the right-handed sleptons are the lightest sfermions, then the dominant annihilation is  $\tilde{B} + \tilde{B} \rightarrow l^+ + l^-$ . The annihilation cross section through this process is given by [111]

$$\langle \sigma v_{\text{rel}} \rangle = 8\pi\alpha_1^2 \langle v^2 \rangle \left\{ \frac{m_{\tilde{B}}^2}{(m_{\tilde{B}}^2 + m_{\tilde{l}_R}^2)^2} - \frac{2m_{\tilde{B}}^4}{(m_{\tilde{B}}^2 + m_{\tilde{l}_R}^2)^3} + \frac{2m_{\tilde{B}}^6}{(m_{\tilde{B}}^2 + m_{\tilde{l}_R}^2)^4} \right\}, \quad (5.6)$$

where  $\langle v^2 \rangle$  is the average velocity squared of bino, and we added the contributions from all three generations by assuming the right-handed sleptons are degenerate.<sup>2</sup> With this annihilation cross section, the Boltzmann equation for the number density of binos is given by

$$\dot{n}_{\tilde{B}} + 3Hn_{\tilde{B}} = -2\langle \sigma v_{\text{rel}} \rangle (n_{\tilde{B}}^2 - (n_{\tilde{B}}^{\text{EQ}})^2), \quad (5.7)$$

where  $n_{\tilde{B}}^{\text{EQ}}$  is the equilibrium number density of binos. The factor 2 is present because two binos annihilate into leptons in one collision. We solved this equation and obtained the mass density of the bino as a function of the bino mass and the right-handed slepton mass. (For details, see *e.g.* Ref. [54]). Numerically, for  $m_{\tilde{B}} = 100$  GeV,  $m_X Y_X$  ranges from  $\sim 10^{-9}$  GeV to  $\sim 10^{-5}$  GeV as we vary  $m_{\tilde{l}_R}$  from 100 GeV to 1 TeV. If  $m_X Y_X$  is in this range, BBN is significantly affected unless the lifetime of the bino is shorter than  $10^4 - 10^5$  sec (see Table 5.2). The lifetime of the bino is given by

$$\tau_{\tilde{B}} = \left[ \frac{1}{48\pi} \frac{m_{\tilde{B}}^5 \cos^2 \theta_W}{m_{3/2}^2 M_*^2} \right]^{-1} \simeq 7 \times 10^4 \text{ sec} \times \left( \frac{m_{\tilde{B}}}{100 \text{ GeV}} \right)^{-3} \left( \frac{m_{3/2}}{1 \text{ GeV}} \right)^2. \quad (5.8)$$

Notice that the lifetime becomes shorter as the gravitino mass decreases; hence, too much D and  ${}^7\text{Li}$  are destroyed if the gravitino mass is too large. Therefore, we can convert the constraints given in Fig. 5.7 into upper bounds on the gravitino mass. Since the abundance of the bino is an increasing function of the slepton mass  $m_{\tilde{l}_R}$ , the upper bound on the gravitino mass is more severe for larger slepton masses. For example, for  $m_{\tilde{B}} = 100$  GeV, the upper bound on the gravitino mass is shown in Fig. 5.8. At some representative values of the slepton mass, the constraint is given by

$$m_{\tilde{l}_R} = 100 \text{ GeV} \quad : \quad m_{3/2} \lesssim 1 \text{ GeV},$$

<sup>2</sup>If the bino is heavier than the top quark, then the *s*-wave contribution annihilating into top quarks becomes important. In this thesis, we do not consider this case.

$$\begin{aligned}
m_{\tilde{g}} = 300 \text{ GeV} & : m_{3/2} \lesssim 700 \text{ MeV}, \\
m_{\tilde{g}} = 1 \text{ TeV} & : m_{3/2} \lesssim 400 \text{ MeV}.
\end{aligned}$$

As expected, for a larger value of the slepton mass, the primordial abundance of the bino gets larger, and the upper bound on the gravitino mass becomes smaller.

Another interesting source of high-energy photons is a modulus field  $\phi$ . Such fields are predicted in string-inspired supergravity theories. A modulus field acquires mass from SUSY breaking, so we estimate its mass  $m_\phi$  to be of the same order as the gravitino mass (see for example [112]).

In the early universe, the mass of the modulus field is negligible compared to the expansion rate of the universe, so the modulus field may sit far from the minimum of its potential. Since the only scale parameter in supergravity is the Planck scale  $M_*$ , the initial amplitude  $\phi_0$  is naively expected to be of  $O(M_*)$ . However, this initial amplitude is too large; it leads to well-known problems such as matter domination and distortion of the CMBR. Here, we regard  $\phi_0$  as a free parameter and derive an upper bound on it.

Once the expansion rate becomes smaller than the mass of the modulus field, the modulus field starts oscillating. During this period, the energy density of  $\phi$  is proportional to  $R^{-3}$  (where  $R$  is the scale factor); hence, its energy density behaves like that of non-relativistic matter. The modulus eventually decays, when the expansion rate becomes comparable to its decay rate. Without entropy production from another source, the modulus density at the decay time is approximately

$$m_\phi Y_\phi = \frac{\rho_\phi}{n_\gamma} \sim 5 \times 10^{10} \text{ GeV} \times (m_\phi/1 \text{ TeV})^{1/2} (\phi_0/M_*)^2, \quad (5.9)$$

where  $\rho_\phi$  is the energy density of the modulus field. As in our other models, we can convert our constraints on  $(\tau_X, m_X Y_X)$  (Fig. 5.7) into constraints on  $(m_\phi, \phi_0)$ , see Fig. 5.11. Using the constraint, we still obtain very stringent bounds on the initial amplitude of the modulus field  $\phi_0$ :

$$\begin{aligned}
m_\phi = 100 \text{ GeV} \quad (\tau_\phi \sim 4 \times 10^8 \text{ sec}) & : \phi_0 \lesssim 1 \times 10^7 \text{ GeV}, \\
m_\phi = 1 \text{ TeV} \quad (\tau_\phi \sim 4 \times 10^5 \text{ sec}) & : \phi_0 \lesssim 5 \times 10^8 \text{ GeV}, \\
m_\phi = 3 \text{ TeV} \quad (\tau_\phi \sim 1 \times 10^4 \text{ sec}) & : \phi_0 \lesssim 9 \times 10^9 \text{ GeV}.
\end{aligned}$$

Clearly, our upper bound from BBN rules out our naive expectation that  $\phi_0 \sim M_*$ . It is important to notice that (conventional) inflation cannot solve this difficulty by diluting the coherent mode of the modulus field. This is because the expansion rate of the universe is usually much larger than the mass of the modulus field, and hence the modulus field does not start oscillation. One attractive solution is a thermal inflation model proposed by Lyth and Stewart [40]. In the thermal inflation model, a mini-inflation of about  $\sim 10$   $e$ -folds reduces the modulus density. Even if thermal inflation occurs, there may remain a significant

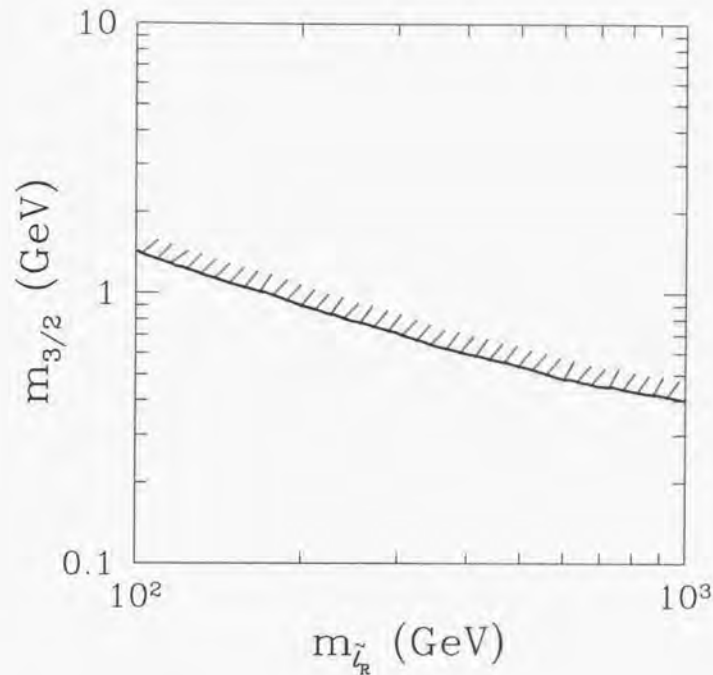


Figure 5.10: Contours of 95% C.L., yielding an upper bound on the gravitino mass, as a function of the right-handed slepton mass.

modulus energy density, which decays to high-energy photons. Thus, BBN gives a stringent constraint on the thermal inflation model.

### 5.3 The obtained constraints of the long-lived massive particles : summary

We have discussed the photodissociation of light elements due to the radiative decay of a massive particle, and we have shown how we can constrain our model parameters from the observed light-element abundances.

We have also discussed candidates for our radiatively decaying particle. Our first example is the gravitino. In this case, we can constrain the reheating temperature after inflation, because it determines the abundance of the gravitino. We obtained the stringent bounds  $T_R \lesssim 10^6 \text{ GeV} - 10^9 \text{ GeV}$  for  $100 \text{ GeV} \lesssim m_{3/2} \lesssim 1 \text{ TeV}$ .

Our second example is the lightest neutralino which is heavier than the gravitino. When the neutralino is the lightest superparticle in the MSSM sector, it can decay into a photon and a gravitino. If we assume the lightest neutralino is pure bino, and its mass is about  $100 \text{ GeV}$ , then the relic number density of binos is related to the right-handed slepton mass, because they annihilate mainly through right-handed slepton exchange. For this case, we obtained an upper bound on the gravitino mass:  $m_{3/2} \lesssim 400 \text{ MeV} - 1 \text{ GeV}$  for  $100 \text{ GeV} \lesssim m_{\tilde{l}_R} \lesssim 1 \text{ TeV}$ .

Our third example is a modulus field. We obtained a severe constraint on its initial amplitude,  $\phi_0 \lesssim 10^8 \text{ GeV} - 10^9 \text{ GeV}$  for  $100 \text{ GeV} \lesssim m_{3/2} \lesssim 1 \text{ TeV}$ . This bound is well below the Planck scale, so it suggests the need for a dilution mechanism, such as thermal inflation.

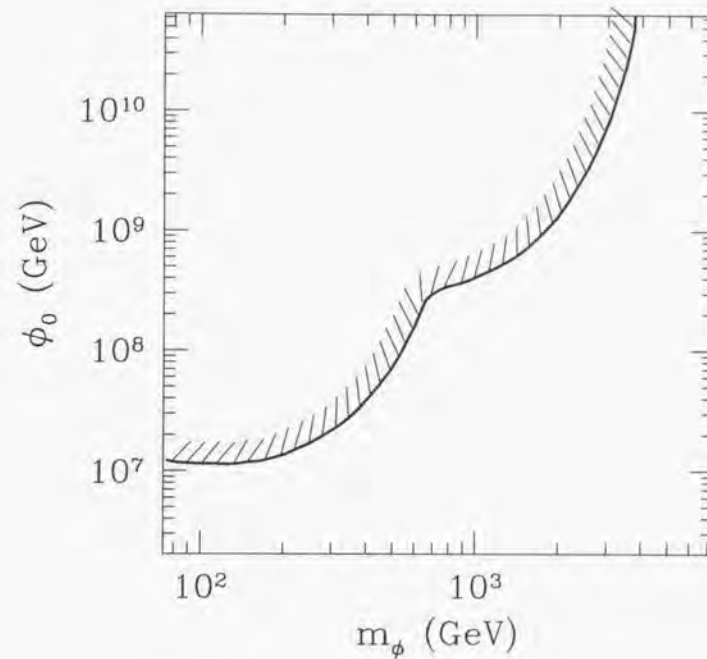


Figure 5.11: Contours of 95% C.L., yielding an upper bound on the initial amplitude of the modulus field as a function of the mass of the modulus field.

## Chapter 6

### Conclusion and Discussion

#### 6.1 Summary of conclusions

In this section we summarize the conclusions drawn in the above chapters. We have investigated the effects on BBN in the various particle injection scenarios, i) the late-time entropy production, ii) the evaporation of the primordial black holes, and iii) the decay of a massive particle after the BBN epoch.

In Chapter 3 we discussed the physical mechanism of the late-time entropy production due to the decay of massive particles before the BBN epoch. In this chapter we pointed out that if the large entropy is produced around the BBN epoch and replace the previous radiations, the background neutrinos are not thermalized well and they do not have the perfect Fermi-Dirac distribution functions. Then, the freeze-out value of  $n/p$  would be sensitively influenced and especially the produced  ${}^4\text{He}$  mass fraction would be drastically changed. Comparing with the observational abundances of the light elements, we have found that the reheating temperature after the entropy production should be higher than 0.7 MeV.

In addition if we consider the decay modes into the quarks or gluons, they immediately fragment into a lot of hadrons ( $\pi, K, n, p$ , etc.) and they induce the further significant effects on BBN. It would be unavoidable for the massive particle to have the net hadronic decay mode in the realistic models. The hadrons emitted at the beginning of the BBN epoch inter-convert the ambient proton and neutron each other. Then the proton which is richer than neutron at that time is extraordinarily changed into neutron and the freeze-out value of  $n/p$  becomes larger and the produced  ${}^4\text{He}$  increases more than SBBN. Observationally we can constrain the late-time hadron emission scenario and we have found the lower bound of the reheating temperature that,

$$T_R \gtrsim 2.5 - 4.0 \text{ MeV}, \quad (6.1)$$

at 95 % C.L. for the hadronic branching ratio  $B_h = 10^{-2} - 1$  and  $m_\phi = 10 \text{ GeV} - 100 \text{ TeV}$  which is the natural mass region for the supersymmetric particles. Namely Eq. (6.1) tells us that the entropy in the universe should be prepared early enough to success the BBN

( $\tau_\phi \lesssim (3-8) \times 10^{-2} \text{ sec}$ ). By the way, if we take the serious attitude to the "Moduli problem", we should consider a sort of the extra dilution mechanism, e.g. "thermal inflation" which dilutes the dangerous particles such as Moduli. In this model we should delicately treat the reheating process just before the BBN epoch and then the above constraint would give a useful indication.

In Chapter 4 we have discussed the evaporation of the PBHs and its effects on BBN. In the chapter we investigated a variety of the physical phenomena concerning the particle emissions from the PBHs and we pointed out that the hadron emission, which is naturally expected to occur within any models of the black holes, dominantly influences the standard big bang scenario and the light element abundances. Although some attempts concerning the hadron emission during the BBN epoch were done about twenty years ago, they discussed that the hadrons are directly emitted in the form of nucleons and mesons. It is surprising that since that time, such an old constraint of the PBH have been believed and referred for twenty years. In the chapter, we asserted that we should adopt the elementary particle picture, and rather hadrons should be emitted as quark-gluon jets primarily in the modern view of quantum chromodynamics (QCD). In this situation we entirely revised the old constraints. Then we obtained the constraint of the initial fraction of PBHs mass density,

$$\beta \lesssim 10^{-20} \quad (\text{for } 10^8 \text{ g} \lesssim M \lesssim 10^{10} \text{ g}) \quad (6.2)$$

$$\beta \lesssim 10^{-22} \quad (\text{for } 10^{10} \text{ g} \lesssim M \lesssim 3 \times 10^{10} \text{ g}). \quad (6.3)$$

The above upper bounds suggest the informations about the primordial density fluctuation on the small scales which was generated from the primordial inflation. It should be noted that only BBN can research such a small scale of the density fluctuation and there is no other method at present.

In Chapter 5 we have investigated the effects on BBN by the radiative decay of the long lived massive particles after the BBN epoch. Since the supergravity or superstring theory predicts such long lived particles and it is commonly regarded them as dangerous in BBN, it has been desired that we should clarify the problems in details. In the chapter we discussed the photo-dissociation of the light elements due to a lot of soft photons emitted by the decay of the massive particles. Especially when the candidate of the massive particles to which we pay attention is the gravitino, we obtain the upper bound of the reheating temperature after the primordial inflation not to produce more gravitinos by the thermal scattering,

$$T_R \lesssim 10^6 \text{ GeV} - 10^9 \text{ GeV} \quad \text{for } 100 \text{ GeV} \lesssim m_{3/2} \lesssim 1 \text{ TeV}. \quad (6.4)$$

The upper bounds strongly constrain the existing models of the inflation. If the latest entropy production were the reheating process after the primordial inflation, i.e. the present radiation were predominantly produced by the decay of the inflaton and the subsequent scatterings, the allowed reheating temperature should have been sandwiched between Eq. (6.1) and Eq. (6.4).

In that context, we could success to constrain the reheating temperature from both the lower and upper sides by applying the BBN to the high energy physics.

As we have explained in the above chapters, comparing with the precise observations, the theory of BBN is robust enough to search the early universe or the high energy physics beyond the SM. The method is very unique because it does not depend on the large experimental instruments such as colliders. We expect that when the further observations provide a lot of accurate data and they become available, we will more profoundly understand the elementary physics and how the nature is.

## Acknowledgments

The author wishes to express his sincere gratitude to M. Kawasaki for various discussions and suggestions. He also wishes to thank Naoshi Sugiyama, Jun'ichi Yokoyama, Takeo Moroi and Erich Holtmann who are his collaborators in the parts of this thesis. If there were not their help, this work would not be completed. He also thank Jiro Arafune and T. Asaka for their valuable discussions and useful comments. He appreciates Katsuhiko Sato and Yasushi Suto for their continuous encouragement. Finally he is also grateful to all the members of Theoretical Astrophysical Group in University of Tokyo, and all the members of Theoretical Group of Institute for Cosmic Ray Research in University of Tokyo for their various supports.

This work was partially supported by the Grant-in-Aid for Research Fellowship of the Japan Society for the Promotion of Science for Young Scientists.

## Appendix A

# Neutrino decoupling from the thermal bath

### A.1 Neutrino decoupling temperature

In this section we discuss the neutrino decoupling from the thermal bath on some simple assumptions in the standard big bang model. In the model it is assumed that the neutrinos had already been thermalized well in an earlier epoch. Therefore we obviously expect that they have the perfect Fermi-Dirac distribution functions around the BBN epoch.

When the ratio of the weak interaction rate  $\Gamma$  to the Hubble expansion rate  $H$  falls below unity, neutrinos depart from thermal equilibrium. Here we define the decoupling temperature  $T_D$  by  $\Gamma(T_D) = H(T_D)$ . In this situation we need to compute the inelastic weak interaction rate  $\Gamma$  precisely. The pair production process is represented by,

$$e^-(p_a) + e^+(p_b) \longleftrightarrow \nu_l(p_1) + \bar{\nu}_l(p_2), \quad (\text{A.1})$$

where  $p$  is the energy momentum four vector. The time evolution of the number density of the particle is described by the Integrated Boltzmann equations<sup>1</sup>. Here we use the method of pseudo-chemical potentials [48]. It is expressed by,

$$R^{-3} \frac{\partial}{\partial t} (R^3 n_e(t)) = (n_e^0(t)^2 - n_e(t)^2) \langle \sigma v_{rel} \rangle, \quad (\text{A.2})$$

where the subscript "0" denotes quantities in thermal equilibrium.  $v_{rel}$  is the relative velocity. In the equation we focus the electron and positron number density. The interaction rate is expressed by  $\Gamma = n_e(t) \langle \sigma v_{rel} \rangle$ , where  $n_e(t)$  is the number density of the background electrons. The thermal averaged cross section times relative velocity in the *center of mass system* (cms)

<sup>1</sup>As we discussed in Chapter 3, the integrated Boltzmann equations are applicable only for the particles which have the thermal distributions. If the particle is not thermalized in the non-standard scenario, we should use the momentum dependent Boltzmann equations.

is given by,

$$\langle \sigma v_{rel} \rangle = \frac{2g_e}{n_e^0(t)^2} \int d\bar{p}_a d\bar{p}_b f_a^0 f_b^0 d\bar{p}_1 d\bar{p}_2 (2\pi)^4 \delta^4(p_a + p_b - p_1 - p_2) |M|^2 [1 - g_1^0(E_1)] [1 - g_2^0(E_2)], \quad (\text{A.3})$$

where  $d\bar{p}_i = d\mathbf{p}_i / 2E_i (2\pi)^3$ ,  $M$  is the matrix amplitude.  $f_a(f_b)$  is the phase space distribution function for electron (positron) and  $g_1(g_2)$  for neutrino (anti-neutrino).

The phase space integration for neutrino and anti-neutrino is performed for  $T \gg m_\nu$  [113, 114, 115, 116, 117].

$$\begin{aligned} & \frac{1}{2E_a E_b} \int d\bar{p}_1 d\bar{p}_2 (2\pi)^4 \delta^4(p_a + p_b - p_1 - p_2) |M|^2 [1 - g_1^0(E_1)] [1 - g_2^0(E_2)] \\ &= \frac{2G_F^2}{3\pi} (c_1^2 + c_2^2) E_a E_b [1 - g_1^0(E/2)] [1 - g_2^0(E/2)], \end{aligned} \quad (\text{A.4})$$

where  $E = E_a + E_b$ ,  $G_F$  is the Fermi coupling constant, and  $c_1$  and  $c_2$  are given by,

$$c_1 = \frac{1}{2} + 2 \sin^2 \theta_W \quad \text{for } \nu_e, \quad (\text{A.5})$$

$$c_2 = \frac{1}{2} - 2 \sin^2 \theta_W \quad \text{for } \nu_\mu \text{ and } \nu_\tau, \quad (\text{A.6})$$

where  $\sin^2 \theta_W \simeq 0.231$  is Weinberg angle [32]. In this case, the scattering amplitude  $|M|^2$  for electron neutrino is larger than for  $\nu_\mu$  and  $\nu_\tau$  by  $\sim 4.66$  since the magnitude of the interaction of  $\nu_e$  is contributed by both the neutral current and the charged current interactions, while the magnitude of the interaction of  $\nu_\mu$  or  $\nu_\tau$  is contributed only by the neutral current interaction. Substituting Eq. (A.4) to Eq. (A.3), we obtain

$$\Gamma(T) = \frac{4(c_1^2 + c_2^2)}{9\pi^3 \zeta(3)} I_2 G_F^2 T^5, \quad (\text{A.7})$$

where  $\zeta(3) \simeq 1.202$  and the numerical factor  $I_2$  is given by,

$$\begin{aligned} I_2 &= \int_0^\infty \int_0^\infty dx dy \frac{x^3}{e^x + 1} \frac{y^3}{e^y + 1} \frac{e^{(x+y)/2}}{e^{(x+y)/2} + 1} \frac{e^{(x+y)/2}}{e^{(x+y)/2} + 1} \\ &\simeq 30.29, \end{aligned} \quad (\text{A.8})$$

Then we can estimate the neutrino decouple temperature as

$$T_D \simeq \frac{4.38}{(c_1^2 + c_2^2)^{1/3}} (\sqrt{g_*})^{1/3}, \quad (\text{A.9})$$

where  $g_* \simeq 10.75$ . Concretely, we find the weak interaction rate  $\Gamma$  for each neutrino species,

$$\Gamma \simeq 0.420 G_F^2 T^5, \quad \text{for } \nu_e, \quad (\text{A.10})$$

$$\Gamma \simeq 0.091 G_F^2 T^5, \quad \text{for } \nu_\mu \text{ and } \nu_\tau, \quad (\text{A.11})$$

and approximately the each decouple temperature is obtained by [113]

$$T_D \simeq 1.98 \text{ MeV} \quad \text{for } \nu_e, \quad (\text{A.12})$$

$$T_D \simeq 3.30 \text{ MeV} \quad \text{for } \nu_\mu \text{ and } \nu_\tau. \quad (\text{A.13})$$

As mentioned above, since the magnitude of interaction rate for  $\nu_e$  is larger than for  $\nu_\mu$  and  $\nu_\tau$  due to the electron background, the reaction which maintains  $\nu_e$  in thermal equilibrium continues later and the decouple temperature of  $\nu_e$  is lower than  $\nu_\mu$  and  $\nu_\tau$ .

## Appendix B

### Boltzmann equation for neutrino distribution functions

#### B.1 Reduction of collision integral

This appendix shows how we can reduce the nine dimensional integrals in Eq. (3.6) of the collision term  $C_{i,\text{scat}}$  for the scattering process into one dimensional integrals. Notice that, since we treat the massless neutrino, the norm of the neutrino momentum equals to its energy  $|\mathbf{p}_i| = E_i$ . Here we divide the collision term into two parts:

$$C_{i,\text{scat}} = -F + B, \quad (\text{B.1})$$

where  $F$  represents the forward process and  $B$  represents the backward process. They are given by

$$F = \frac{g_e}{2E_1} \int \frac{d^3p_2}{2E_2(2\pi)^3} \int \frac{d^3p_3}{2E_3(2\pi)^3} \int \frac{d^3p_4}{2E_4(2\pi)^3} (2\pi)^4 \delta^4(p_1 + p_2 - p_3 - p_4) S|M|^2 \Lambda_F, \quad (\text{B.2})$$

$$B = \frac{g_e}{2E_1} \int \frac{d^3p_2}{2E_2(2\pi)^3} \int \frac{d^3p_3}{2E_3(2\pi)^3} \int \frac{d^3p_4}{2E_4(2\pi)^3} (2\pi)^4 \delta^4(p_1 + p_2 - p_3 - p_4) S|M|^2 \Lambda_B, \quad (\text{B.3})$$

where  $g_e = 2$  and the phase space factors are given by

$$\Lambda_F = f_1(E_1) f_2(E_2) (1 - f_3(E_3)) (1 - f_4(E_4)), \quad (\text{B.4})$$

$$\Lambda_B = (1 - f_1(E_1)) (1 - f_2(E_2)) f_3(E_3) f_4(E_4). \quad (\text{B.5})$$

The integral over  $d^3p_4$  is immediately done using  $\delta^3(\mathbf{p}_1 + \mathbf{p}_2 - \mathbf{p}_3 - \mathbf{p}_4)$ . From the momentum conservation,  $|\mathbf{p}_4|$  is given by

$$|\mathbf{p}_4|^2 = E_4^2 = E_2^2 + 2E_2 R \cos \eta + R^2, \quad (\text{B.6})$$

where  $\mathbf{R} \equiv \mathbf{p}_1 - \mathbf{p}_3$ ,  $R = |\mathbf{R}|$  and  $\cos \eta \equiv \mathbf{R} \cdot \mathbf{p}_2 / (|\mathbf{p}_2| R)$ .

The remaining delta function  $\delta(E_1 + E_2 - E_3 - E_4)$  shows the energy conservation law

which is given by

$$E_4^2 = E_1^2 + E_2^2 + E_3^2 + 2(E_1E_2 - E_1E_3 - E_2E_3). \quad (\text{B.7})$$

We can generally take the momentum axes as

$$\mathbf{R} = (0, 0, R) \quad (\text{B.8})$$

$$\mathbf{p}_2 = (E_2 \sin \eta \sin \phi, E_2 \sin \eta \cos \phi, E_2 \cos \eta), \quad (\text{B.9})$$

$$\mathbf{p}_3 = (E_3 \sin \xi, 0, E_3 \sin \xi), \quad (\text{B.10})$$

where

$$\cos \xi = \frac{E_1^2 - E_3^2 - R^2}{2E_3R}. \quad (\text{B.11})$$

Then  $|\cos \xi| \leq 1$  demands

$$|E_1 - E_3| \leq R \leq E_1 + E_3. \quad (\text{B.12})$$

The volume element of  $\mathbf{p}_2$  is given by  $dp_2^3 = E_2^2 d\cos \eta d\phi$  and from Eqs. (B.6) and (B.7) the azimuthal angle is obtained by

$$\cos \eta = -\frac{R^2 - (E_1 - E_3)^2 - 2E_2(E_1 - E_3)}{2E_2R}. \quad (\text{B.13})$$

Then  $|\cos \eta| \leq 1$  demands

$$|E_1 - E_3| \leq R \leq E_1 + 2E_2 - E_3. \quad (\text{B.14})$$

From Eqs. (B.12) and (B.14), we can obtain the allowed region of R,

$$|E_1 - E_3| \leq R \leq \text{Inf}[E_1 + E_3, E_1 + 2E_2 - E_3]. \quad (\text{B.15})$$

Since the volume element of  $\mathbf{p}_3$  is given by  $dp_3^2 = 2\pi E_3^2 dE_3 d\cos \theta$  where  $\cos \theta = \mathbf{p}_1 \cdot \mathbf{p}_3 / (E_3 E_1)$ , the differential angle element is evaluated by

$$d\cos \theta = -\frac{R}{2E_1E_3} dR. \quad (\text{B.16})$$

From Eq. (B.15) we can see that the integration can be performed in the four allowed intervals,

$$\begin{aligned} -F + B &= \frac{1}{128E_1^2} \int_0^\infty dE_3 \int_0^\infty dE_2 \int dR \int_0^{2\pi} \frac{d\phi}{2\pi} |M|^2 (-\Lambda_F + \Lambda_B) \\ &= \frac{1}{128E_1^2} \left[ \int_0^{E_1} dE_3 \int_0^{E_3} dE_2 \int_{E_1-E_3}^{E_1+2E_2-E_3} dR + \int_0^{E_1} dE_3 \int_{E_3}^\infty dE_2 \int_{E_1-E_3}^{E_1+E_3} dR \right. \\ &\quad \left. + \int_{E_1}^\infty dE_3 \int_{-E_1+E_3}^{E_3} dE_2 \int_{-E_1+E_3}^{E_1+2E_2-E_3} dR + \int_{E_1}^\infty dE_3 \int_{E_3}^\infty dE_2 \int_{-E_1+E_3}^{E_1+E_3} dR \right] \end{aligned}$$

$$\times \int_0^{2\pi} \frac{d\phi}{2\pi} S|M|^2 (-\Lambda_F + \Lambda_B). \quad (\text{B.17})$$

Even though we only show the case of of  $\nu_e$  here, we can get the same procedure for  $\nu_\mu$  and  $\nu_\tau$  if  $C_V$  and  $C_A$  are replaced by  $\tilde{C}_V$  and  $\tilde{C}_A$ . As we also noted in Sec 3.2, we assume that electrons obey the Boltzmann distribution function  $e^{-E/T}$ . In addition, since neutrinos are massless, the energy momentum conservation gives  $p_1 \cdot p_1 = p_2 \cdot p_3$  in the elastic scattering process. The above assumptions simplify the integrations still more.

For the forward reaction,  $\nu(p_1) + e^\pm(p_2) \rightarrow \nu(p_3) + e^\pm(p_4)$ , the phase space factor is given by

$$\Lambda_F = f_\nu(E_1) (1 - f_\nu(E_3)) \exp\left[-\frac{E_2}{T}\right]. \quad (\text{B.18})$$

Then  $F_1$  and  $F_2$  in Eq. (3.12) are analytically estimated as

$$\begin{aligned} F_1 &\equiv \left[ \int_0^{E_3} dE_2 \int_{E_1-E_3}^{E_1+2E_2-E_3} dR + \int_{E_3}^\infty dE_2 \int_{E_1-E_3}^{E_1+E_3} dR \right] \int_0^{2\pi} \frac{d\phi}{2\pi} \cdot \frac{S|M|^2 e^{-\frac{E_2}{T}}}{256(C_V^2 + C_A^2)G_F^2} \\ &= 2T^4 [E_1^2 + E_3^2 + 2T(E_1 - E_3) + 4T^4] - T^2 [E_1^2 E_3^2 + 2E_1 E_3 (E_1 + E_3)T \\ &\quad + 2(E_1 + E_3)^2 T^2 + 4(E_1 + E_3)T^3 + 8T^4] e^{-\frac{E_1}{T}}. \quad (\text{B.19}) \end{aligned}$$

$$\begin{aligned} F_2 &\equiv \left[ \int_{-E_1+E_3}^{E_3} dE_2 \int_{-E_1+E_3}^{E_1+2E_2-E_3} dR + \int_{E_3}^\infty dE_2 \int_{-E_1+E_3}^{E_1+E_3} dR \right] \int_0^{2\pi} \frac{d\phi}{2\pi} \cdot \frac{S|M|^2 e^{-\frac{E_2}{T}}}{256(C_V^2 + C_A^2)G_F^2} \\ &= 2T^4 (E_1^2 + E_3^2 - 2T(E_1 - E_3) + 4T^4) e^{-\frac{E_1-E_3}{T}} - T^2 [E_1^2 E_3^2 + 2E_1 E_3 (E_1 + E_3)T \\ &\quad + 2(E_1 + E_3)^2 T^2 + 4(E_1 + E_3)T^3 + 8T^4] e^{-\frac{E_1}{T}}. \quad (\text{B.20}) \end{aligned}$$

On the other hand, for the backward reaction,  $\nu(p_1) + e^\pm(p_2) \leftarrow \nu(p_3) + e^\pm(p_4)$ , the phase space factor is given by,

$$\Lambda_B = (1 - f_\nu(E_1)) f_\nu(E_3) \exp\left(-\frac{E_1 + E_2 + E_3}{T}\right). \quad (\text{B.21})$$

Then we can analytically obtain  $B_1$  and  $B_2$  in Eq. (3.12) as

$$\begin{aligned} B_1 &\equiv \left[ \int_0^{E_3} dE_2 \int_{E_1-E_3}^{E_1+2E_2-E_3} dR + \int_{E_3}^\infty dE_2 \int_{E_1-E_3}^{E_1+E_3} dR \right] \int_0^{2\pi} \frac{d\phi}{2\pi} \cdot \frac{S|M|^2 e^{-\frac{E_1+E_2+E_3}{T}}}{256(C_V^2 + C_A^2)G_F^2} \\ &= 2T^4 (E_1^2 + E_3^2 + 2T(E_1 - E_3) + 4T^4) e^{-\frac{E_1-E_3}{T}} - T^2 [E_1^2 E_3^2 + 2E_1 E_3 (E_1 + E_3)T \\ &\quad + 2(E_1 + E_3)^2 T^2 + 4(E_1 + E_3)T^3 + 8T^4] e^{-\frac{E_1}{T}}, \quad (\text{B.22}) \end{aligned}$$

$$B_2 \equiv \left[ \int_{-E_1+E_3}^{E_3} dE_2 \int_{-E_1+E_3}^{E_1+2E_2-E_3} dR + \int_{E_3}^\infty dE_2 \int_{-E_1+E_3}^{E_1+E_3} dR \right] \int_0^{2\pi} \frac{d\phi}{2\pi} \cdot \frac{S|M|^2 e^{-\frac{E_1+E_2+E_3}{T}}}{256(C_V^2 + C_A^2)G_F^2}$$

$$= 2T^3 (E_1^2 + E_3^2 - 2T(E_1 - E_3) + 4T^4) - T^2 [E_1^2 E_3^2 + 2E_1 E_3 (E_1 + E_3)T + 2(E_1 + E_3)^2 T^2 + 4(E_1 + E_3)T^3 + 8T^4] e^{-\frac{E_1}{T}}, \quad (\text{B.23})$$

## Appendix C

### Method of Maximal Likelihood Analysis

#### C.1 $\chi^2$ Fitting in SBBN and SBBN+X

In this section, we explain how we answer the question, "How well does our simulation of BBN agree with the observed light-element abundances?" To be more precise, we rephrase the question as, "At what confidence level is our simulation of BBN excluded by the observed light-element abundances?"

From our Monte-Carlo BBN simulation, we obtain the theoretical probability density function (p.d.f.)  $p_{247}^{th}(y_2^{th}, Y^{th}, \log_{10} y_7^{th})$  of our simulated light-element abundances  $y_2^{th}$ ,  $Y^{th}$ , and  $\log_{10} y_7^{th}$ . We find that  $p_{247}^{th}(y_2^{th}, Y^{th}, \log_{10} y_7^{th})$  is well-approximated by a multivariate Gaussian distribution function:

$$p_{247}^{th}(y_2^{th}, Y^{th}, \log_{10} y_7^{th}) = p_2^{Gauss}(y_2^{th}) \times p_4^{Gauss}(Y^{th}) \times p_7^{Gauss}(\log_{10} y_7^{th}), \quad (\text{C.1})$$

where

$$p^{Gauss}(x; \bar{x}, \sigma) = \frac{1}{\sqrt{2\pi}\sigma} \exp\left[-\frac{1}{2}\left(\frac{x - \bar{x}}{\sigma}\right)^2\right]. \quad (\text{C.2})$$

Note that  $p_{247}^{th}(y_2^{th}, Y^{th}, \log_{10} y_7^{th})$  depends upon the parameters  $\mathbf{p} = (\eta, \dots)$  of our theory. (The ellipses refer to parameters in non-standard BBN, e.g.,  $m_X Y_X$ ,  $\tau_X$ .) In particular, the means and standard deviations of  $p_{247}^{th}(y_2^{th}, Y^{th}, \log_{10} y_7^{th})$  are functions of  $\mathbf{p}$ .

For BBN with a radiatively decaying particle, we also consider the ratio  $r^{th} = y_3^{th}/y_2^{th}$ . Our Monte-Carlo BBN simulation allows us to find the p.d.f.  $p_{23}^{th}(r^{th})$ . We approximate  $p_{23}^{th}$  by a Gaussian, and neglect the correlation between  $r$  and  $y_2^{th}, Y^{th}, \log_{10} y_7^{th}$ . This assumption allows us to write

$$p_{2347}^{th}(y_2^{th}, Y^{th}, r^{th}, \log_{10} y_7^{th}; \mathbf{p}) = p_{23}^{th}(r^{th}; \mathbf{p}) \times p_{247}^{th}(y_2^{th}, Y^{th}, \log_{10} y_7^{th}; \mathbf{p}). \quad (\text{C.3})$$

We want to compare these theoretical calculations to the observed light-element abun-

dances  $y_2^{obs}$ ,  $Y^{obs}$ , and  $\log_{10} y_7^{obs}$ . Since the observations of the light-element abundances are independent, we can factor the p.d.f.  $p_{247}^{obs}(y_2^{obs}, Y^{obs}, \log_{10} y_7^{obs})$  as

$$p_{247}^{obs}(y_2^{obs}, Y^{obs}, \log_{10} y_7^{obs}) = p_2^{obs}(y_2^{obs}) \times p_Y^{obs}(Y^{obs}) \times p_7^{obs}(\log_{10} y_7^{obs}). \quad (C.4)$$

We assume Gaussian p.d.f.'s for  $y_2^{obs}$ ,  $Y^{obs}$ , and  $\log_{10} y_7^{obs}$ . We use the mean abundances and standard deviations given in Equations (2.6), (2.9), and (2.10). Since we have two discordant values of  ${}^4\text{He}$ , we considered two cases, *i.e.*, high and low values of  ${}^4\text{He}$  abundances.

${}^3\text{He}$  is more complicated. Aside from the trivial positivity requirement, we only have an upper bound on  $r^{obs}$  (the primordial  ${}^3\text{He}/\text{D}$ , as deduced from solar-system observations); namely,  $r^{obs} < r_{\odot}$ . Because of this, we choose for the p.d.f.

$$p_{23}^{obs}(r^{obs}) = \begin{cases} 0 & , r^{obs} < 0 \\ N & , 0 < r^{obs} < \bar{r}_{\odot} \\ N \exp\left(-\frac{1}{2}\left(\frac{r^{obs}-\bar{r}_{\odot}}{\sigma_{r_{\odot}}}\right)^2\right) & , \bar{r}_{\odot} < r^{obs} \end{cases} \quad (C.5)$$

where the normalization factor is  $N = 1/(\bar{r}_{\odot} + \sigma_{r_{\odot}}\sqrt{\pi/2})$ , and  $\bar{r}_{\odot}$ ,  $\sigma_{r_{\odot}}$  are given in Eq. (2.7).

Since the observations of the light-element abundances are independent, we can write the total observational p.d.f. for BBN+ $X$  as

$$p_{2347}^{obs}(y_2^{obs}, Y^{obs}, r^{obs}, \log_{10} y_7^{obs}) = p_{23}^{obs}(r^{obs}) \times p_{247}^{obs}(y_2^{obs}, Y^{obs}, \log_{10} y_7^{obs}). \quad (C.6)$$

To simplify the notation, we write

$$\mathbf{a}^{th} = (y_2^{th}, Y^{th}, r^{th}, \log_{10} y_7^{th}) \quad (C.7)$$

$$\mathbf{a}^{obs} = (y_2^{obs}, Y^{obs}, r^{obs}, \log_{10} y_7^{obs}) \quad (C.8)$$

$$\mathbf{b}^{th} = (y_2^{th}, Y^{th}, \log_{10} y_7^{th}) \quad (C.9)$$

$$\mathbf{b}^{obs} = (y_2^{obs}, Y^{obs}, \log_{10} y_7^{obs}). \quad (C.10)$$

Then the quantities  $\Delta\mathbf{a} = \mathbf{a}^{th} - \mathbf{a}^{obs}$  have a p.d.f. given by:

$$\begin{aligned} p_{247}^{\Delta}(\Delta\mathbf{b}) &= \int d\mathbf{b}^{obs} p_{247}^{obs}(\mathbf{b}^{obs}) \int d\mathbf{b}^{th} p_{247}^{th}(\mathbf{b}^{th}) \delta(\Delta\mathbf{b} - (\mathbf{b}^{th} - \mathbf{b}^{obs})) \\ &= \int d\mathbf{b} p_{247}^{th}(\mathbf{b}) p_{247}^{obs}(\mathbf{b} - \Delta\mathbf{b}), \quad [\text{SBBN}] \end{aligned} \quad (C.11)$$

$$\begin{aligned} p_{2347}^{\Delta}(\Delta\mathbf{a}) &= \int d\mathbf{a}^{obs} p_{2347}^{obs}(\mathbf{a}^{obs}) \int d\mathbf{a}^{th} p_{2347}^{th}(\mathbf{a}^{th}) \delta(\Delta\mathbf{a} - (\mathbf{a}^{th} - \mathbf{a}^{obs})) \\ &= \int d\mathbf{a} p_{2347}^{th}(\mathbf{a}) p_{2347}^{obs}(\mathbf{a} - \Delta\mathbf{a}), \quad [\text{BBN}+X] \end{aligned} \quad (C.12)$$

where we have suppressed the dependence of  $p_{247}^{\Delta}(\Delta\mathbf{b})$ ,  $p_{247}^{th}(\mathbf{b}^{th})$ ,  $p_{2347}^{\Delta}(\Delta\mathbf{a})$ , and  $p_{2347}^{th}(\mathbf{a}^{th})$

on the theory parameters  $\mathbf{p}$ . The integral in Eq. (C.11) is simply a Gaussian:

$$p_{247}^{\Delta}(\Delta\mathbf{b}) = \prod_{i=2,4,7} \frac{1}{\sqrt{2\pi}\sigma_i} \exp\left[-\frac{1}{2}\left(\frac{\Delta b_i - \bar{\Delta b}_i}{\sigma_i^2}\right)^2\right], \quad (C.13)$$

where  $\bar{\Delta b}_i = \bar{b}_i^{th} - \bar{b}_i^{obs}$ ,  $\sigma_i^2 = (\sigma_i^{th})^2 + (\sigma_i^{obs})^2$ , and  $i$  runs over  $y_2$ ,  $Y$  and  $\log_{10} y_7$ . To evaluate Eq. (C.12), we note that

$$p_{2347}^{obs}(\mathbf{a}^{obs}) = p_{23}(r^{obs}) \times p_{247}^{obs}(\mathbf{b}^{obs}) \quad (C.14)$$

$$p_{2347}^{th}(\mathbf{a}^{th}) = p_{23}(r^{th}) \times p_{247}^{th}(\mathbf{b}^{th}), \quad (C.15)$$

where  $p_{247}^{obs}$  and  $p_{247}^{th}$  are Gaussian. The integral then factors as

$$p_{2347}^{\Delta}(\Delta\mathbf{a}) = \int dr p_{23}^{th}(r) p_{23}^{obs}(r - \Delta r) \times \int d\mathbf{b} p_{247}^{th}(\mathbf{b}) p_{247}^{obs}(\mathbf{b} - \Delta\mathbf{b}) \quad (C.16)$$

$$= p_{23}^{\Delta}(\Delta r) \times p_{247}^{\Delta}(\Delta\mathbf{b}). \quad (C.17)$$

The first integral can be evaluated as

$$p_{23}^{\Delta}(\Delta r) = \int_{-\infty}^{\infty} dr p_{23}^{th}(r + \Delta r) p_{23}^{obs}(r) \quad (C.18)$$

$$\begin{aligned} &= \int_0^{\bar{r}_{\odot}} dr \frac{N}{\sqrt{2\pi}\sigma_r^{th}} \exp\left[-\frac{1}{2}\left(\frac{r + \Delta r - \bar{r}^{th}}{\sigma_r^{th}}\right)^2\right] \\ &+ \int_{\bar{r}_{\odot}}^{\infty} dr \frac{N}{\sqrt{2\pi}\sigma_r^{th}} \exp\left(-\frac{1}{2}\left[\left(\frac{r + \Delta r - \bar{r}^{th}}{\sigma_r^{th}}\right)^2 + \left(\frac{r - \bar{r}_{\odot}}{\sigma_{r_{\odot}}}\right)^2\right]\right) \end{aligned} \quad (C.19)$$

$$\begin{aligned} &= \frac{N}{2} \left[ \text{erf}\left(\frac{\Delta r + \bar{r}_{\odot} - \bar{r}^{th}}{\sqrt{2}\sigma_r^{th}}\right) - \text{erf}\left(\frac{\Delta r - \bar{r}^{th}}{\sqrt{2}\sigma_r^{th}}\right) \right] \\ &+ \frac{N\sigma_{r_{\odot}}}{2\sigma_r} \left[ 1 - \text{erf}\left(\frac{\sigma_{r_{\odot}}(\Delta r - \bar{r}^{th} + \bar{r}_{\odot})}{\sqrt{2}\sigma_r^{th}\sigma_r}\right) \right] \exp\left[-\left(\frac{\Delta r - \bar{r}^{th} + \bar{r}_{\odot}}{\sqrt{2}\sigma_r}\right)^2\right] \end{aligned} \quad (C.20)$$

where  $\sigma_r^2 = (\sigma_r^{th})^2 + (\sigma_{r_{\odot}})^2$ . Since the above error function is defined by,

$$\text{erf}(x) \equiv \frac{2}{\sqrt{\pi}} \int_0^x \exp[-t^2] dt \quad \text{for } [-\infty \leq x \leq \infty], \quad (C.21)$$

the function can become the negative value when the argument is negative.

Our question can now be rephrased as, "At what confidence level is  $\Delta\mathbf{a} = 0$  excluded?" To answer this, we need to consider the region  $S$  in abundance space where the value of the p.d.f. is higher than

$$\bar{p} = \begin{cases} p_{247}^{\Delta}(\Delta\mathbf{b} = 0; \mathbf{p}) & [\text{SBBN}] \\ p_{2347}^{\Delta}(\Delta\mathbf{a} = 0; \mathbf{p}) & [\text{BBN}+X] \end{cases} \quad (C.22)$$

Mathematically phrased,

$$\text{C.L.}(\mathbf{p}) = \int_S d(\Delta\mathbf{b}) p_{247}^{\Delta}(\Delta\mathbf{b}; \mathbf{p}), \quad [\text{SBBN}] \quad (\text{C.23})$$

$$\text{C.L.}(\mathbf{p}) = \int_S d(\Delta\mathbf{a}) p_{2347}^{\Delta}(\Delta\mathbf{a}; \mathbf{p}), \quad [\text{BBN}+X] \quad (\text{C.24})$$

where

$$S = \{\Delta\mathbf{b} : p_{247}^{\Delta}(\Delta\mathbf{b}; \mathbf{p}) > \bar{p}\}, \quad [\text{SBBN}], \quad (\text{C.25})$$

$$S = \{\Delta\mathbf{a} : p_{2347}^{\Delta}(\Delta\mathbf{a}; \mathbf{p}) > \bar{p}\}, \quad [\text{BBN}+X]. \quad (\text{C.26})$$

We use the C.L. to constrain various scenarios of BBN.

In the SBBN case, the integral is Gaussian and is easily expressed in terms of  $\chi^2 = -2 \log[(2\pi)^{3/2} \sigma_2 \sigma_4 \sigma_7 \bar{p}]$  (See Eqs. (2.63) and (2.65)):

$$\text{C.L.}(\mathbf{p}) = -\sqrt{\frac{2\chi^2}{\pi}} \exp\left(-\frac{\chi^2}{2}\right) + \text{erf}\left(\sqrt{\frac{\chi^2}{2}}\right), \quad [\text{SBBN}]. \quad (\text{C.27})$$

To evaluate the BBN+X integral Eq. (C.24), we separate the Gaussian variables  $\Delta\mathbf{b}$  from the non-Gaussian variable  $\Delta r$ , using the decomposition in Eq. (C.16):

$$\text{C.L.}(\mathbf{p}) = \int_{S_{23}} d(\Delta r) p_{23}^{\Delta}(\Delta r) \int_{S_{247}(\Delta r)} d(\Delta\mathbf{b}) p_{247}^{\Delta}(\Delta\mathbf{b}), \quad (\text{C.28})$$

where  $S_{23}$  = the set of  $\Delta r$  such that  $p_{23}^{\Delta}(\Delta r) \geq \bar{p}/\max(p_{247})$ ; and  $S_{247}(\Delta r)$  = the set of  $\Delta\mathbf{b}$  such that  $p_{247}^{\Delta}(\Delta\mathbf{b}) \geq \bar{p}/p_{23}^{\Delta}(\Delta r)$ . We can easily evaluate the Gaussian integral. Again, the result is conveniently expressed in terms of  $\chi^2$ .

$$\text{C.L.}(\mathbf{p}) = \int_{S_{23}} d(\Delta r) p_{23}^{\Delta}(\Delta r) \left[ -\sqrt{\frac{2}{\pi}} \chi(\Delta r) e^{-\chi^2(\Delta r)/2} + \text{erf}\left(\frac{\chi(\Delta r)}{\sqrt{2}}\right) \right], \quad (\text{C.29})$$

where  $\chi(\Delta r) = \sqrt{2 \log[p_{23}^{\Delta}(\Delta r)/\{(2\pi)^{3/2} \sigma_2 \sigma_4 \sigma_7 \bar{p}\}]}$ . We then evaluate Eq. (C.29) numerically.

Our confidence level is calculated for four degrees of freedom  $\Delta a_i$  (three, in the case of SBBN). It denotes our certainty that a given point  $\mathbf{p}$  in the parameter space of the theory is excluded by the observed abundances. In order to compare our theory with a late-decaying particle (three parameters  $\mathbf{p}$ :  $\tau_X$ ,  $m_X Y_X$ , and  $\eta$ ) to a theory with a different number of parameters (*e.g.*, only one in SBBN), one would want to use a  $\chi^2$  variable in these parameters. This transformation would be possible if the abundances  $a_i$  were linear in the theory parameters  $\mathbf{p}$ . In this case, we could integrate out a theory parameter such as  $\eta$  and set a C.L. exclusion limit (with a reduced number of degrees of freedom) on the remaining parameters. However, the  $a_i$  turn out to be highly non-linear functions of  $\mathbf{p}$ , so integrating out a theory parameter turns out to have little meaning. Instead, we project out various

theory parameters (as explained in Section 5.1.3) to present our results as graphs.

## Bibliography

- [1] E. Hubble, *The realm of the nebulae*, Dover, p114 (1930).
- [2] A. A. Penzias and R. W. Wilson, *Astrophys. J.* **142** (1965) 419.
- [3] R. A. Alpher, H. Bethe and G. Gamow, *Phys. Rev.* **73** (1948) 803.
- [4] S. Weinberg, *Phys. Rev. Lett.* **19**, 1264 (1967);  
A. Salam, in *Elementary Particle Theory*, N. Svartholm, ed. (Almqvist and Wiksells, Stockholm, 1969), p. 367;  
S.L. Glashow, J. Iliopoulos, and L. Maiani *Phys. Rev.* **D2**, 1285 (1970).
- [5] C. Caso *et al.*, *Euro. Phys. J. C* **3**, 90 (1998) and references therein; see for the recent review, A. Sirlin, hep-ph/9912227.
- [6] G. 't Hooft and M. Veltman, *Nucl. Phys.* **B44**, 189 (1972); C.G. Bollini and J.J. Giambiagi, *Nuovo Cimento* **12B**, 20 (1972).
- [7] R. Gastmans and R. Meuldermans, *Nucl. Phys.***B63**, 277 (1973); W.J. Marciano and A. Sirlin, *Nucl. Phys.* **B88**, 86 (1975); W.J. Marciano, *Phys. Rev.* **D12**, 3861 (1975).
- [8] P. Langacker and M. Luo, *Phys. Rev.* **D44** (1991) 817.
- [9] U. Amaldi, W. de Boer and H. Fürstenau, *Phys. Lett.* **B260** (1991) 447.
- [10] L. Maiani, *Gif-sur-Yvette Summer School on Particle Physics*, (Natl. Inst. Nucl. Phys. Part. Phys., Paris, 1979).
- [11] M.J.G. Veltman, *Acta Phys. Pol.* **B12** (1981) 437.
- [12] M. Yoshimura, *Phys. Rev. Lett.*, **41** (1978) 281; M. Yoshimura, *Phys. Rev. Lett.*, **42** (1978) 746;  
A.Y. Ignatiev *et al.*, *Phys. Lett.* **B76** (1978) 436;  
S. Dimopoulos and L. Susskind, *Phys. Rev.* **D18** (1978) 4500;  
S. Weinberg, *Phys. Rev. Lett.*, **42** (1979) 850.
- [13] A.H. Guth, *Phys. Rev.* **D23** (1981) 347.
- [14] K. Sato, *Mon. Not. R. Astron. Soc.* **195** (1981) 467.
- [15] S. Burles and D. Tytler, *Astrophys. J.* **507** (1998) 732.
- [16] J. K. Webb *et al.*, *Nature* **388** (1997) 250.
- [17] D. Tytler, S. Burles, L. Lu, X-M. Fan and A. Wolfe, *Astron. J.* **117** (1999) 63.
- [18] D. Kirkman, D. Tytler, S. Burles, D. Lubin and J. O'Meara, astro-ph/9907128.
- [19] J. Geiss, in *Origin and Evolution of the Elements*, edited by N. Prantzos, E. Vangioni-Flam, and M. Cassé (Cambridge University Press, Cambridge, 1993) 89.
- [20] G. Sigl, K. Jedamzik, D.N. Schramm, and V.S. Berezhinsky, *Phys. Rev.* **D52** (1995) 6682, astro-ph/9503094.
- [21] P. Molaro, P. Bonifacio, M. Centurion and G. Vladilo, astro-ph/9908060.
- [22] K.A. Olive, G. Steigman, and E.D. Skillman, *Astrophys. J.* **483** (1997) 788.
- [23] Y.I. Izotov, T.X. Thuan, and V.A. Lipovetsky, *Astrophys. J. Suppl. Series.* **108** (1997) 1;  
Y.I. Izotov and T.X. Thuan, *Astrophys. J.*, **500** (1998) 188.
- [24] B.D. Fields and K.A. Olive, *Astrophys. J.*, **506** (1998) 177.
- [25] P. Bonifacio and P. Molaro, *Mon. Not. R. Astron. Soc.* **285** (1997) 847.
- [26] C.J. Hogan, astro-ph/9609138.
- [27] B.D. Fields, K. Kainulainen, K.A. Olive, and D. Thomas, *New Astron.* **1** (1996) 77, astro-ph/9603009.
- [28] L.M. Hobbs and J.A. Thorburn, *Astrophys. J.* **491** (1997) 772.
- [29] V.V. Smith, D.L. Lambert, and P.E. Nissen, *Astrophys. J.* **408** (1993) 262.
- [30] D.J. Fixsen *et al.*, *Astrophys. J.* **473** (1996) 576.
- [31] L. Kawano, preprint FERMILAB-Pub-92/04-A.
- [32] C. Caso *et al.*, Particle Data Group, *Euro. Phys. J. C* **3**, 1 (1998).
- [33] G.R. Caughlan and W.A. Fowler, *Atomic Data and Nuclear Data Tables* **40** (1988) 283; M.S. Smith, L.H. Kawano, and R.A. Malaney, *Astrophys. J. Suppl. Series* **85** (1993) 219.
- [34] G. Fiorentini, E. Lisi, S. Sarkar, and F. L. Villante, astro-ph/9803177.
- [35] T.P. Walker, G. Steigman, D.N. Schramm, K.A. Olive, and H.-S. Kang, *Astrophys. J.* **376** (1991) 51; Subir Sarkar, *Rept. Prog. Phys.* **59** (1996) 1493, hep-ph/9602260.

- [36] J. Yang, M.S. Turner, G. Steigman, D.N. Schramm, and K.A. Olive, *Astrophys. J.* **281** (1984) 493.
- [37] C.J. Copi, D.N. Schramm, and M.S. Turner, *Phys. Rev. Lett.* **75** (1995) 3981, *astro-ph/9508029*.
- [38] For a review, H.P. Nilles, *Phys. Rep.* **110** (1984) 1.
- [39] C.D. Coughlan, N. Fischler, E.W. Kolb, S Rabi and G.G Ross, *Phys. Lett.* **B131** (1983) 59;  
T. Banks, D.B. Kaplan and A.E. Nelson, *Phys. Rev.* **D49** (1994) 779;  
B. de Carlos, J.A. Carlos, F. Quevedo and E. Roulet, *Phys. Lett.* **B174** (1993) 447.
- [40] D.H. Lyth and E.D. Stewart, *Phys. Rev. Lett.* **75** (1995) 201, *hep-ph/9502417*; *Phys. Rev.* **D53** (1996) 1784, *hep-ph/9510204*.
- [41] For a review, see G.F. Giudice and R. Rattazzi, *hep-ph/9801271*.
- [42] J. Hashiba, M. Kawasaki and T. Yanagida, *Phys. Rev. Lett.*, **79**, 4525 (1997), *hep-ph/9708226*;  
T. Asaka, J. Hashiba, M. Kawasaki and T. Yanagida, *Phys. Rev.* **D58**, 083509 (1998), *hep-ph/9711501*;  
T. Asaka and M. Kawasaki, *Phys. Rev.* **D60**, 123509 (1999), *hep-ph/9905467*.
- [43] M. Kawasaki, K. Kohri and N. Sugiyama, *Phys. Rev. Lett.*, **82**, 4168 (1999), *astro-ph/9811437*.
- [44] R.E. Lopez, S. Dodelson, A. Heckler and M.S. Turner, *Phys. Rev. Lett.*, **82** 3952 (1999), *astro-ph/9803095*.
- [45] C.L. Bennett *et al.*, *Astrophys. J. Letter* **464**, L1 (1996).
- [46] <http://map.gsfc.nasa.gov/>
- [47] <http://astro.estec.esa.nl/SA-general/Projects/Planck/>
- [48] J. Bernstein, *Kinetic Theory in the Expanding Universe* (Cambridge Univ. Press, Cambridge, 1988).
- [49] J. Bernstein, L. Brown and G. Feinberg, *Phys. Rev.* **D32** 3261 (1985).
- [50] S. Hannestad and J. Madsen, *Phys. Rev.* **D52** 1764 (1995), *astro-ph/9506015*.
- [51] A.D. Dolgov, S.H. Hansen and D.V. Semikoz, *Nucl. Phys.* **B502** (1997) 3, *hep-ph/9703315*;  
A.D. Dolgov, S.H. Hansen and D.V. Semikoz, *Nucl. Phys.* **B543** (1999) 269, *hep-ph/9805467*.

- [52] M. Srednicki, R. Watkins and K. Olive, *Nucl. Phys.* **B310** (1988) 693.
- [53] M. Kawasaki, G. Steigman and H-S Kang, *Nucl. Phys.* **B403** (1993) 671;  
M. Kawasaki, P. Kernan, H-S, Kang, R.J. Scherrer, G. Steigman and T.P. Walker, *Nucl. Phys.* **B419** (1994) 105;  
M. Kawasaki, K. Kohri and K. Sato, *Phys. Lett.* **B430** (1998) 132, *astro-ph/9705148*.
- [54] E.W. Kolb and M.S. Turner, *The Early Universe*, Addison-Wesley (1990).
- [55] E. Holtmann, M. Kawasaki, K. Kohri and T. Moroi, *Phys. Rev.* **D60** 023506 (1999), *hep-ph/9805405*.
- [56] S. Dimopoulos, G. Dvali, R. Rattazzi and G.F. Giudice, *Nucl. Phys.* **B510** (1998) 12.
- [57] M. H. Reno and D. Seckel, *Phys. Rev.* **D37**, 3441 (1988).
- [58] K. Kohri and J. Yokoyama, *Phys. Rev.* **D61** 023501 (2000).
- [59] O. Biebel, private communication.
- [60] A. G. Riess *et al.*, *Astron. J.* **116**, 1009 (1998).
- [61] S. Perlmutter *et al.* *Astrophys. J.* **517**, 565 (1999).
- [62] S. Hancock, G. Rocha, A. N. Lasenby and C. M. Gutiérrez, *Mon. Not. R. Astron. Soc.* **294**, L1 (1998); G. Efstathiou *et al.* *Mon. Not. R. Astron. Soc.* **393**, L47 (1999); M. Tegmark, *Astrophys. J.* **514**, L69 (1999).
- [63] J. M. Bardeen, J. R. Bond, N. Kaiser and A. S. Szalay, *Astrophys. J.* **304**, 15 (1986).
- [64] J.A. Peacock and S.J. Dodds, *Mon. Not. R. Astron. Soc.* **267**, 1020 (1994).
- [65] N. Sugiyama and N. Gouda, *Prog. Theor. Phys.* **88**, 803 (1992).
- [66] V. R. Eke, S. Cole and C. S. Frenk, *Mon. Not. R. Astron. Soc.* **282**, 263 (1996).
- [67] N. A. Bahcall and X. Fan, *Astrophys. J.* **504**, 1 (1998); P. T. P. Viana and A. R. Liddle, in *Proceedings of the Conference "Cosmological Constraints from X-Ray Clusters"* (to be published), *astro-ph/9902245*.
- [68] J. R. Mould *et al.*, *astro-ph/9909260*.
- [69] W. Hu, N. Sugiyama and J. Silk, *Nature* **386**, 37 (1997).
- [70] Ya.B. Zel'dovich and I.D. Novikov, *Soviet Astronomy* **10**, 602 (1967); S.W. Hawking, *Mon. Not. R. astr. Soc.* **152**, 75 (1971); B.J. Carr, *Astrophys. J.* **201**, 1 (1975).

- [71] C. Alcock *et al.*, *Nature*, **365**, 623 (1990); *Phys. Rev. Lett.* **74**, 2867 (1995); *Astrophys. J.* **486**, 697 (1997); E. Aubourg *et al.*, *Nature*, **365**, 623 (1993); *Astron. Astrophys.* **301**, 1 (1995).
- [72] J. Yokoyama, *Astron. Astrophys.* **318**, 673 (1997); *Phys. Rev. D* **58**, 083510 (1998); *Phys. Rep.* **307**, 133 (1998).
- [73] S.W. Hawking, *Nature* **248**, 30 (1974); *Comm. Math. Phys.* **43**, 199 (1975).
- [74] B.J. Carr, *Astrophys. J.* **206**, 8 (1976).
- [75] B.V. Vainer and P.D. Nasel'skii, *Astron. Zh.* **55**, 231 (1978) [*Sov. Astron.* **22**, 138 (1978).]
- [76] S. Miyama and K. Sato, *Prog. Theor. Phys.* **55**, 1012 (1978).
- [77] Ya.B. Zel'dovich, A.A. Starobinskii, M.Yu. Khlopov, and V.M. Chechëtkin, *Pis'ma Astron. Zh.* **3**, 208 (1977) [*Sov. Astron. Lett.* **3**, 110 (1977).]
- [78] B.V. Vainer, O.V. Dryzhakova, and P.D. Nasel'skii, *Pis'ma Astron. Zh.* **4**, (1978) [*Sov. Astron. Lett.* **4**, 185 (1978).]
- [79] D. Lindley, *Mon. Not. R. Astron. Soc.* **193**, 593 (1980).
- [80] Ya.B. Zel'dovich, A.A. Starobinskii, *JETP Lett.* **24**, 571 (1976).
- [81] J.H. MacGibbon, *Nature* **329**, 308 (1987); J.H. MacGibbon and B.J. Carr, *Astrophys. J.* **371**, 447 (1991).
- [82] M.B. Bowick, S.B. Giddings, and J.A. Harvey, *Phys. Rev. Lett.* **61**, 2823 (1988); J.D. Barrow, E.J. Copeland, and A.R. Liddle, *Phys. Rev.* **D46**, 645 (1992).
- [83] J.D. Barrow and B.J. Carr, *Phys. Rev. D* **54**, 3920 (1996).
- [84] A.M. Green and A.R. Liddle, *Phys. Rev. D* **56**, 6166 (1997).
- [85] For a review of BBN, see, *e.g.* T.P. Walker, G. Steigman, D.N. Schramm, K.A. Olive, and H.-S. Kang, *Astrophys. J.* **376** (1991) 51; K.A. Olive, G. Steigman, and T.P. Walker, *astro-ph/9905320*
- [86] J.H. MacGibbon and B.J. Carr, *Astrophys. J.* **371**, 447(1991) ; B.J. Carr and J.H. MacGibbon, *Phys. Rept.* **307**, 141(1998).
- [87] J.C. Niemeyer and K. Jedamzik, *Phys. Rev. Lett.* **80**, 5481 (1998); *Phys. Rev.* **D59**, 124013 (1999).
- [88] M. Shibata and M. Sasaki, *gr-qc/9905064*, to appear in *Phys. Rev. D*.

- [89] J. Yokoyama, *Phys. Rev.* **D58**, 107502 (1998); A.M. Green and A.R. Liddle, *astro-ph/9901268*; H.I. Kim, *astro-ph/9907372*.
- [90] A.A. Starobinsky and S.M. Churilov, *Zh. Eksp. Theor. Fiz.* **65**, 3(1973) [*Sov. Phys. JETP* **38**, 1(1974)] D.N. Page, *Phys. Rev. D* **13**, 198(1976); **14**, 3260(1976); **16**, 2402(1977).
- [91] J.H. MacGibbon and B.R. Webber, *Phys. Rev. D* **41**, 3052(1990).
- [92] J.H. MacGibbon, *Phys. Rev. D* **44**, 376(1991).
- [93] S. Dimopoulos, R. Esmailzadeh, L. Hall, and G. Starkman, *Phys. Rev. Lett.* **60**, 7 (1988); *Astrophys. J.* **330**, 545 (1988); *Nucl. Phys.* **B311**, 699 (1988/89).
- [94] K. Kohri and J. Yokoyama, in preparation.
- [95] W. Furmanski, R. Petronzio and S. Pokorski, *Nucl. Phys.* **B155**, 253 (1979); A. Bassetto, M. Ciafaloni and G. Marchesini, *Phys. Lett.* **B83**, 207 (1979); K. Konishi, *Rutherford Lab. Rep* RL 79-035 (1979); A. H. Mueller, *Phys. Lett.* **B104**, 161 (1981); *Nucl. Phys.* **B213**, 85 (1983).
- [96] J.H. Applegate and C.J. Hogan, *Phys. Rev.* **D31**, 3037 (1985).
- [97] M. Kawasaki and T. Moroi, *Prog. Theor. Phys.* **93** (1995) 879, *hep-ph/9403364*.
- [98] M. Kawasaki and T. Moroi, *Astrophys. J.* **452** (1995) 506, *astro-ph/9412055*.
- [99] A.A. Zdziarski, *Astrophys. J.* **335** (1988) 786; R. Svensson and A.A. Zdziarski, *Astrophys. J.* **349** (1990) 415.
- [100] R.D. Evans. *The Atomic Nucleus* (McGraw-Hill, New York, 1955).
- [101] R. Pfeiffer. *Z. Phys.* **208** (1968) 129.
- [102] D.D. Faul, B.L. Berman, P. Mayer, and D.L. Olson, *Phys. Rev. Lett.* **44** (1980) 129.
- [103] A.N. Gorbunov and A.T. Varfolomeev, *Phys. Lett.* **11** (1964) 137.
- [104] J.D. Irish, R.G. Johnson, B.L. Berman, B.J. Thomas, K.G. McNeill, and J.W. Jury, *Can. J. Phys.* **53** (1975) 802.
- [105] C.K. Malcom, D.V. Webb, Y.M. Shin, and D.M. Skopik, *Phys. Lett.* **B47** (1973) 433.
- [106] Yu.M. Arkatov, P.I. Vatsset, V.I. Voloshchuk, V.A. Zolenko, I.M. Prokhorets, and V.I. Chimil', *Sov. J. Nucl. Phys.* **19** (1974) 598.
- [107] B.L. Berman, *Atomic Data and Nuclear Data Tables* **15** (1975) 319.

- [108] W. Hu and J. Silk, Phys. Rev. Lett. **70** (1993) 2661.
- [109] A.P. Lightman, Astrophys. J. **244** (1981) 392.
- [110] J. Gratsias, R.J. Scherrer, and D.N. Spergel, Phys. Lett. **B262** (1991) 298; M. Kawasaki and T. Moroi, Phys. Lett. **B346** (1995) 27, hep-ph/9408321.
- [111] K.A. Olive and M. Srednicki, Phys. Lett. **B230** (1989) 78.
- [112] B. de Carlos, J.A. Casas, F. Quevedo, and E. Roulet, Phys. Lett. **B318** (1993) 447, hep-ph/9308325.
- [113] H. Kang and G. Steigman, Nucl. Phys. **B372** (1992) 494.
- [114] A. Lenard, Phys. Rev. **90**, 968 (1953).
- [115] E.W. Kolb and S. Wolfram, Nucl. Phys. **B172** (1980) 224.
- [116] D.A. Dicus, Phys. Rev. **D6** 941 (1972).
- [117] H.-Y. Chiu and R.C. Stabler, Phys. Rev. **122** 1317 (1961).

120

